



MASTER'S THESIS

Time-Resolved Quantum Simulations of
Photosynthetic Energy Transport with
Superconducting Qubits

Graham J. NORRIS

Supervisor: Dr. Anton POTOČNIK

Principal Investigator: Prof. Dr. Andreas WALLRAFF

April 3, 2018

Contents

1	Photosynthetic Energy Transport	2
1.1	Introduction	2
1.2	Photosynthesis	2
1.3	Photosynthetic Energy Transport	3
1.4	Studies of Photosynthetic Energy Transport	5
1.4.1	Open Questions	6
1.5	Analog Quantum Simulation	7
1.5.1	Quantum Simulations of NAT	8
1.6	Current Work	9
1.7	Note to the Reader	9
2	Experimental System and Apparatus	10
2.1	Target Hamiltonian	10
2.2	Superconducting Simulator Sample	11
2.2.1	Design	11
2.2.2	Hamiltonian	13
2.2.3	Hacken–Strobl–Reineker Model	13
2.2.4	Physical Sample	14
2.2.5	Simulation Standard Configuration	15
2.2.6	Flux Noise	17
2.3	Experimental Apparatus	17
2.3.1	Dilution Refrigerator	17
2.3.2	Microwave Generation and Measurement	19
2.3.3	Noise Generation	21
3	Results and Discussion	24
3.1	Hamiltonian Characterization Measurements	24
3.1.1	Mutual Inductance and Maximum Frequency	24
3.1.2	Rabi Rate	27
3.2	Environment Characterization Measurements	28
3.2.1	Purcell Decay Rate	28
3.2.2	Intrinsic Dephasing Rate	29
3.2.3	T_1 , T_2 , and Dephasing Rate	30

3.3	Interacting Many-Body System Characterization	34
3.3.1	Coherent Spectroscopy	34
3.4	Time-Resolved Photosynthetic Excitation Transport Measurements	36
3.4.1	Numerical Simulations	40
4	Conclusions	42
A	Derivation of System Hamiltonian	45
A.1	Harmonic Oscillator	45
A.2	LC Oscillator	46
A.3	Josephson Junction	48
A.3.1	Cooper Pair Box	49
A.3.2	Transmon	51
A.3.3	Superconducting Quantum Interference Devices	51
A.4	System Hamiltonian	52
A.4.1	Qubit-Qubit Coupling	52
A.4.2	Qubit-Transmission Line Coupling	53
B	Open Quantum Systems	55
B.1	Lindblad Formalism	55
C	Methods	57
C.1	Bandwidth of Pulses and Boxcar Filter	57
C.2	Noise Voltage to Flux Power Conversion	57
C.3	TWPA	59
C.4	Rabi Measurements	59
C.4.1	Time-Resolved	59
C.4.2	Frequency-Resolved	60
C.5	T_1 Measurements	62
C.5.1	Inversion Recovery	62
C.5.2	Power	64
C.6	T_2 Measurements	64
C.7	2D Spectroscopy	65
D	COSY	66
D.1	Theory	66
D.2	Phase Cycling	70
D.3	Data Processing	70
E	Parameters	73
E.1	Numerical Simulations	73

Abstract

Many interesting systems in many-body physics and open quantum systems cannot be fully simulated using classical computers due to exploding memory requirements. We can overcome this limitation with analog quantum simulation, where techniques developed for building quantum computers are used to construct fixed-purpose simulators of physical systems. By using engineered quantum systems to emulate other quantum systems, we avoid the memory bottleneck of classical computers and can also realize simulations before general-purpose quantum computers are available.

In this thesis, I will present the details of my work on analog quantum simulations of energy transport during photosynthesis. I have extended the previous work in our group from steady-state to time-resolved measurements which required novel characterization techniques and which provide abundant information about our sample. I will present evidence that we observed clear signatures of quantum coherence in our experiments, validating our approach and preparing a path for more advanced quantum simulations in the future.

Chapter 1

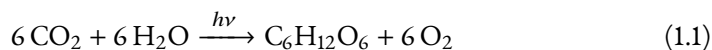
Photosynthetic Energy Transport

1.1 Introduction

In order to limit global warming to just 1.5 °C by 2100, our only option is to go carbon-negative, that is, to collect carbon dioxide from the atmosphere and store it within the Earth, and to do so on an industrial scale [1]. While this currently appears to be a daunting task, we are fortunate enough to have a finely honed example of carbon capture to study: photosynthetic organisms. Every year, the plants, bacteria, and algae of Earth sequester $(110 \pm 21) \times 10^{12}$ kg of carbon [2]. As a step in converting carbon dioxide into sugar, photosynthetic organisms manage to transport light-derived excitations over large distances, known as *photosynthetic energy transport*, and efficiently convert them into separated electrical charges using organic molecules, known as *charge separation*, processes humans are just starting to master. Furthermore, potentially inexpensive future sources of zero-emission energy such as organic photovoltaics depend on a better understanding of photosynthetic energy transport and the design guidelines that are contained therein. For these reasons, it is important to study photosynthetic energy transport mechanisms and to engineer artificial energy transport.

1.2 Photosynthesis

From a mass-balance perspective, photosynthesis is a simple process converting carbon dioxide, water, and light into glucose and oxygen¹:



However, the mechanisms used by photosynthetic organisms to achieve this simple reaction are highly involved multi-stage processes which I will attempt to condense into the following paragraphs.

Photosynthesis begins with the absorption of a photon of sunlight by pigments known as *chromophores*. Examples of chromophores used in biology include chlorophyll,

¹Note that there are also some organisms that use sulfur as the final electron acceptor rather than oxygen, consuming hydrogen sulfide (H₂S) and evolving sulfur.

bacteriochlorophyll, and carotenoids. After absorption, the excitation is transferred to a specialized pigment complex known as the *reaction center* where the excitation is converted into separated charges that can be used to drive chemical reactions, eventually resulting in the formation of sugar.

Since the reaction center requires significant additional chemical machinery to complete the task of charge separation, it is biologically expensive to build². At the same time, since it is based on a single light-absorbing molecule, its cross section for solar radiation is small. Simple estimates show that the reaction center can absorb around $10 \text{ photons s}^{-1}$ under ideal conditions, a plodding pace for biological systems where enzymes routinely reach the diffusion limit of more than 10^4 s^{-1} [3, Chp. 5]. To surpass the cross-section limit, photosynthetic organisms build many additional chromophores, called an *antenna complex*, and connect them to the reaction center. This vastly increases the surface area for absorbing solar radiation. In most cases, the chromophores are not randomly distributed, but are held in specific orientations by a protein matrix, known collectively as a *pigment-protein complex* (PPC). Remarkably, despite the warm and fluctuating environment of cells at physiological temperatures, photosynthetic organisms achieve a nearly unit quantum yield for energy transport from the antenna complexes to the reaction center, meaning that a single charge carrier is formed for each photon absorbed by a chromophore [3, Chp. 1].

One important pigment-protein complex (PPC) is the Fenna–Matthews–Olson (FMO) complex from green sulfur bacteria. Green sulfur bacteria are widely studied in the biophysics community due to their relatively simple photosynthetic system. The FMO complex is particularly important because it was the first PPC for which an x-ray structure was determined [4] and among the first to have an extraction protocol [5]. This complex is trimer of proteins each containing 7–8 bacteriochlorophyll surrounded by a protein scaffold that holds each of the chromophores in a specific location and orientation. The pigments in a single subunit of the complex are pictured in Figure 1.1. For a list of the extensive theoretical and spectroscopic studies of the FMO complex, consult [6].

As the final stage of photosynthesis considered here, the excitation is trapped in photochemical products by the reaction center. This trapping can be strong (*deep trapping*), characterized by a unidirectional transfer of energy, or weak (*shallow trapping*), characterized by oscillation of the excitation between the reaction center and the antenna proteins bound to it [3, Chp. 5]. After trapping, the remainder of photosynthesis is predominantly based on chemical reactions which are outside the scope of this work.

1.3 Photosynthetic Energy Transport

As is clear from the above discussion, a crucial point of photosynthesis is a directed transfer of excitations from dispersed chromophores to the sparse reaction centers. Without this movement, photosynthesis could not have a high quantum yield, and wasted excitations would generate dangerous products such as singlet oxygen that would damage

²Since additional reaction centers require additional supporting machinery.

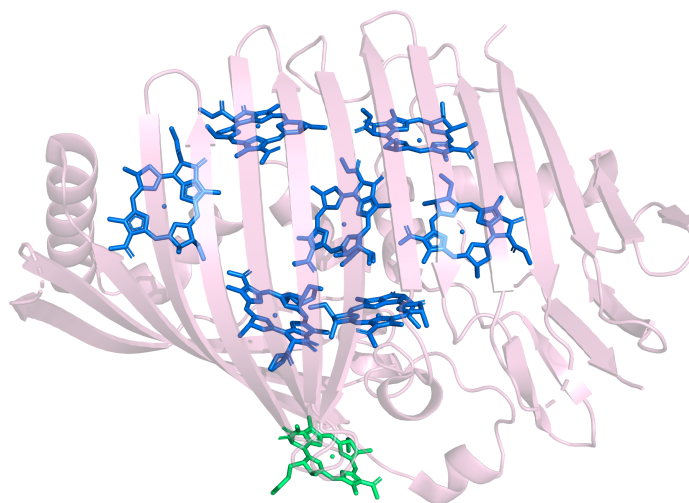


Figure 1.1: Subunit of FMO complex with the bacteriochlorophyll *a* molecules shown in blue and green, and the protein matrix that surrounds the chromophores shown in translucent purple. Approximate scale: 4 pm. The phytol tails of the bacteriochlorophyll have been omitted. Image of Protein Data Bank file 3ENI [7] created with PyMOL [8].

the organism [9]. These excitations form electron-hole quasiparticles which propagate through the antenna complexes and are referred to as (*Frenkel*³) *excitons* [12].

While there was initially interest in modeling chlorophyll as a network or crystal on which excitons propagate quantum mechanically (see *e.g.* [13]), this interest disappeared when a semiclassical model known as Förster resonance energy transfer (FRET) [14] appeared. FRET explains the high efficiency of photosynthetic energy transport (PET) by modeling the chromophores as weakly interacting dipoles that exchange virtual photons. This approach works well for intermediate distances, where the overlap of electronic wavefunctions is small, such as from an antenna complex to the reaction center or from one antenna complex to another [3, Chp. 5]. In addition, the chromophores of antenna complexes tend to be arranged such that chromophores closer to the reaction center are lower in energy than chromophores farther away, providing directional bias in the transport. Thus, it seemed that PET was an entirely diffusive process, a view that was supported by the fact that cells are warm and wet environments which should suppress any quantum coherence on timescales much faster than the energy transfer dynamics [15].

However, later results questioned this orthodoxy, hinting that quantum coherent effects may play a role in PET. Structural analysis of PPCs revealed that they had closely

³After Yakov Frenkel, [10, 11]

spaced chromophores, a situation where FRET breaks down due to overlapping electronic wavefunctions, known as *excitonic* coupling, in which the eigenstates become *dressed* or superpositions of the individual chromophore wavefunctions. This can lead to the formation of the *bright* and *dark* states from quantum optics, which were observed in a different PPC, LH2 from purple sulfur bacteria [16]. Beyond this, direct experimental evidence of quantum transport behavior was discovered in FMO, first at cryogenic temperatures [17] and then at physiological ones [18].

1.4 Studies of Photosynthetic Energy Transport

Early photosynthesis research focused on determining the chemistry of photosynthesis and then the stoichiometry of the reaction (Equation 1.1) [19]. Initial spectroscopic measurements studied the quantum efficiency of photosynthesis, rates of reactions, and identification of the system components [20]. Spectroscopy was also able to determine whether the chromophores are strongly or weakly coupled by comparing *in vivo* and *in vitro* spectroscopy [21]. While steady-state or modulated spectroscopy was able to determine that energy transport was taking place, it was not until the advent of picosecond spectroscopy, including techniques such as transient absorption, that dynamics of the energy transfer process could be measured [22, 23]. Further enhancements of timing resolution, using femtosecond lasers, led to the startling results about the electronic dynamics previously mentioned [17, 18].

Since those landmark measurements, Panitchayangkoon *et al.* extended their previous work, observing oscillation of the exciton population on different chromophores, something that they asserted was direct evidence for quantum transport in FMO [24], relying on theoretical results from Abramavicius and Mukamel [25]. Countering this, a number of results disputed the nature of these observed coherences or their physiological applicability under incoherent illumination from the sun. Eisfeld and Briggs found, under approximations, classical coherences matching the observed quantum coherences implying that a quantum description of FMO may not be necessary to account for the observed coherences [26]. Wilkins and Dattani provided a sobering theoretical analysis showing that incoherent transport is predicted to be faster than quantum transport in FMO and that the importance of quantum transport depends crucially on the rate of trapping in the reaction center, which had not been included in prior simulations [27]. Pachón *et al.* found that there are no coherent dynamics under illumination by a thermal source, even for a non-equilibrium open quantum system [28, 29]. Duan *et al.* rule out long-lived electronic coherences in FMO, meaning that noise-assisted transport relying on purely electronic states does not play a role in photosynthesis [30], which, however, does not rule out hybrid electronic-vibrational (vibronic) coherences, a mechanism suggested by Huelga and Plenio [31]. Trying to bridge the divide between these two groups, Romero *et al.* were careful to distinguish two types of coherences: *static coherences* due to strongly coupled portions of the system (called excitonic coupling above) and *dynamic coherences* induced by exciting a portion of the Hilbert space rather than an eigenstate of

the full system, arguing that static coherences might be responsible for high efficiency even in the case of incoherent transport [32].

The possible discovery of quantum effects in PET immediately renewed interest in analyzing photosynthetic complexes as quantum networks, resulting in a hypothesis termed *environment-assisted quantum transport* (ENAQT) [15]. ENAQT, also known as *noise-assisted transport* (NAT), considers PPCs as a network of quantum sites. When perfectly isolated, any excitation of the system would delocalize over the entire PPC, preventing it from transferring to the specific site which is coupled to the reaction center. In the opposite case, inside an extremely noisy bath, any excitation will experience strong dephasing, localizing it and again preventing it from reaching the reaction center. Thus, counter to the usual intuition that noise is always detrimental, the NAT hypothesis claims that there will be an intermediate level of environmental noise which leads to maximum transportation efficiency.

Since that result, further progress has been made to understanding NAT. Plenio and Huelga asserted that Markovian noise might assist energy transport within dissipative quantum networks that include dephasing, such as an FMO monomer with phononic (vibrational) modes [33]. Mohseni *et al.* found similar results using a Lindblad master equation and quantum walk formalism, adding that the phononic modes may also assist transport efficiency by acting as a dissipative sink for energy, trapping the exciton at progressively lower energy sites [34]. They disputed the claim by Engel *et al.* in [17] that the efficiency of energy transport in FMO was due to a Grover-like search⁴ for the lowest-energy chromophore, since the exciton delocalizes only over a few sites. Finally, Rebentrost *et al.* also found, using a Lindblad master equation approach, that environment-induced relaxation was responsible for approximately 90 percent of the energy transfer efficiency of FMO, with the remainder corresponding to coherent dynamics [36], quantifying the impact of NAT on photosynthetic organisms.

One particularly difficult issue has been how to explain the experimentally observed long-lived coherence given the short phase-coherence time that has been independently measured [15]. One solution proposed by Huelga and Plenio, is the *phonon antenna* mechanism, where the exciton induces nuclear motion including a well-defined vibrational mode with a low frequency and a long lifetime [31]. In this model, the phonon mode is excited into a coherent state which then drives population transfer between excitonic states with an energy difference comparable to the vibrational mode.

1.4.1 Open Questions

With this sort of disagreement within the field, there are clearly open questions pertaining to photosynthetic energy transport. Two of the prominent ones are:

- *What is the exact nature of the coherences that are observed (e.g. electronic, vibrational, vibronic)?* This determines the importance of the phononic modes and consequently, NAT.

⁴ See [35]

- *What quantum effects, if any, play a role in the transport dynamics under incoherent illumination?* This determines whether NAT offers any improvement under realistic excitation conditions and hence whether useful “design principles” can be taken from quantum networks and applied to organic photovoltaics.

Unfortunately, these questions are difficult to treat theoretically and experimentally. Since the energy scale of electronic coupling between chromophores is similar to the energy scale of coupling between the chromophores and the phononic modes of the protein, no perturbative approximation can be made, hampering theoretical studies of FMO [37]. On the other hand, spectral congestion makes assigning spectroscopic features to a specific site in the PPC difficult. Biologists can get around this by modifying the PPC, but this is not always easy or guaranteed to have the same behavior as the original complex [32]. In the next section, I will discuss one possible solution to study these questions in a tractable fashion: quantum simulation.

1.5 Analog Quantum Simulation

While quantum computers might one day help develop new catalysts to directly fix CO₂ or simulate the full dynamics of pigment-protein complexes, we can apply the technology being used to build the quantum computers of the future *today* to evaluate models of energy transfer in photosynthetic organisms. This technique is known as *analog quantum simulation* and it is where quantum systems are engineered to directly exhibit the dynamics of a target system rather than perform universal quantum calculations via long sequences of gates. Thus, we trade generality for easier implementation: a universal quantum computer can tackle any computable problem, but is currently difficult to make while an analog quantum simulator solves only one sort of problem but is implementationally feasible. Here I draw strong parallels to the dawn of classical computing, where the first useful computers such as ENIAC had to be laboriously re-wired by hand to perform different types of calculations and only later did general-purpose, stored-program computers such as EDVAC become feasible as the technology and understanding of computer construction improved.

First proposed by Feynman in 1982 [38], analog quantum simulations have now been conducted for: spin systems using superconducting circuits [39] as well as trapped ions [40]; for quantum phase transitions using cold atoms [41], along with many others. For a recent review, see [42].

Noise-assisted transport is a particularly good target for analog quantum simulation because it naturally involves a network of quantum sites and noise is not necessarily undesirable as it is for digital quantum computation. Analog quantum simulators designed to study NAT in the context of photosynthetic energy transport may help in resolving the open questions facing the biophysics community. Interactions are typically engineered, meaning that the coherences can be chosen to be electronic, vibrational, or a mix of the two, and may even be tunable. At the same time, since engineered quantum systems are typically isolated from their environment and rely on external drives for all dynamics, we can directly study the effect of incoherent versus coherent drive and have techniques

to characterize the light involved in transport. Even if photosynthetic energy transport does not involve any quantum behavior under incoherent excitation, we may still learn about how to optimally select environmental modes to optimize energy transport from studying NAT, especially in highly-tunable systems.

1.5.1 Quantum Simulations of NAT

Some of the earliest theoretical studies of NAT in the context of photosynthetic energy transport proposed to use quantum systems to simulate the dynamics due to the difficulty of isolating specific effects in biological systems [33]. These were followed by proposals to study NAT in a superconducting circuit analog of the FMO complex [43] and in quantum dots [44]. At this point, there were only proposals for how to test NAT in engineered quantum systems.

Experimental studies of NAT started appearing in 2015, when León-Montiel *et al.* investigated NAT using a three-site *LRC*-oscillator circuit [45]. They modeled dephasing by adding high-frequency noise to the coupling between two sites on the network, finding increased transport efficiency with increasing broadband noise amplitude. Biggerstaff *et al.* investigated ENAQT using a four-site photonic waveguide system [46]. They were able to recreate the results expected from ENAQT, but could not simulate different configurations as the site energies and couplings were determined by the material and fabrication parameters of the device and were not tunable *in situ*. Both of these classical experiments only included white noise and had fixed system parameters outside of the dephasing rate.

At the same time, several groups studied quantum approaches to studying photosynthetic energy transport. Imada *et al.* investigated resonance energy transport between molecular dimers using scanning tunneling spectroscopy, studying incoherent transport in an artificial quantum system [47]. Harris *et al.* scaled the photonic approach to a discrete-time simulation with 26 sites and 88 interaction elements [48]. They incorporated both static and dynamic disorder and found maximum quantum transport efficiency at intermediate disorder levels, the expected ENAQT results.

In 2018, Potočnik, Bargerbos, *et al.*, inspired by the proposal of Mostame *et al.*, studied NAT using a superconducting circuit sample, moving from classical simulations or discrete-time quantum simulations to a continuous-time semi-quantum simulation, where the system is quantum but the noise replicating phonon modes is classical [49]. As with the previous studies, they measured steady-state power transfer efficiency for broadband noise, finding optimal efficiencies at intermediate dephasing rates. In addition, they considered shaped noise akin to a phononic mode, finding that this dramatically improved transfer efficiency. Unlike previous studies, their three-site system had tunable site frequencies (with coupling tied to detunings) and hence is able to look at transfer in several different configurations.

Recently, Gorman *et al.* looked at NAT in a two-site fully quantum system [50]. Using trapped ions, they measured increased population transfer from one site to another when the vibrational mode was tuned to equal the site energy difference along with

nontrivial population dynamics due to non-Markovian noise. However, their simulation does not include any trapping dynamics.

1.6 Current Work

Now that previous studies have validated the use of analog quantum simulators for studying noise assisted transport, I can extend the work of Potočnik and Bargerbos on superconducting circuits to time-resolved measurements of NAT. At the most basic level, this will verify that the simulator correctly exhibits the dynamics that it was designed to, an obvious milestone on the path to more advanced simulations. At the same time, we want to engineer static coherences in the system and observe their effect on the transport dynamics, which should clearly appear in the time domain. In addition, we can measure additional parameters of the transfer dynamics, such as timing, which cannot readily be extracted from steady-state measurements. Finally, time-dependent methods allow us to implement a number of characterization methods to determine system parameters in a way more familiar to the community or to prove that the system behaves quantum-mechanically.

1.7 Note to the Reader

This text is primarily intended for an audience familiar with quantum optics and circuit quantum electrodynamics (cQED) implemented via superconducting transmon qubits, and so in the interests of brevity, I will not cover these topics in the main text. However, I have included some material on these topics in the appendices (starting from [Appendix A](#)) and will try to link to them from the main text where they might help someone less familiar with the material.

Chapter 2

Experimental System and Apparatus

2.1 Target Hamiltonian

For our simulation of NAT to provide useful information about models of photosynthetic energy transport, it must mimic the dynamics of the real system, which is most clearly evident when the systems have the same Hamiltonian. Pigment-protein complexes contain many electronic and nuclear degrees of freedom; however, I will focus on the photosynthetically active electronic modes based in the chromophores and the “phononic” vibrational modes of the chromophores and proteins that couple to the chromophores due to their proximity and electrostatic forces. Here I will work in the *site* basis, where (electronic) state $|j\rangle$ corresponds to chromophore j of the PPC being in the excited state ($|e\rangle$) and all other chromophores being in the ground state ($|g\rangle$). This choice is motivated by the fact that the electronic excitations rarely delocalize over more than a few sites [37] and holds for low illumination intensities. With this context in mind, following [43], I can write the Hamiltonian of the PPC as:

$$\begin{aligned}\hat{H} &= \sum_j \hbar\omega_j |j\rangle \langle j| + \sum_j \sum_{k < j} V_{jk} (|j\rangle \langle k| + |k\rangle \langle j|) && (\hat{H}_S) \\ &+ \sum_j \sum_m \chi_j^m |j\rangle \langle j| (\hat{a}_j^{m\dagger} + \hat{a}_j^m) && (\hat{H}_{SB}) \\ &+ \sum_j \sum_m \hbar\omega_j^m (\hat{a}_j^{m\dagger} \hat{a}_j^m + 1/2) && (\hat{H}_B)\end{aligned}\tag{2.1}$$

where I have grouped the contributions into three terms: one for the electronic degrees of freedom (called the *system*), one for the interaction between the electronic and phononic degrees of freedom (called the *system-bath* interactions), and one for the phononic degrees of freedom (called the *bath*). In all terms, subscript j and k refer to electronic states, while superscript m refers to phononic modes. The system terms include both the individual site transition energies (given by ω_j) and the exchange interactions (with strength V_{jk}). The bath is treated as a number of harmonic oscillators at each site, with frequencies

ω_j^m and creation (annihilation) operator $\hat{a}_j^{m\dagger}$ (\hat{a}_j^m). The system and bath interact with strength χ_j^m , which can be derived from characteristics of the particular sites¹.

To facilitate the comparison with superconducting circuit Hamiltonians, Equation 2.1 can be re-written in terms of Pauli matrices for the electronic terms:

$$\begin{aligned} \hat{H} = & \sum_j \hbar\omega_j \hat{\sigma}_j^z + \sum_j \sum_{k < j} V_{jk} \left(\hat{\sigma}_j^+ \hat{\sigma}_k^- + \hat{\sigma}_k^+ \hat{\sigma}_j^- \right) \\ & + \sum_j \sum_m \chi_j^m \hat{\sigma}_j^z \left(\hat{a}_j^{m\dagger} + \hat{a}_j^m \right) \\ & + \sum_j \sum_m \hbar\omega_j^m \left(\hat{a}_j^{m\dagger} \hat{a}_j^m + 1/2 \right) \end{aligned} \quad (2.2)$$

where $\sigma_j^\pm \equiv 1/2 \left(\hat{\sigma}_j^x \pm i\hat{\sigma}_j^y \right)$ are Pauli raising and lowering operators. In this notation, it is clear that the electron-phonon coupling (system-bath interaction) corresponds to *longitudinal* or $\hat{\sigma}^z$ coupling, affecting the transition energies of the electrons. This type of coupling (as opposed to *transversal*, $\hat{\sigma}^x$ or $\hat{\sigma}^y$, coupling) has been difficult to achieve in the superconducting circuits that we use to build our simulator [51], discussed below.

2.2 Superconducting Simulator Sample

Superconducting circuits are a mature technology that enables us to build and control ever-increasing numbers of quantum bits, or *qubits*. The foundation for such qubits is a superconducting, dissipationless inductor-capacitor (*LC*) resonator, which produces a ladder of equally spaced energy levels in the microwave spectrum. To gain control of the system, we restrict the resonator to two levels by introducing a nonlinear element to the circuit. This nonlinear element, a superconductor-insulator-superconductor (S-I-S) junction known as a *Josephson junction* [52], distorts the harmonic potential into an anharmonic potential with unequal level spacing. A key property of Josephson-junction circuits is that at sufficiently low temperatures (≈ 10 mK) most degrees of freedom are frozen out and the macroscopic system behaves as a quantum two-level object. Significant technological progress has recently been made in the areas of fabrication, readout, and control, so superconducting circuit qubits have been chosen as the platform for building commercial quantum computers by several companies. For additional discussion of the Josephson effect and superconducting circuits, consult Appendix A and Refs. [53, 54].

2.2.1 Design

The design of the superconducting circuit was performed by Anton Potočnik and Arno Bargerbos and discussed by them in previous works [49, 55]. Since it is designed to test NAT, it consists of a network of qubits along with a source of dephasing noise.

¹ $\chi_j^m = \hbar\omega_j^m d_j^m$, where d_j^m represents the displacement in terms of a generalized oscillator position of the electronic excited state relative to the ground state

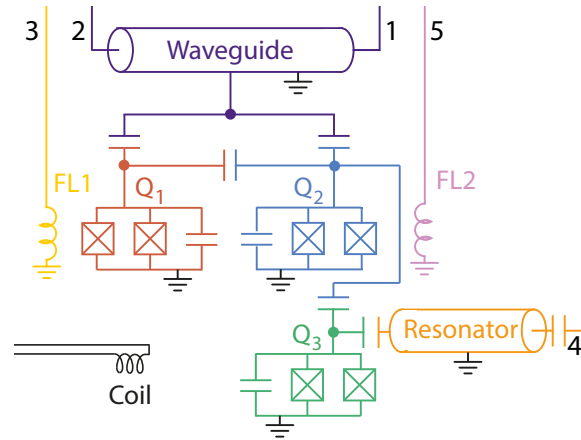


Figure 2.1: Circuit diagram of biological simulation sample. Qubits shown in red, blue, and green. Transmission line shown in purple; resonator shown in orange. Flux lines shown in yellow and pink; coil shown in black. Numbered traces are input or output lines used to configure, drive, or probe the sample. Adapted from [49].

More precisely, the circuit consists of three qubits, an input waveguide, an output resonator, along with flux lines and a coil affecting all qubits (see Figure 2.1). Two qubits, Q_1 and Q_2 , are linked through a capacitor which produces strong transverse coupling, leading to hybridization that results in eigenstates that are symmetric and antisymmetric combinations of the individual qubit states. These qubits are also simultaneously capacitively coupled to a transmission line. Since the distance over which the qubits are coupled is significantly smaller than the wavelength of microwaves that drive them (approximately 2 cm at 6 GHz), both qubits are driven equally, and thus the symmetric mode is strongly driven (making it a *bright* mode) while the antisymmetric mode is weakly driven (*dark* mode). Qubit 3, Q_3 , is capacitively coupled to qubit 2 along with the output resonator, which is itself capacitively coupled to a port.

All qubits used in the sample are formed from two junctions enclosing a small loop, a configuration known as a SQUID², which enables the transition frequencies of the qubits to be adjusted by the magnetic flux through the loop. Flux lines 1 and 2 (FL1 and FL2) provide local control over the magnetic field near qubits 1 and 2 respectively, while a large coil adjusts the magnetic flux through all three qubits.

The transmission line acts as a broadband input-output port for the bright and dark states, allowing us to rapidly drive these states or superpositions of the states, and acts as an antenna complex passing excitations to FMO. On the other side of the sample, the resonator and the waveguide attached to it act as the input-output port for qubit 3. The resonator functions as a Purcell filter [56], changing the coupling between qubit 3 and

²Superconducting Quantum Interference Device

the input/output line depending on the detuning between the qubit and the resonator. Since the input/output line is a semi-infinite 50Ω cable, emission into this port results in irreversible loss of the excitation, functioning as the reaction center, with the Purcell filter tuning the rate of the trapping dynamics.

2.2.2 Hamiltonian

Quantizing the circuit shown in [Figure 2.1](#), as I discuss in [Appendix A](#) and as laboriously completed by my predecessors following the instructions of, for example, Devoret, Vool, or Girvin [[57](#), [54](#), [58](#)], results in the following Hamiltonian [[55](#), [49](#)]:

$$\begin{aligned} \hat{H} = & \sum_j \frac{\hbar}{2} \omega_j(t) \hat{\sigma}_j^z + \hbar \omega_r \hat{a}^\dagger \hat{a} \\ & + \sum_j \sum_{k < j} J_{jk} \left(\hat{\sigma}_j^+ \hat{\sigma}_k^- + \hat{\sigma}_k^+ \hat{\sigma}_j^- \right) + \sum_j g_{jr} \left(\hat{a}^\dagger \hat{\sigma}_j^- + \hat{a} \hat{\sigma}_j^+ \right) \\ & + \frac{\Omega_1}{2} (\hat{\sigma}_1^+ + \hat{\sigma}_1^-) + \frac{\Omega_2}{2} (\hat{\sigma}_2^+ + \hat{\sigma}_2^-) \end{aligned} \quad (2.3)$$

where j sums over qubits 1–3 and r stands for the resonator, \hat{a}^\dagger (\hat{a}) is the resonator creation (annihilation) operator. J_{jk} parameterizes the qubit coupling strength while g_{jr} quantifies the strength of the qubit resonator couplings. Ω_1 (Ω_2) are the driving rates (*Rabi* rates) of qubits 1 (2) by a microwave field in the transmission line.

While this Hamiltonian has terms corresponding to the system terms of the goal Hamiltonian ([Equation 2.2](#)), *i.e.* electronic site energies and exchange interactions, there are no terms corresponding to the system-bath interactions or to the bath itself. This is due to the lack of longitudinal coupling on the sample, which remains an experimental challenge for superconducting circuits and which was deemed to be too complicated for this sample. However, there are ways to *emulate* the system-bath interactions via classical control signals, something I will discuss in the next section.

2.2.3 Haken–Strobl–Reineker Model

Haken, Strobl, and Reineker studied ways of analytically addressing electron-phonon interactions. Importantly, they found that, by letting the site energies fluctuate with time, they could recreate the effects of a phonon bath [[59](#), [60](#), [61](#)]. However, their results require a number of assumptions. Firstly, they assume that the phononic environments at the different sites are uncorrelated, something which also holds for the biological system [[62](#)]. Secondly, they assume that site energies fluctuations are Gaussian and Markovian, corresponding to the infinite temperature limit with a broadband phonon spectrum. Finally, this model (the HSR model), in which the phonons affect the excitons but not *vice versa* ignores the *back-action* that occurs in quantum-mechanical systems and thus corresponds to a classical or thermodynamic limit.

Even with those restrictions in mind, this result vastly simplifies our sample construction task. Rather than needing to engineer new types of coupling to recreate the system-bath interactions, which would likely be fixed or only narrowly tunable, as long as

we are satisfied with a high-temperature limit, we can create the system-bath interactions by applying time-varying currents through our flux lines. By comparison, this is a relatively trivial process with modern arbitrary waveform generators (AWGs), and provides high degrees of flexibility. Not only can we, as originally formulated by the authors, apply Gaussian, Markovian noise (also referred to as *white* noise), but we can also *shape* or tune the noise spectrum to be more faithful to the FMO system, which has some broadband vibrational modes, but also narrower modes at specific frequencies [43, 31].

2.2.4 Physical Sample

The sample used for my experiments is depicted in Figure 2.2 where each qubit is in the same relative physical position as in the circuit diagram. My predecessors implemented the circuit using coplanar waveguides for the transmission line, resonator, and for the flux lines. A *transmon* parameter regime was used for the qubits, reducing their sensitivity to flux and charge noise while preserving anharmonicity that lets them act as two-level systems.

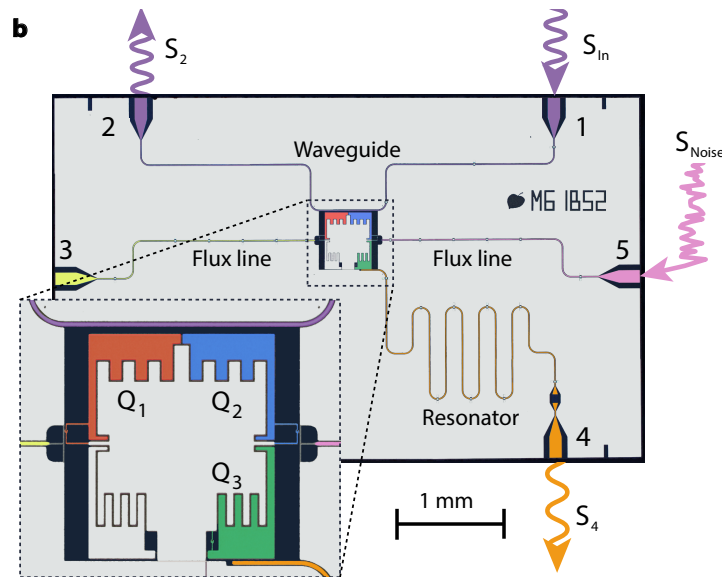


Figure 2.2: False-color micrograph of the sample used in my experiments. Silver or colored regions represent metal while black regions are bare substrate. The long meandering lines are flux lines, resonators, or coplanar waveguides. Within the central region, there are Josephson junctions and capacitor pads that create capacitive couplings to other circuit elements. The numbers of the ports correspond to the numbers in Figure 2.1. Adapted from [49].

The large, colored, crenelated structures visible in the center of the chip are the capacitive islands of the qubits. Close proximity of the capacitor pads leads to strong capacitive (dipole-dipole) coupling of the qubits, as is the case for qubits 1 (red) and 2 (blue). Similarly, pads for both of these qubits are near the light purple transmission

line, leading to capacitive coupling that is used to drive and probe these qubits. Since the green pad of qubit 3 is farther away, it is not affected by the transmission line, and is considered isolated. Instead, it has weak coupling to qubit 2 (note the thin peninsula of gray ground plane between the pads of these two qubits which partially shields the capacitive coupling) and strongly coupled to the orange output resonator. One end of the resonator is adjacent to qubit 3 while the other end is formed by an interdigitated capacitor (the circuit analog of a mirror) interrupting the coplanar waveguide.

The SQUID junctions reside on the thin looping bridges which extend to the left and right of qubits 1 and 2, or shielded in a cavity in the lower-middle of the sample for qubit 3. This places the SQUID loops of qubits 1 and 2 near the terminations of the flux-line waveguides, where currents are converted to magnetic flux. Thus, these flux lines achieve local control of qubits 1 and 2 while qubit 3 is partially shielded. The coil (not pictured) can be used to adjust qubit 3 to the correct regime, with the other qubits corrected using their flux line.

Note that there is an additional, unused capacitor pad in the lower left corner of the qubit region of the sample (Figure 2.2). This is included to reduce the differences between different sites on the chip, making the capacitance properties (and hence frequencies) more homogeneous and easier to predict.

The base of the chip is a highly pure sapphire (Al_2O_3) substrate on which an approximately 150 nm layer of niobium has been deposited (for more details on Niobium film creation, see [63]). Photolithography is followed by reactive ion etching to form the coplanar waveguides, resonators, and qubit capacitor pads. Since niobium has a critical temperature, T_c , above 4.2 K for thin films (approximately 9 K), the chip can be probed at this stage by microwave spectroscopy while in a liquid helium dipstick to check that the design frequencies for the different structures were achieved by the photolithographic process. After this verification, the junctions of the SQUID loops are created via shadow mask deposition of aluminum around a resist bridge created by electron-beam patterning of a dual-layer resist [53]. Aluminum is preferred for Josephson junctions because of its highly controllable oxide formation, which is used to form the several nm insulating barrier in the S-I-S Josephson junction, resulting in predictable junction impedances.

2.2.5 Simulation Standard Configuration

In order to test models of photosynthetic energy transport, we must choose the correct frequencies for each of the qubits. The energy-level diagram of the qubit configuration used throughout my experiments is shown in Figure 2.3. We place qubits 1 and 2 on resonance at 6.313 GHz to create hybridized bright and dark states at 6.433 GHz and 6.193 GHz respectively ($2J_{12}/2\pi = +240$ MHz). Furthermore, we tune qubit 3 to the same frequency as the dark state, creating hybrid states $|d_1\rangle$ and $|d_2\rangle$ at 6.166 GHz and 6.220 GHz respectively ($2J_{d3}/2\pi = 54$ MHz). These states couple to the resonator, which is fixed at 6.000 GHz due to its dimensions, via Purcell decay. The system parameters, including the Rabi and Purcell rates are presented in Table 2.1.

Now that I have detailed both the connectivity of the sample and the energy level configuration, we can touch on some of the finer points about design decisions. Bright

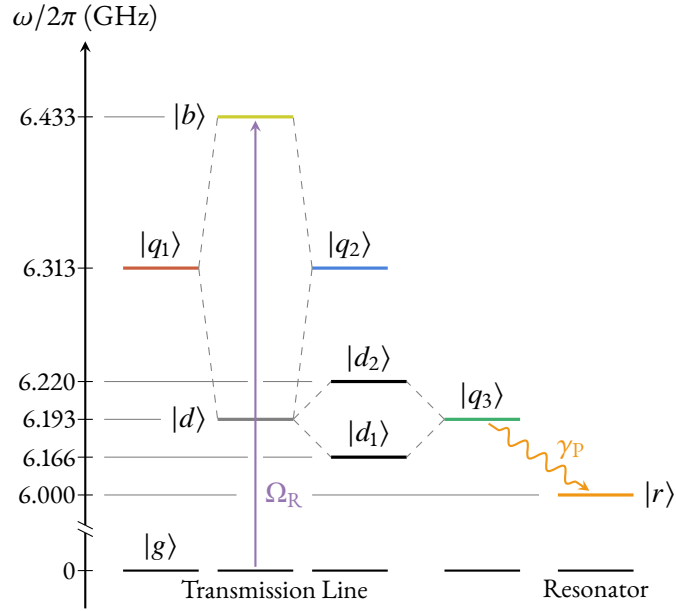


Figure 2.3: Energy level diagram of the sample when in standard simulation configuration. Qubits 1 and 2 are tuned in resonance, forming bright and dark states. Qubit 3 is brought into resonance with the dark state, forming states $|d_1\rangle$ and $|d_2\rangle$, which couple to the resonator via Purcell decay.

Table 2.1: Sample parameters in simulation standard configuration

Parameter	Value (MHz)
$\omega_1/2\pi$	6313
$\omega_2/2\pi$	6313
$\omega_3/2\pi$	6193
$\omega_r/2\pi$	6000
$2J_{12}/2\pi$	240
$2J_{d3}/2\pi$	54
Ω_R	21
γ_P	8
γ_b	10

and dark states are not present in the FMO complex. However, they do appear in other PPCs, and they have been suggested to increase energy transport efficiency [64, 65, 66, 67, 68], and hence we have decided to use them here. The configuration of the third qubit follows the suggestion by Huelga and Plenio to maximize energy transport efficiency in a network of three qubits [31]. Finally, not only does the resonator provide Purcell tuning of the decay rate into the microwave line, but the strong coupling also leads to static coherence, which has been suggested to be one mechanism that could boost transfer efficiency even in the presence of incoherent excitation [32], and which is a feature that we wish to observe in this round of time-resolved measurements. This configuration demonstrates two types of energy transfer: incoherent transfer from the bright state to the dark state induced by noise, and coherent transfer from the dark state to qubit 3 as a result of the strong coupling between those states.

One additional detail is that in our system, the coupling between sites, J_{12} , is positive, meaning that the bright, symmetric superposition is higher in energy than the dark, antisymmetric superposition, the opposite of the usual case for electronic wavefunctions, where the HOMO is usually symmetric while the LUMO is antisymmetric. While this case may be unusual within biological PPCs, it is not uncommon, with H -aggregates of organic dyes also having the same hypsochromic shift of the visible state.

2.2.6 Flux Noise

Now that I have presented the energy-level diagram of the system, we can again discuss the flux noise that will be used in the experiments. As specified by the HSR model, we will use broadband white noise with a bandwidth that includes the $|b\rangle$ - $|d\rangle$ frequency difference (white noise with a reduced bandwidth merely dephases the qubits without leading to transport from the bright to dark state [49]). In addition, we will use shaped noise that recreates the biologically observed sharp phononic mode, *i.e.* noise with a Lorentzian lineshape, a *non-Markovian* bath that behaves as if it had some memory. Following evidence in the FMO complex [43], we will place this mode at the $|b\rangle$ - $|d\rangle$ frequency difference.

2.3 Experimental Apparatus

I performed the experiments in the following chapter using a standard setup for measurements of superconducting transmon circuits. This consists of a dilution refrigerator to cool the sample down to millikelvin temperatures, microwave electronics to apply signals to the sample and to measure the response, and a system to generate flux noise.

2.3.1 Dilution Refrigerator

In order to bring the sample to a regime where it is superconducting and where the thermal excitations of the system are suppressed far below the energy scales of the qubit, I had to cool the sample down to around 15 mK. This was done using a BlueFors LD250 *dilution refrigerator* (DR), a type of multi-stage cryogen-free refrigerator frequency used

in cryogenic experiments. The primary cooling stage consists of a two-stage *pulse-tube cooler*, a heat engine that uses helium as a working gas to reduce the temperature to approximately 3 K. As the second stage of the DR, a *dilution unit* uses mixing and separation of ^3He from superfluid ^4He to produce additional cooling power in order to reach 10 mK [69]. In between these special stages, there are other stages such as the 50 K stage and the 1 K “still” stage in order to reduce the radiation load on subsequent heat stages or to perform heat-exchanging functions.

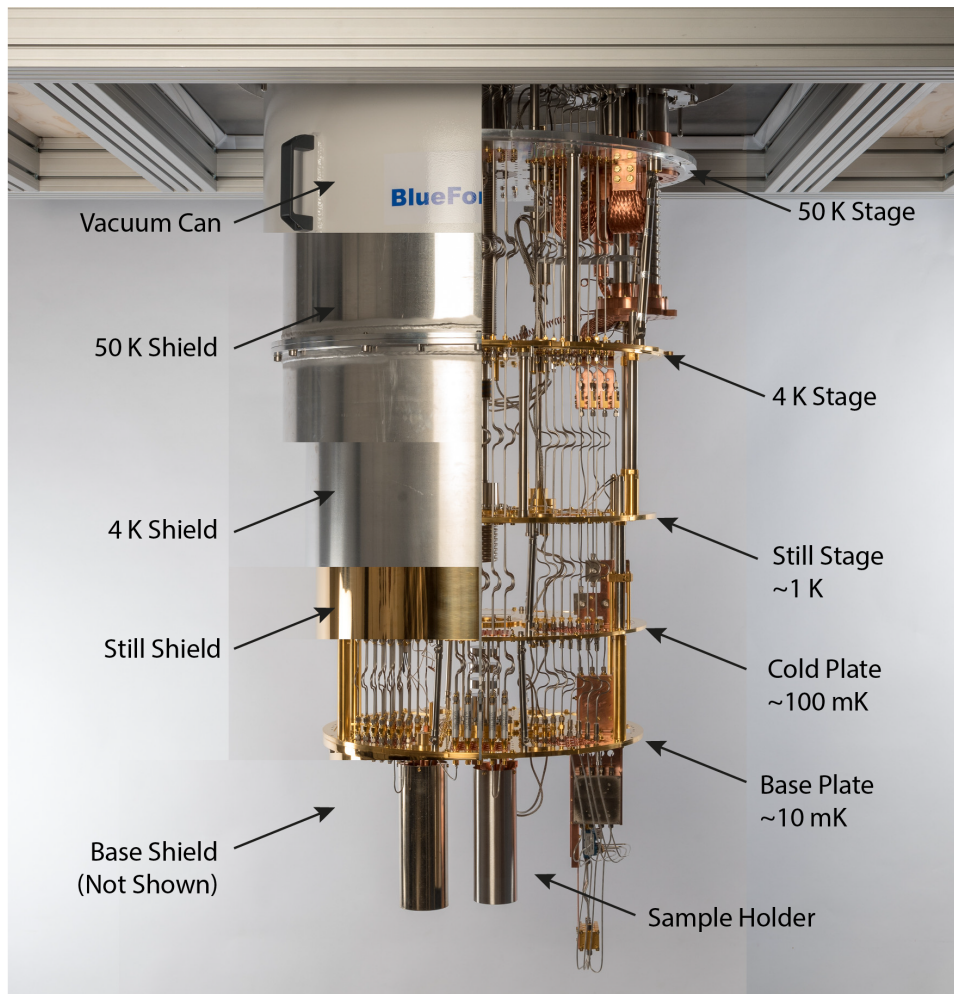


Figure 2.4: Composite photograph revealing different temperature stages of a dilution refrigerator along with the various stages of shielding. Note that this is a BlueFors XLD400 which is significantly larger than the LD250 used in our experiments, and is only shown for demonstration purposes. Photo and editing by Janis Lütolf; used with permission.

At the very bottom of the dilution refrigerator, on the coldest stage, the sample chip (sapphire wafer) is placed onto a printed circuit board (PCB) with microwave connectors,

enclosed inside a mostly light-proof metal enclosure, and then fixed to the base plate of the fridge. The sample is surrounded with two layers of high-magnetic permeability metal (μ -metal), which acts as a magnetic shield, reducing the magnetic field around the sample.

Even though the sample may be cold and well-shielded, in order for it to be useful, we need ways to control and measure the sample. At room temperature, this might be easy, but the need to shield the sample from room temperature radiation dictates a more complicated setup shown in [Figure 2.5](#). Input lines to the transmission line and resonator have several stages of attenuation to reduce the thermal noise carried from room temperature to cold stages. For the flux lines, this is slightly modified, since the attenuators function as voltage dividers and thus limit the amount of current that can be applied to the flux line. Here, additional low pass filters (cutoff frequency: 780 MHz) are used to eliminate high-frequency noise which would dephase the qubits. We measure both the transmission line and the resonator in reflection, which dictates a circulator on the input line for both of these components.

In order to amplify the extremely weak signals³ from the sample, we use several stages of amplification. Since the noise of an amplified signal is dominated by the noise of the first amplifier, we use the best available amplifiers. For the resonator, we use a *travelling-wave parametric amplifier* (TWPA) graciously provided by MIT's Lincoln Laboratory. For both output lines, the next stage is a *high-electron mobility transistor* (HEMT) amplifier (Low Noise Factory LNC4.8A for the resonator and LNC1.12A for the transmission line). These lines use band-pass filters and circulators to prevent amplified noise from reaching the sample and to limit the bandwidth of noise that reaches later stages of amplification.

2.3.2 Microwave Generation and Measurement

The generation of microwave signals is split into two categories: continuous-wave (CW) signals and pulsed signals. All CW tones can be directly generated using commercial microwave generators. Pulse generation, on the other hand is limited by current electronics to working at lower frequencies, so a classic heterodyne architecture is used for up-conversion of signals from intermediate frequency (IF) to radio frequency (RF). We use Agilent E8257D PSG analog signal generators as the local oscillator (LO) of these heterodyne circuits or as probe tones and a Rhode&Schwarz SGS100A SGMA RF source as the pump for our TWPA. Pulses are generated via a Tektronix AWG520 AWG which has a sample rate of 1 GS s^{-1} and a vertical resolution of 10-bits.

Signals emerging from the output ports of the fridge pass through a custom-built amplification and down-conversion circuit, depicted in [Figure 2.6](#), in order to increase their amplitude and reduce their frequency until they reach the domain where they can be sampled. The signals are captured by an Abaco FMC110 two-channel, 1 GS s^{-1} , 14-bit analog-to-digital converter (ADC). We collect the data from the ADC using a Xilinx Virtex-6 FPGA where we perform digital down-conversion (DDC) to get a zero

³A single microwave photon has an energy of just $\hbar\omega = 4.0 \times 10^{-24} \text{ J}$ at 6 GHz, five orders of magnitude less than optical photons where $\hbar\omega = 3.3 \times 10^{-19} \text{ J}$ at 600 nm

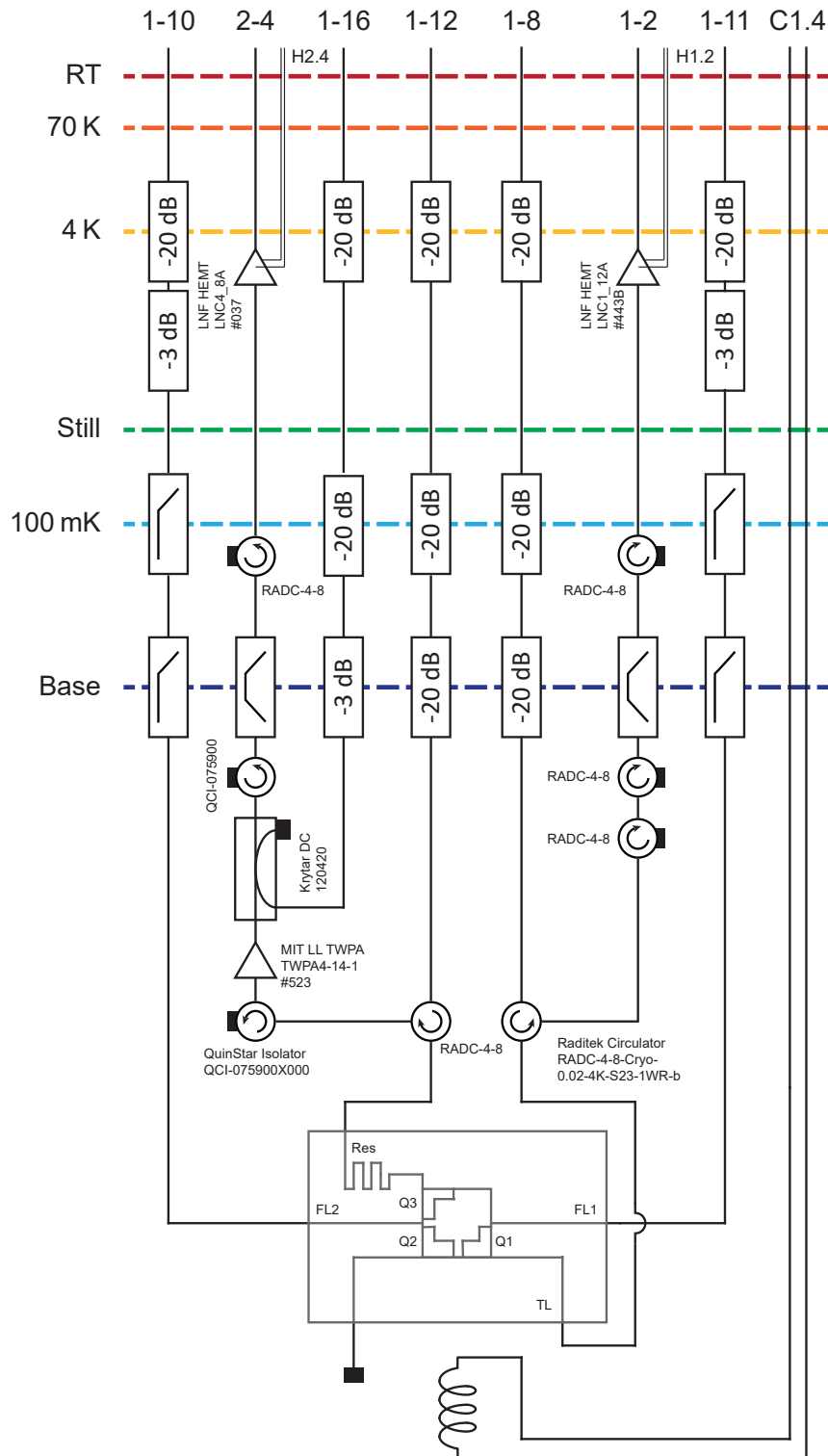


Figure 2.5: Cabling diagram of the refrigerator during my experiments. Partially adapted from [55].

frequency signal which subsequently undergoes significant real-time signal processing in our custom-designed FPGA applications [70].

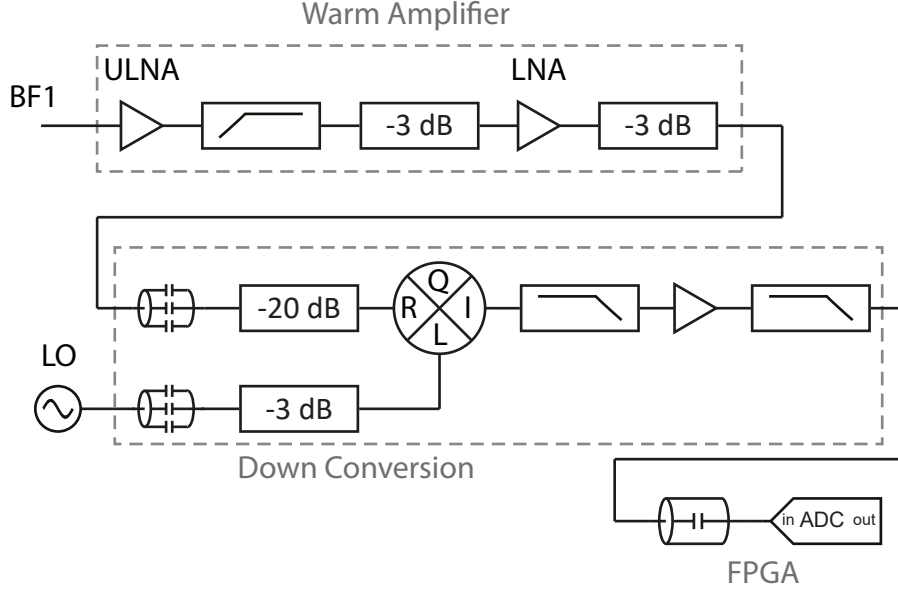


Figure 2.6: Schematic diagram of warm amplification, down-conversion, and digitization modules for signals returning from fridge.

In addition to these microwave electronics, we have Stanford Research Systems SIM928 isolated voltage sources to DC bias our flux lines and coil. Experiments are controlled using a custom LabVIEW application called *SweepSpot* which was developed by Simon Storz during his Master's thesis [71].

2.3.3 Noise Generation

I generated flux noise at the sample following the method outlined by Bargerbos [55]. In brief: we start with an independent random variable, X , with zero mean ($\mu_X = 0$) and finite variance ($E(X^2) = \sigma^2 < \infty$), a practical example of which is the *Gaussian* or *normal* distribution. The covariance function for this distribution is

$$\gamma_X(h) = E(X_{t+h}X_t) = \begin{cases} \sigma^2 & \text{if } h = 0 \\ 0 & \text{otherwise} \end{cases}$$

due to the independence of the random variable at different times. Applying the definition of a spectral density [72] and noting that we satisfy the criterion $\sum_{h=-\infty}^{\infty} |\gamma(h)| < \infty$, we

find

$$\begin{aligned} f(\lambda) &= \frac{1}{2\pi} \sum_{h=-\infty}^{\infty} e^{-ih\lambda} \gamma(h) \\ &= \frac{1}{2\pi} \gamma(0) \\ &= \frac{\sigma^2}{2\pi} \end{aligned}$$

so the spectrum of this random variable is completely uniform across all frequencies. By sampling randomly from this distribution, we create a time series, $\{x_t\}$, that shares these properties, *i.e.* a time series of perfect white noise [72].

To create a particular noise spectral density from this, we filter the time series data. For the white noise, since our AWG does not have infinite bandwidth (which would imply infinite power), we limit the bandwidth to a value within the sampling rate of the AWG, given by a Fermi-Dirac spectral density

$$S_{\text{FD}}(\omega) = \frac{A}{e^{(\omega-\omega_C)/2\pi B} - 1} \quad (2.4)$$

where A parameterizes the amplitude, ω_C is the cutoff frequency, and B parameterizes the “steepness” of the decline from full density to no density. For Lorentzian noise, we use the following spectral density function:

$$S_{\text{L}}(\omega) = \frac{A}{\left(\frac{\omega-\omega_C}{\pi B}\right)^2 + 1} \quad (2.5)$$

where A again characterizes the amplitude, ω_C is now the center frequency, and B is the full-width half-maximum (FWHM). We take the square root of the spectral densities (to go from power to voltage values), Fourier transform, discretize, and then truncated them at a finite number of points in order to create *finite-impulse response* (FIR) filter kernels, k_n . To produce the final (filtered) time series, $\{x'_t\}$, we convolve the time series with the FIR filter, *i.e.*

$$x'_t = \sum_{n=0}^K k_n x_{t+n}$$

where K is the length of the filter.

When generating broadband noise, we have to take an additional step to correct for the analog performance of the AWG. We measure the spectrum produced by the instrument for a uniform noise input file (up to the sampling rate of the AWG). Since we use a uniform input, the transfer function is trivially given by the measured power spectral density, $S(\omega)$ divided by the specified amplitude A ,

$$h(\omega) = \frac{S(\omega)}{A}.$$

In order to correct the signal generation, we multiply the FIR filter kernel for the Fermi-Dirac white noise by the square root of the inverse transfer function

$$k'_n = k_n \sqrt{h^{-1}(\omega_n)} = k_n \sqrt{\frac{A}{S(\omega_n)}}.$$

The final voltage time series is then uploaded to a second Tektronix AWG520, which converts the digital signals to a physical voltage which is connected to flux line 2 of the sample. The voltage is reduced by attenuators in the line and we can model the final attenuator as a resistor, dividing the voltage between the flux line and ground. With this resistance, and knowledge of the impedance of the flux lines, we can compute the current produced at the sample by a given voltage.

In the experiments that I will present below, we used white noise with a cutoff frequency of 300 MHz and shaped noise with a Lorentzian lineshape at a frequency of 246 MHz and a FWHM of 10 MHz. The results of the noise generation procedure outlined above compared with the expected values are presented in [Figure 2.7](#). Extremely observant readers might notice significant differences between these figures and the ones presented in [\[55\]](#); this is due to the difference of AWG. The Tektronix AWG520 does not have as high of a peak output voltage as the Tektronix AWG5014 used in previous experiments (2 V versus 4.5 V), so the amplitude of the noise is reduced. To overcome this restriction, a low-frequency amplifier with 16 dB of gain was used whenever greater amplitudes were required. In addition, the white noise spectrum deviates from the expected values, even after correcting for the analog performance of the AWG. We believe that this is due to the lower vertical resolution of the AWG520 compared to the AWG5014 (10 bits versus 14 bits).

In the measurements below, I will plot data as a function of flux power rather than AWG voltage in order to make the data more general; for details on how I performed this conversion, see [section C.2](#).

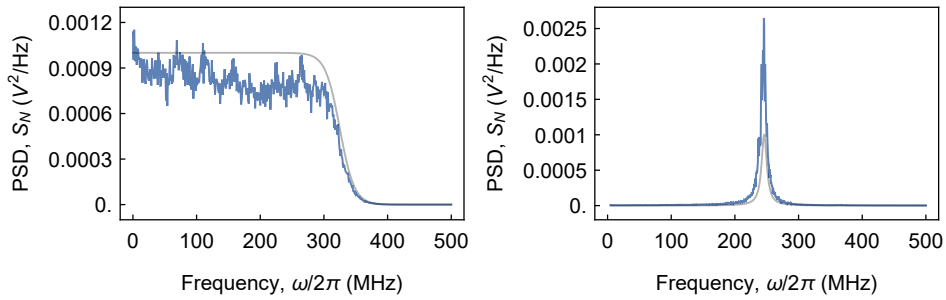


Figure 2.7: Power spectral density, S_N , of the generated noise. *Left*: white noise, with a cutoff frequency of 300 MHz. *Right*: Lorentzian noise with a center frequency of 246 MHz and a FWHM of 10 MHz. Expected noise shown in light gray, generated noise shown in blue.

Chapter 3

Results and Discussion

3.1 Hamiltonian Characterization Measurements

Before moving on to measurements of the system's dynamics, it is important that we first calibrate the parameters of the Hamiltonian, including qubit frequencies and the effect of the flux noise. This is needed not only for simulations to check the validity of our results, but to be able to place the system in simulation configuration and ensure that the noise is functioning as intended.

3.1.1 Mutual Inductance and Maximum Frequency

In order to calculate the frequencies of the various qubits at different flux line or coil voltages (corresponding to different currents and hence different magnetic fluxes), I performed measurements to extract the maximum frequencies of the qubits and their mutual inductances with the flux lines. The usual measurement for these parameters is the *coil sweep*, where the electric field response of the system to a continuous microwave probe tone is measured as both the frequency of the tone and the voltage applied to the coil (or flux line) is varied. When the frequency of the probe tone corresponds to the frequency of an eigenstate of the system, the amplitude of the signal will decrease for reflected signals or increase for transmitted signals. Transmitted signals, where the probe tone is applied to one port but observed from another, will only appear when there is sufficient hybridization between qubits visible at each of the ports involved.

A coil sweep that I performed on our sample is presented in [Figure 3.1](#). The general trend in the plots is that the frequency of the qubits changes in a roughly parabolic shape, which is expected since the transition frequency of a SQUID should vary proportionally to $|\cos(\Phi/\Phi_0)|$ —which can be approximated as a parabola for small amplitudes—as the coil voltage and hence magnetic flux (Φ) is swept. Additionally, the changes in qubit frequency are periodic with respect to coil voltage, again, as expected for SQUIDS due to the cosine dependence on the external magnetic flux. Qubit 3 can always be seen in the resonator, since it is directly coupled there, but qubits 1 and 2 can only be seen when they partially hybridize with qubit 3.

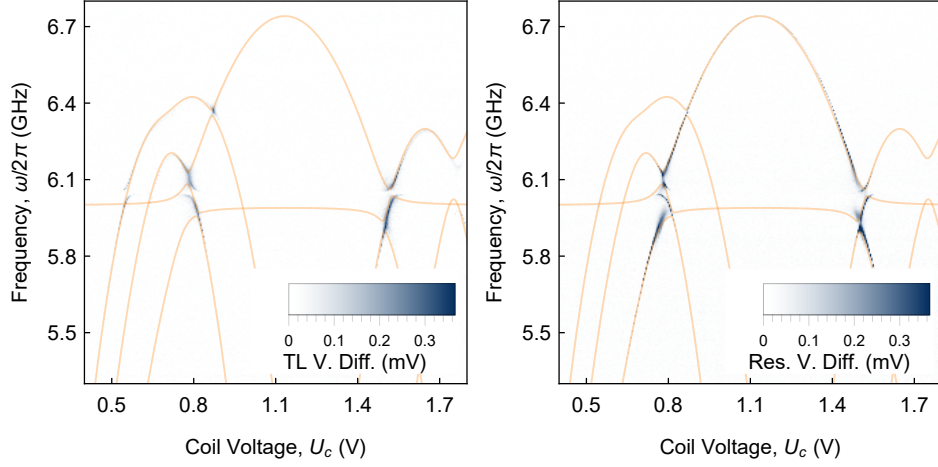


Figure 3.1: Coil sweep of the sample with the probe tone applied to the resonator and no voltage applied to the flux lines. *Left*: transmitted voltage measured in transmission line. *Right*: reflected voltage measured in the resonator. In both figures, the background signal has been subtracted to produce a voltage difference plot. Translucent orange lines are a manual fit using a simple model presented below.

As can be seen from the orange lines in the figures, we can recreate the behavior of the system by fitting to a simple model. In this case, I have plotted the eigenvalues of a simple matrix:

$$H(U_c, U_1, U_2) = \begin{pmatrix} \omega_1 & J_{12} & J_{13} & g_{1r} \\ J_{12} & \omega_2 & J_{23} & g_{2r} \\ J_{13} & J_{23} & \omega_3 & g_{3r} \\ g_{1r} & g_{2r} & g_{3r} & \omega_r \end{pmatrix} \quad (3.1)$$

as a function of coil voltage, U_c , flux line 1 voltage, U_1 , and flux line 2 voltage, U_2 . Note that in this equation, each variable (except for ω_r) will be dependent on U_c , U_1 , and U_2 , but these were omitted for brevity. More explicitly, taking the voltage dependence of the parameters to be:

$$\omega_j(U_c, U_1, U_2) = \omega_{j,0} \sqrt{|\cos[\pi(-a_j + b_j U_c + c_j U_1 + d_j U_2)]|} \quad (3.2)$$

and:

$$X_{j\alpha}(U_c, U_1, U_2) = X_{j\alpha,0} \frac{\sqrt{\omega_j(U_c, U_1, U_2)\omega_\alpha(U_c, U_1, U_2)}}{\sqrt{\omega_{j,0}\omega_{\alpha,0}}} \quad (3.3)$$

where $X \in \{J, g\}$, $j \in \{1, 2, 3\}$, $\alpha \in \{1, 2, 3, r\}$, $\omega_{\alpha,0}$ represents the maximum frequency of a qubit or resonator, and $X_{j\alpha,0}$ is the no-field coupling between qubit j and circuit element α . The frequency-dependent coupling term comes from the capacitive coupling between the qubits (see [subsection A.4.1](#)). Since the resonator does not include any

SQUIDS, the resonator frequency does not depend on the applied magnetic field. a_j , b_j , c_j , and d_j are parameters that specify each qubit's effective flux offset and mutual inductance with the different voltage sources. We can relate voltage to flux via the following matrix:

$$\begin{pmatrix} \varphi_1 \\ \varphi_2 \\ \varphi_3 \end{pmatrix} = M \begin{pmatrix} U_1 \\ U_2 \\ U_3 \end{pmatrix} + \begin{pmatrix} O_1 \\ O_2 \\ O_3 \end{pmatrix}$$

where

$$M \equiv \begin{pmatrix} b_1 & c_1 & d_1 \\ b_2 & c_2 & d_2 \\ b_3 & c_3 & d_3 \end{pmatrix},$$

$O_j = a_j$, and the b , c , and d coefficients have units of magnetic flux quanta per volt.

A fit of these eigenvalues to a coil sweep can only determine the b and a parameters; to measure the remaining two types, we must perform voltage sweeps of the flux lines while keeping the coil at a fixed voltage. By doing this in a systematic way, it is possible to calibrate the entire mutual inductance matrix. From our measurements, we recovered:

$$M = \begin{pmatrix} -0.91 & -0.04 & 0.02 \\ -1.05 & 0.01 & -0.28 \\ 0.57 & -0.01 & -0.021 \end{pmatrix}.$$

It is clear that the coil (first column) strongly affects all qubits, that flux line 2 strongly affects qubit 2, but that flux line 1 does not affect the qubits. The reason for this is not completely known, but we suspect a collapsed airbridge over FL1. We had an issue in the past with a collapsed airbridge on FL2 that we were able to correct, and applying currents to FL1 warms up the fridge significantly more than applying the same current to FL2 does, indicating some fault as the flux lines should be superconducting and largely dissipationless.

The maximum frequencies and coupling rates of the different circuit elements are presented below in [Table 3.1](#). Some observers may note that the maximum frequencies are reduced compared to previous measurements with the same sample [55], having shifted downwards by between 200 MHz and 450 MHz. We believe this drop in maximum frequency to be due to aging of the junction that reduces E_J [73, 74].

Knowing the response of the system to the magnetic fields that we could apply, we could now place the system in standard configuration. The dysfunctional flux line 1 restricted arbitrary configuration of the system, but we were able to reach standard configuration of the system through flexibility in which flux period we used. Unfortunately, this had to be a functional standard configuration rather than the ideal configuration, *i.e.* we were able to position the qubits such that they recreated the correct bright and dark states, but with slightly reduced coupling, since it was not possible to get qubit 2 to reach the target frequency of 6.313 GHz. We did not move to frequencies below the resonator (which has symmetric dynamics) since this places the qubits far away from their flux sweet spots, making them highly sensitive to flux noise and leading to greater frequency drifts over time.

Table 3.1: System frequency and coupling parameters

Parameter	Value (Hz)
$\omega_{1,0}/2\pi$	6.41×10^9
$\omega_{2,0}/2\pi$	6.29×10^9
$\omega_{3,0}/2\pi$	6.73×10^9
$\omega_r/2\pi$	6.00×10^9
$J_{12,0}/2\pi$	83.6×10^6
$J_{13,0}/2\pi$	8.5×10^6
$J_{23,0}/2\pi$	36.7×10^6
$g_{1r,0}/2\pi$	1×10^6
$g_{2r,0}/2\pi$	0.2×10^6
$g_{3r,0}/2\pi$	9×10^6

3.1.2 Rabi Rate

In order to deterministically excite the system into different states, we must characterize the strength with which we drive our system through the different ports, known as the *Rabi rate*. The method that we have used to characterize this is time-resolved: we apply pulses of different duration or amplitude and observe the response of the state. Steady-state measurements such as a Mollow triplet measurement can also calibrate Rabi rates, but they do not provide calibrated qubit rotation pulses which are needed for later measurements. Since we typically excite the bright state, I will focus on Rabi measurements of the bright state through the transmission line. An example measurement is plotted in [Figure 3.2](#). Due to our connectivity, we measure electric field ($\propto a + a^\dagger$), so our signal is maximized when the qubit is in the superposition state (the equatorial plane of the Bloch sphere). Thus the first maximum of the blue and yellow traces correspond to rotations of $\frac{\pi}{2}$. As the signal amplitude is increased, the rotation angle increases, until (for the blue trace), the rotation angle reaches π , meaning that the qubit has been transferred to the excited state. The excited state has no average electric field, so our measured signal is minimized for a π pulse. Continuing to increase the amplitude eventually leads to a $\frac{3\pi}{2}$ pulse. At the same electric field amplitude, shorter pulse lengths reduce the rotation angle by reducing the interaction time, explaining the slower oscillation of the 4 ns trace compared to the 10 ns one.

In order to minimize the time needed to prepare the system in a given state, we used short square pulses, which have a broad spectral spread (for more information, see [section C.1](#)). Thus, especially for rotation angles greater than π , we lose signal due to transitions to higher-lying states (*f, h, etc.*), reducing the contrast of the Rabi trace.

Knowing the pulse length to achieve different qubit rotations leads directly to the Rabi driving rates of these pulses. The Rabi rate, Ω_R , corresponds to the following

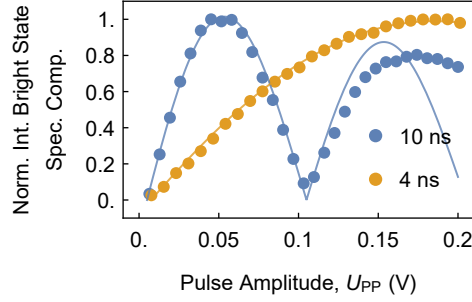


Figure 3.2: Rabi measurement of the bright state through the transmission line. The normalized integrated bright state spectral component (a measure of the electric field amplitude at the frequency corresponding to the bright state) is plotted versus pulse amplitude for two pulse lengths, 4 ns and 10 ns. Filled circles are data, solid lines are a fit to an exponentially damped absolute-value sinusoid.

formula:

$$\Omega_R = \frac{\theta}{2\pi} \frac{1}{t}$$

where θ is the rotation angle of the pulse and t is the length of the pulse in seconds. Thus, for the 10 ns pulse of [Figure 3.2](#) rotating the state by $\pi/2$, we get a Rabi rate of 25 MHz. The experiments below predominantly used pulse lengths of 12 ns, corresponding to $\Omega_R/2\pi = 42$ MHz for π pulses and 21 MHz for $\pi/2$ pulses. For more discussion on the Rabi measurement procedure, including discussion on the data processing, see [section C.4](#).

3.2 Environment Characterization Measurements

Now that we have characterized the parameters of the three-qubit system, it is time to characterize the environment around that system. This includes the radiative Purcell decay rate of qubit 3 coupled to a resonator that together simulate the trapping rate of the sites near the reaction center, the intrinsic dephasing rate of the qubits, corresponding roughly to homogeneous broadening of the chromophore lineshapes, and the dephasing rate produced by the flux noise which acts as the phononic bath surrounding the qubit “chromophores” (inhomogeneous broadening).

3.2.1 Purcell Decay Rate

The Purcell effect, as mentioned previously, modifies the emission rate of a system depending on its electromagnetic environment. For the particular case of a qubit capacitively connected to an output line through a resonator, we can follow the work of *Sete et al.*

and write the Purcell rate as

$$\gamma_P = \frac{\kappa_r}{2} - \frac{\sqrt{2}}{2} \sqrt{-B + \sqrt{B^2 + (\kappa_r \Delta_{3r})^2}} \quad (3.4)$$

where

$$B \equiv \Delta_{3r}^2 + 4g_{3r} - \frac{\kappa_r^2}{4},$$

κ_r is the resonator loss rate into the transmission line, g_{3r} is the resonator-qubit 3 coupling, and Δ_{3r} is the resonator-qubit 3 detuning [75].

To measure the Purcell rate, we place the system in a configuration where qubit 3 is isolated from the other qubits by at least 2 GHz and perform spectroscopic sweeps at different coil voltages. As the magnetic field tunes the frequency of the qubit relative to the fixed frequency of the resonator, the linewidth changes due to the differing Purcell rate. We numerically fit a Lorentzian lineshape to the data to extract the linewidth and center frequency of qubit 3 at these different coil voltages and plot the linewidth (corresponding to the Purcell rate plus the intrinsic dephasing rate of qubit 3) versus the detuning, as shown in Figure 3.3. Since our simulation configuration involves having the qubit state transition frequencies above the resonator frequency, I measured the Purcell rate for positive detunings (qubit 3 above resonator). The gray dashed lines in Figure 3.3 correspond to Equation 3.4 with a resonator frequency, $\omega_r/2\pi$, of 6.00 GHz, a resonator loss rate, $\kappa/2\pi$, of 110 MHz, and a resonator-qubit coupling, $g_{3r}/2\pi$, of 60 MHz. Using these values, we find that in the standard configuration, with qubit 3 at a frequency of 6.193 GHz, we have a Purcell decay rate of $\gamma_P/2\pi = 8$ MHz, in line with the previously published results [49] and the linewidths of the dark states in the resonator.

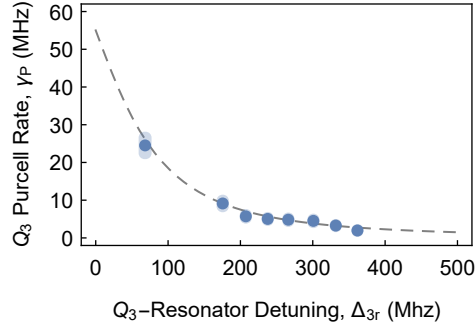


Figure 3.3: Purcell rate of qubit 3, $\gamma_P/2\pi$, as a function of resonator-qubit 3 detuning, $\Delta_{3r}/2\pi$. Data with standard error plotted as blue circles with translucent error regions, Equation 3.4 with $\omega_r/2\pi = 6.00$ GHz, $\kappa_r/2\pi = 110$ MHz, and $g_{3r}/2\pi = 60$ MHz plotted as the gray dashed line.

3.2.2 Intrinsic Dephasing Rate

The intrinsic dephasing rate of a qubit, which I will call γ_I , corresponds to the linewidth of an atomic transition in quantum optics: it is the measured linewidth of the qubit in

the absence of all added dephasing and thus includes only dephasing due to defects in the sample with fluctuating electric fields, any high frequency magnetic field fluctuations that are not removed by the shielding, *etc.*, all outside of experimental control. To measure the intrinsic dephasing rate, we perform spectroscopy on an isolated qubit as we reduce the probe-tone power. Since the probe field dephases the qubit, the linewidth will decrease as the drive power decreases. At some point, the dephasing rate caused by the drive will fall below the intrinsic dephasing, and the measured linewidth will saturate. I have plotted this for qubit 3 in Figure 3.4, which saturates at $\gamma_{1,3}/2\pi = 1.8$ MHz.

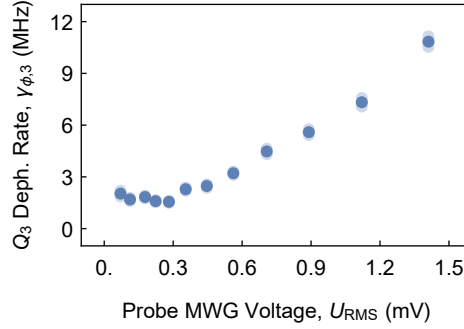


Figure 3.4: Dephasing rate of qubit 3, $\gamma_{\phi,3}/2\pi$, as a function of probe tone RMS voltage, U_{RMS} . Data with standard error plotted as blue circles with translucent error regions. We see a linear dependence on the driving voltage until the dephasing rate saturates at 1.8 MHz, the *intrinsic dephasing rate*, γ_1 .

3.2.3 T_1 , T_2 , and Dephasing Rate

For any quantum system, there several time-domain parameters that describe how long the system retains quantum information, for different measures of “quantum information”. The most important are the *energy relaxation time*, T_1 , the time that the qubit takes to decay from the excited state to the ground state, and the *phase coherence time*, T_2 , the time that the qubit remains in a specific superposition state. On the density matrix of a single qubit in the usual computational basis, these show up as exponential decays of the excited state diagonal component (population) and of the off-diagonal components (coherences) respectively. A simple formula connects the two times:

$$\frac{1}{T_2} = \frac{1}{2T_1} + \frac{1}{T_\phi} \quad (3.5)$$

which is derived in many sources, including [54]. The new term in the above equation, $1/T_\phi$ is known as the *pure dephasing rate* and the result of any processes that induce decoherence without causing the qubit to decay, *i.e.* dephasing. In our experiments, the pure dephasing rate is the intrinsic dephasing rate plus any dephasing due to applied noise or drive tones, $1/T_\phi = \gamma_\phi = \gamma_1 + \sum \gamma$.

Relaxation Time

The general procedure to measure T_1 is to excite the qubit and then record the probability to find the qubit in the excited state as a function of time; an exponential fit to this decay gives the T_1 time. In our case, because we capacitively couple our qubits to output lines rather than using the dispersive shift of a cavity to detect the state, our natural measurement basis is the electric field of the qubit (similar to nuclear magnetic resonance [NMR] where they are sensitive to the transverse magnetic field component of the spins) rather than populations, and so we use a slightly different technique borrowed from NMR known as *inversion recovery* in which T_1 is extracted from a series of electric field time traces rather than from a population time trace. For more information on how I measured T_1 times, including a comparison with the “standard” cQED technique, see [section C.5](#).

For qubits 1 and 2 in isolated configurations without any applied flux noise, we measured T_1 times of (24 ± 1) ns. Once brought into simulation configuration, we measured the T_1 times in [Figure 3.5](#). The bright state starts off with T_1 times around 17.5 ns with no applied flux noise, but as soon as noise is added, there is a decrease to 16 ns to 17 ns for both white noise and Lorentzian noise. At high flux noise powers, the T_1 value of the white noise collapses as the dephasing rate interferes with qubit excitation. For the Lorentzian noise this is not an issue.

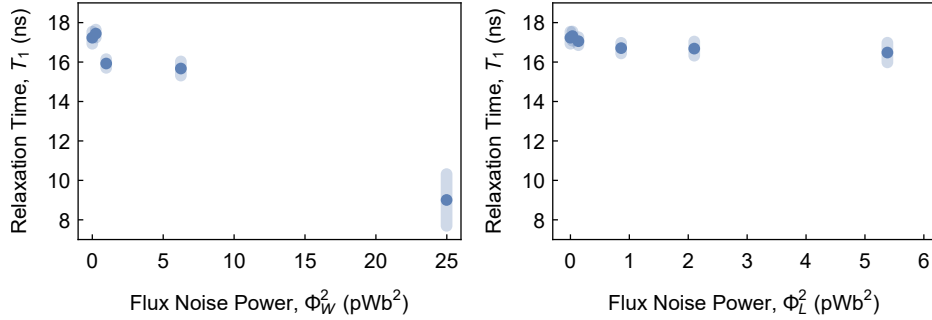


Figure 3.5: T_1 time of the bright state versus flux noise power for white noise (*left*) and Lorentzian noise (*right*). Data plotted as solid blue circles; standard error depicted in translucent regions.

Coherence Time

T_2 times are generally measured via a “Ramsey” pulse sequence, in which the probability of finding the qubit in the excited state is recorded versus delay between two resonant $\pi/2$ pulses (for more details on the measurement procedure, see [section C.6](#)). In our case, we recover T_2 by the equivalent of the cQED method for measuring T_1 : we apply a $\pi/2$ pulse and record the electric field as a function of time. The rate of the exponential decay corresponds to $1/T_2$.

When measuring qubits 1 and 2 in isolation, we recover T_2 times of (47 ± 1) ns and (49 ± 1) ns respectively, which agrees well with Equation 3.5 and the isolated T_1 times, assuming a small intrinsic dephasing rate, indicating that we are T_1 limited and cannot extend the phase-coherence time through refocusing, dynamical decoupling, or other techniques. Measurements of the bright state versus flux noise power are presented in Figure 3.6. T_2 times start at values twice the T_1 times, at 32 ns and decay with increasing noise power, as expected from Equation 3.5 with increasing pure dephasing. For the white noise, this decay is rapid and saturates at values of around 18 ns for noise powers greater than 5 pWb^2 . This is partially due to the configuration of the qubits where qubit 2 is only 25 MHz from its flux “sweet spot”, limiting the possible frequency shifts (and hence dephasing) due to the flux noise. Lorentzian noise, on the other hand, sees an almost linear decrease from 28 ns to 18 ns. Both noise types show an initial drop from no applied noise to the first point at extremely low applied noise powers, likely due to some constant-intensity $1/f$ noise introduced by the AWG electronics which adds additional dephasing to the qubit.

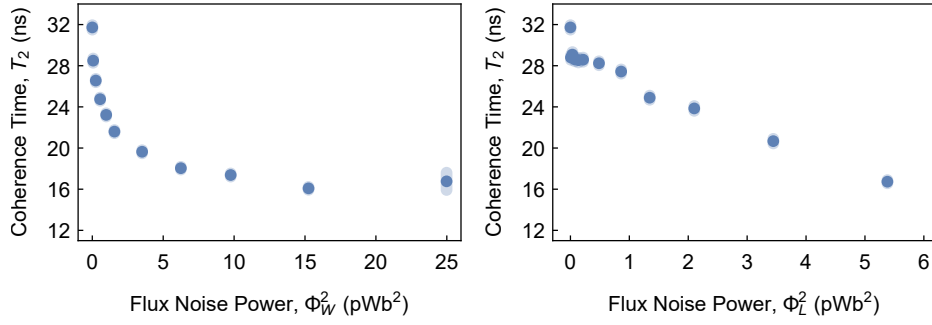


Figure 3.6: T_2 time of the bright state versus flux noise power for white noise (*left*) and Lorentzian noise (*right*). Data plotted as solid blue circles; standard error depicted in translucent regions.

Dephasing Rate

Dephasing rates are calculated rather than measured, inferred from T_1 and T_2 measurements using Equation 3.5 and assuming negligible intrinsic dephasing rates. Although qubit 3 had an intrinsic dephasing rate of 1.8 MHz, as I discussed above, the isolated T_1 and T_2 times for qubits 1 and 2 correspond to the predicted values with very small intrinsic dephasing rates, justifying the assumption when calculating dephasing rates.

Bright state dephasing rates for white and Lorentzian noise are presented in Figure 3.7. Both noise types reach dephasing rates of around 30 MHz, without premature saturation. Since we see the drop in T_2 as the AWG is enabled, this becomes a jump in dephasing rate, observed in the Lorentzian noise. These dephasing rates are below the values reached in [49], however, as I previously mentioned, our qubits have aged, placing the standard qubit configuration closer to the flux sweet spot of some of the qubits, where they have reduced sensitivity to external flux noise. As with the T_2 measurements, the Lorentzian

noise shows a quasi-linear scaling with noise power, as expected, while the white noise shows super-linear behavior followed by a gradual increase to the maximum dephasing. This shows the difference in dephasing potential of the two different types of noise: white noise strongly dephases the bright state, eventually hampering our ability to even excite the state while Lorentzian noise provides a more focused dephasing only where it is beneficial to the energy transfer without hampering excitation of the bright state (note the lack of collapse in the T_1 measurement).

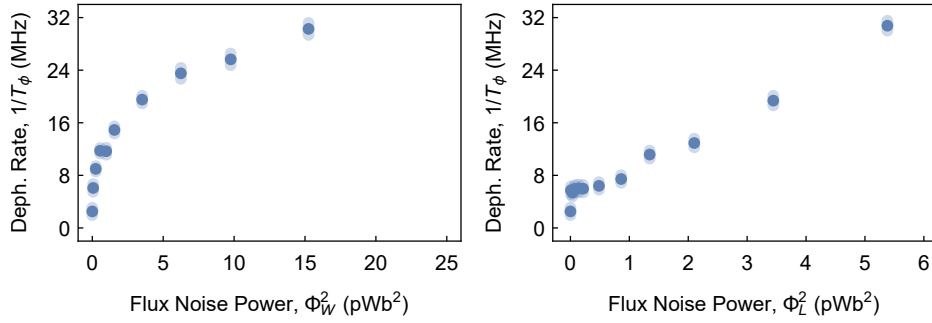


Figure 3.7: Dephasing rate of the bright state versus flux noise power for white noise (*left*) and Lorentzian noise (*right*). Data plotted as solid blue circles; standard error depicted in translucent regions.

Comparison with Linewidths

The above measurements were all performed using time-domain techniques. However, just as with atomic optics, we should be able to relate the time dynamics to the frequency domain via a Fourier transform, in this case, mapping T_1 times onto linewidths. This provides an additional check that our understanding and characterization of the system is correct. Naïvely, we might expect the FWHM linewidth, $\Delta\omega/2\pi$ to be equal to $1/2\pi T_1$, since the lifetime of the excited state must certainly bound the linewidth of the transition. However, in this case we have added additional dephasing and so the correct formula is

$$\Delta\omega/2\pi = \frac{2\Gamma_2}{2\pi} = \frac{1}{\pi T_2}$$

(which can be justified by taking the no pure dephasing limit and rearranging [Equation 3.5](#)).

When using this formula, we find good agreement with our measured linewidths. Taking isolated qubit 1 as an example, we measured a T_2 of (47 ± 1) ns and a FWHM linewidth of (6.9 ± 0.4) MHz. Plugging the T_2 into the above equation, we get $\Delta\omega/2\pi = (6.8 \pm 0.1)$ MHz. Similar results hold for the other qubits, validating our unorthodox time-resolved measurement methodology.

3.3 Interacting Many-Body System Characterization

One of the difficulties that arises when looking at systems of many interacting units is determining the source of different hybridized peaks measured in spectroscopy. In NMR, this problem is particularly important because knowledge about the states responsible for hybridized peaks leads to knowledge about the structure of the molecule. For strongly interacting quantum systems, similar problems can arise, especially when there is large disorder in qubit parameters due to fabrication or qubits are multiplexed on a single input/output line.

3.3.1 Coherent Spectroscopy

The solution to the assignment problem, borrowed from NMR, is known as *coherent spectroscopy* (COSY) [76]. COSY is a multi-pulse sequence, depicted below in Figure 3.8. In this sequence, there are two broadband $\pi/2$ pulses separated by a time delay, τ . After these pulses, the signal is recorded as a function of time, t . Recording the signal for many different values of τ and then Fourier transforming across both the t and τ dimensions produces the two-dimensional plot shown in Figure 3.9.

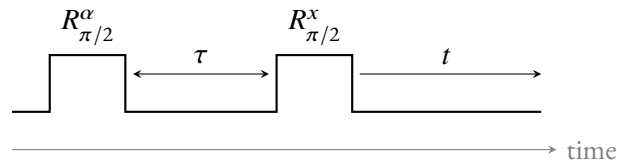


Figure 3.8: COSY pulse sequence. The phase of first pulse can be static or cycled to improve SNR (known as phase cycling, see section D.2)

In these plots, the peaks along the main diagonal corresponds to the signal measured during spectroscopy. Off-diagonal peaks correspond to states that are coupled. The locations of the peaks can be calculated by propagating the density matrix of the system through the above pulse sequence; for more information, see section D.1. Pulses are applied and measured relative to a fixed frequency, meaning that coherences and populations will appear to oscillate in the reference frame due to their detuning. For a peak to be on the diagonal, this means that the oscillation frequency during the τ and t times are the same, indicating a population that remained in this state. An off-diagonal peak means that the oscillation frequency changed between the two times, indicating population transfer or coherence between different states.

For our measurement, we excited the system with short, broadband pulses in the transmission line while applying flux noise to qubit 2 and recorded the electric field in the resonator. Thus, in Figure 3.9, we see the bright state and both dark states along the main diagonal (confirmed via the absolute frequencies of the peaks). At the same time, we see peaks in the upper-left quadrant linking the bright state to the two dark states, which we expect, since the flux noise couples the bright and dark states. Without flux noise, these cross-peaks are significantly reduced. Interestingly, we also see a faint cross-peak from

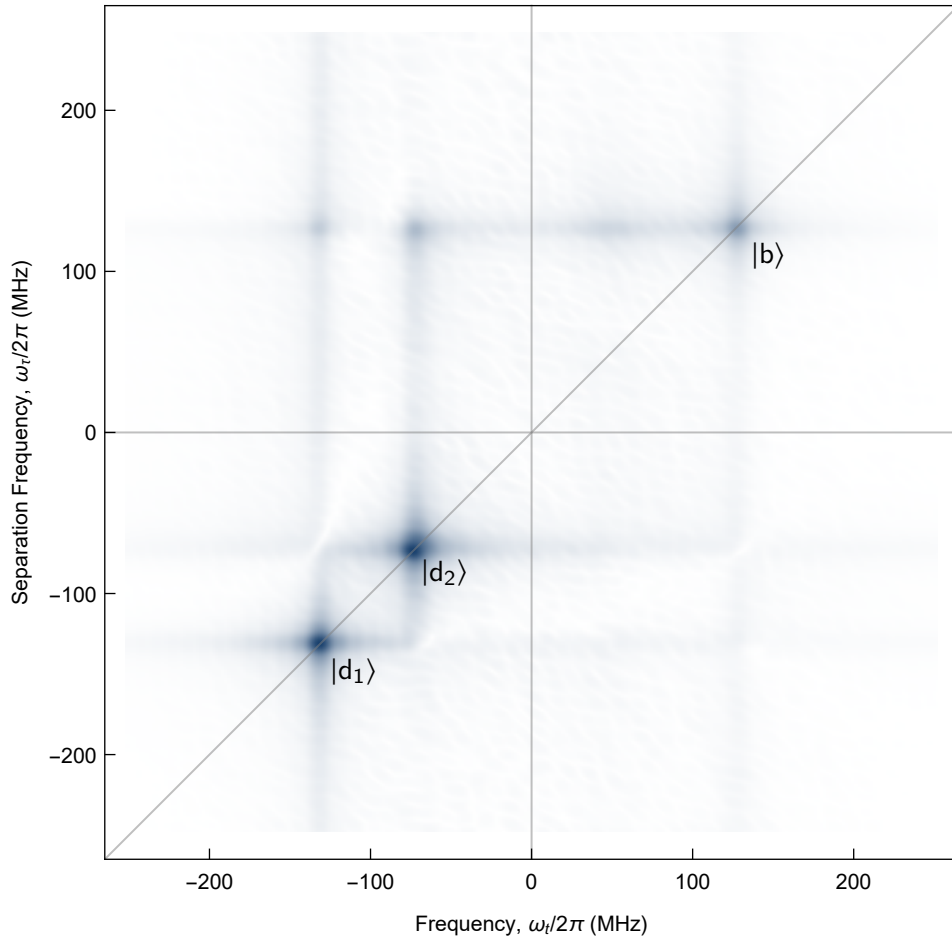


Figure 3.9: COSY measurement of the simulation configuration. Absolute value of two-dimensional Fourier transform components plotted versus frequency, $\omega_t/2\pi$ and separation frequency, $\omega_r/2\pi$. Qubits were excited using 3 ns square pulses from the transmission line at a frequency of 6.300 GHz and the signal was measured relative to the same frequency from the resonator. Bright state, $|b\rangle$, and dark states, $|d_1\rangle$ and $|d_2\rangle$, visible along the main diagonal. Cross-peaks indicating coupling from the bright state to the dark states visible in the upper-left quadrant. There is a broad feature at (70 MHz, 120 MHz) corresponding to coupling from the bright state to higher-lying states.

the bright state to a higher-lying state (which matches with the anharmonicity of our junctions). Notably absent are cross-peaks between the two dark states and cross-peaks from the bright state to the dark states in the lower-right quadrant. Instead, we see some “anti-peaks” or slightly negative features relative to the background. We are not certain of the reason for the absence of these features, but suspect that they are a result of our signal processing. For more information on the signal processing, see [section D.3](#).

An important part of producing clean COSY plots was something called *phase cycling*. When only considering a single pulse sequence, say $R_{\pi/2}^x$ followed by $R_{\pi/2}^x$, strong zero-frequency components arise which tend to mask the desired signal. However, by measuring x and y rotations by $\pi/2$ and $-\pi/2$ and then combining these in the appropriate way, the zero-frequency component disappears leaving only the COSY signals. For further discussion, see [section D.2](#).

Although in this case the coupling of the system was clear from spectroscopic measurements, this technique still allows us to verify that the coupling we expect is indeed present. Furthermore, this serves as a “proof-of-principle” for measuring complicated pulse sequences on our sample, paving the way for measurements using contemporary pulse sequences from the biophysics community. COSY itself is applicable whenever many qubits are simultaneously excited via direct capacitive coupling and could be useful in future analog quantum simulations or in larger systems with significant fabrication disorder.

These measurements also show the limitations of our sample. We would like to be able to perform the same measurements used by the biophysics community (such as two-dimensional electronic spectroscopy, a four-wave mixing experiment using three pulses applied to the sample, discussed further in [section C.7](#)). However, during experiments needing only two pulses, we already had difficulties with the system decaying as the pulses are being applied. In order to recover the figure above, we had to use the fastest pulses our AWG could generate (3 ns) and ignore the exact rotation angle. Adding an additional pulse with an additional time delay promises to make this more difficult.

In our case, the short T_1 times are the direct result of the strong, broadband coupling from the qubits to the input and output ports. Short decay times produce a “brighter” system, reducing averaging times for steady-state and time-resolved experiments. Unfortunately, in this case, we run into limitations of our electronics and our qubit anharmonicity and so future experiments may have to use a new sample that trades averaging time for qubit lifetimes.

3.4 Time-Resolved Photosynthetic Excitation Transport Measurements

With the system fully characterized, we can now move on to time-resolved measurements of photosynthetic energy transport in the standard simulation configuration. Here the basic idea of the measurement is to deterministically excite the bright state via a π pulse and then observe the signal in the resonator as a function of flux noise power and type. Due to the strong coupling of the dark states $|d_1\rangle$ and $|d_2\rangle$ (static coupling), we expect to

see oscillations of the power emitted into the resonator resulting from oscillations of the transferred population between the two states.

Since the transmon qubits function as two-level systems, the maximum number of photons that can be transferred from the bright state to the dark states and then subsequently emitted is one. This makes amplification, to improve the signal strength, and filtering, to reduce the number of noise photons that are collected, extremely important. We perform power measurements by signal processing of the electric field amplitude¹ since this is our natural measurement basis. For these reasons, we use a TWPA in the resonator line and also use a narrow (60 MHz) boxcar filter in the data processing to maximize our signal-to-noise ratio for these measurements. More discussion about the TWPA is present in [section C.3](#) and our digital filtering is discussed in [section C.1](#).

In the absence of flux noise, no signal was measured in the resonator, as is expected due to the energy difference of the bright state and the dark state. Adding flux noise dephases qubit 2, bridging this energy gap and resulting in increased power transmitted to the resonator, plotted in [Figure 3.10](#). For white noise, the transmitted power peaks and then declines and never reaches a clear peak for the Lorentzian noise. As predicted by ENAQT, the white noise initially boosts transport and then hinders it due to excessive dephasing at high powers (the *quantum Zeno effect*). Lorentzian noise results in higher emitted power than white noise due to its selective dephasing at relevant frequencies, also in line with our previous results [\[49\]](#). Although both noise types achieve similar total dephasing rates (*cf.* [Figure 3.7](#)), shaped noise that is optimized for the site energy differences results in dramatically greater transported power, demonstrating the efficiency boost that photosynthetic systems can extract from a carefully shaped phonon environment.

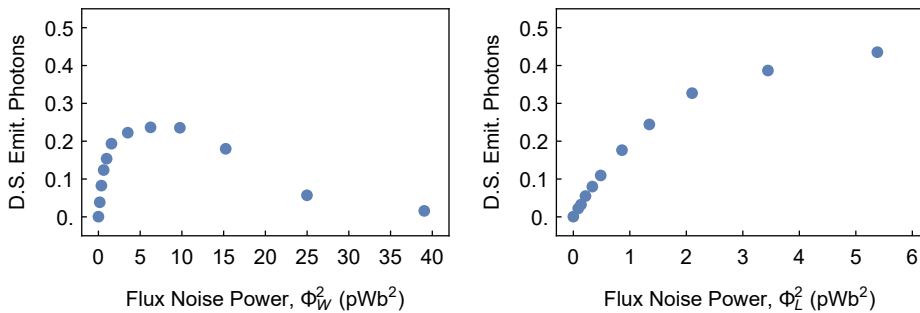


Figure 3.10: Approximate dark state emitted photons measured in the resonator as a function of flux noise type and power. *Left*: white noise which achieves maximum transmitted photon number at an intermediate flux noise power. *Right*: Lorentzian noise which achieves higher transmitted photon number than white noise and does not show a maximum within our attainable flux noise range. Note that the vertical axes of the figures are set to the same scale.

However, the interesting results appear when looking at the power emitted from the resonator as a function of time. Since timing is important, we first calibrated the delay

¹ $(I + iQ)^*(I + iQ)$ in terms of the measured complex electric field components I and Q .

difference between the transmission line and the resonator by applying a pulse to the transmission line and observing the time delay until it was detected in the resonator². Additionally, we measured the pulse duration via direct measurements (including up- and down-conversion but not the fridge). Then, during transport measurements, the signal from the transmission line and resonator were collected simultaneously, with the transmission line serving as a record of when the pulse reached the sample. Using these three pieces of information: the time the pulse started in the transmission line, the time delay between the transmission line and the resonator, and the duration of the pulse, we are able to plot the resonator power in a meaningful time-resolved manner, correcting for most of the timing differences, or *jitter*, that can occur.

The results of these measurements are presented below in Figure 3.11. At high flux noise intensities, both white and Lorentzian noise produce similar smooth, peaked transfer pulses. However, at very low white noise power, a few periods of oscillation are superimposed on the pulsed dynamics. For Lorentzian noise, the oscillations at low intensities are even more pronounced, almost completely replacing the pulse. In both figures, the gray lines are fits to a function of the following form:

$$f(t) = \begin{cases} 0 & t < t_0 - t_{\text{rise}} \\ \sin^2 \left(\frac{\pi}{2} \frac{t - (t_0 - t_{\text{rise}})}{t_{\text{rise}}} \right) & t_0 - t_{\text{rise}} \leq t < t_0 \\ A \exp [-(t - t_0)/T_1] & \\ + B \sin [2\pi(t - t_0)f - 2\pi\phi] \exp [-(t - t_0)/T_{\text{decay}}] & t \geq t_0 \end{cases} \quad (3.6)$$

where t_0 is the time of maximum power for each trace, t_{rise} is the time for the pulse to ramp from zero to the maximum, T_1 is the relaxation time, f is frequency, ϕ is a phase shift, and T_{decay} is the decay time of the oscillations. This phenomenologically models a constant rate of population transfer under the influence of noise (leading to \sin^2 oscillations, as with a Rabi drive) followed by an exponential decay with superimposed exponentially decaying sinusoid.

For the low power Lorentzian flux noise, we extract a frequency of (55.5 ± 0.8) MHz, matching the $|d_1\rangle$ - $|d_2\rangle$ frequency difference of 54 MHz well within the bounds of experimental uncertainty. A similar fit also holds for Lorentzian noise with a power of 0.022 pWb^2 . Oscillations with a similar period are visible to the eye in the higher-power Lorentzian noise traces, but these could not be robustly extracted during fitting. T_1 values in the fitting results correspond to the previously measured T_1 times within the fitting error, at approximately 15 ns to 20 ns. The decay times, T_{decay} , would be expected to be on the order of T_2 , but are observed to be significantly less, remaining below 20 ns, a result of our T_1 -limited sample.

This fitting model also allows us to extract other features from the rich dataset that time-resolution provides. As one example, we can look at the timing of the population transfer from bright state to the resonator via the dark states, called t_{rise} in the above model. As is perhaps visible by eye in Figure 3.11, the power maximum shifts towards

²Note that although there is no transfer from the bright state to the dark state in the absence of flux noise, there is a small amount of direct coupling from the transmission line to the resonator.

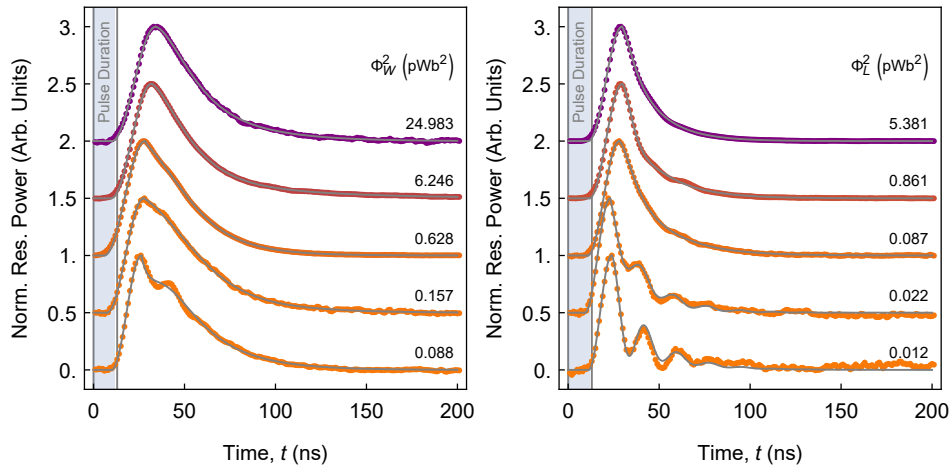


Figure 3.11: Time-resolved resonator power measurements. *Left*: white flux noise. *Right*: Lorentzian flux noise. Gray lines are nonlinear fits to Equation 3.6. Oscillation frequency of low-power Lorentzian noise traces matches $|d_1\rangle-|d_2\rangle$ frequency difference of 54 MHz.

later times with increasing flux noise power, which is made explicit when I plot t_{rise} versus flux noise power below in Figure 3.12. Here, both Lorentzian and white noise show similar general behavior: both feature a sharp jump in the rise time at low noise powers followed by a gradual increase with increasing power. Plotting the rise times instead on a linear-logarithmic plot, we see that the exponentially increasing flux power results in only (roughly) linearly increasing rise time. The kink in the Lorentzian noise rise time at noise powers around 0.1 pWb² is likely the result of transitioning to the noise amplifier. These rise times are not on the scale of the Purcell decay (8 MHz or 125 ns), but rather on the timescale of the resonator-qubit 3 state coupling (approximately 60 MHz or 16 ns). The increasing rise time at higher flux noise powers indicates that the coupling between the dark states and the resonator is reduced by dephasing, another area where the two noise types are distinguishable. White noise produces rise times which are always higher than the Lorentzian noise, indicating that while the white noise enables energy transport from the bright state to the dark state, it has significant side effects such as reduced coupling, which make it less efficient overall for photosynthetic energy transport. Again, specially tuned phononic modes provide significant advantages to photosynthetic organisms.

Lower rise times may also be important for the durability of the PPCs. One side product that competes with the reaction center as a sink for the exciton is singlet oxygen, a highly reactive species that can damage the organism [9]. Thus, it may be beneficial for the organism to tune for slightly lower transferred power as long as it occurs faster, leading to greater operational efficiency, since the organism either does not have to use repair machinery as often or perhaps lives longer.

Even in these measurements with classical noise that cannot replicate the full dynamics of a long-lived phonon mode, the advantages of shaped phonon modes for photosynthetic energy transport are clear. Lorentzian noise at an appropriate frequency results in more transferred photons and a faster start of photon transfer, than white noise at similar dephasing rates.

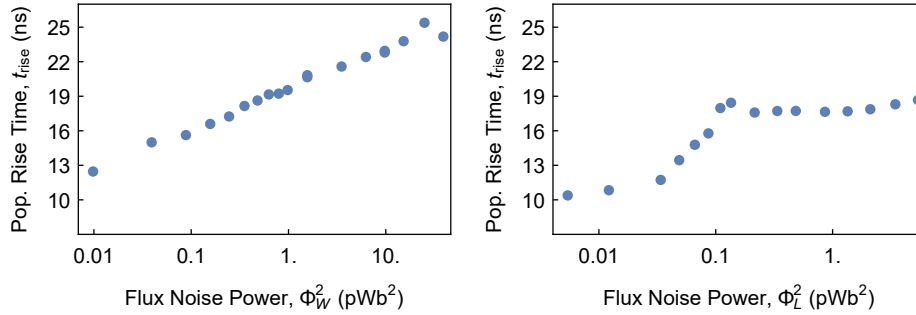


Figure 3.12: Population rise time versus flux noise power and type. *Left*: white flux noise. *Right*: Lorentzian flux noise.

3.4.1 Numerical Simulations

As a sanity check for the oscillating time traces that I showed above, I also performed numerical simulations of the white noise case. I used a time-dependent Hamiltonian to add the symmetric drive to the system for the first 12 ns and then allowed it to evolve, as occurs in the real measurements. Otherwise, the Hamiltonian was identical to Equation 2.3. Simulation Hamiltonian parameters were chosen to be comparable to the system parameters and are given in Table E.1. Loss into the transmission line and resonator were modeled using the Lindblad formalism (section B.1) with standard collapse operators. The flux noise was also treated in the Lindblad formalism, but using a $\hat{\sigma}^z$ collapse operator that shifts the energy levels rather than adding or removing quanta, although the dephasing rate had to be approximately twice as large as experimentally measured to observe similar behavior.

The results are plotted below in Figure 3.13. The numerical simulations broadly show the same behavior as the measurements on the sample, with small-amplitude oscillations at low flux noise powers (low dephasing rates) which then disappear at higher powers. While the simulations show a gradual reduction in the oscillation amplitude with increasing dephasing rate, the measurements show a faster decay in amplitude, largely due to the nonlinear change in dephasing rate with increasing noise power (Figure 3.7). The oscillations last longer for the numerical simulations, indicating that either some of the other dephasing channels do not match the rates of the real sample, or some dephasing channels are missing.

Additionally, the simulations recreate the result where the power increases only after the pulse finishes, although they do not show a change in the rise time despite the presence of oscillations. However, the results do help to rule out a conflicting source of the rise

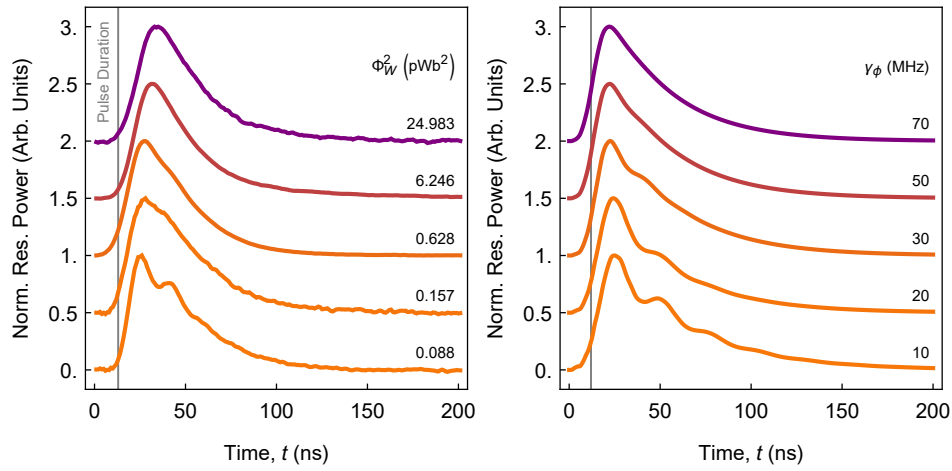


Figure 3.13: Comparison of white noise time-resolved resonator power measurements to numerical simulations. *Left*: measurement. *Right*: numerical simulation.

time variation. If the peak location was due to subtraction of oscillations with different amplitudes from same transfer peak, this could explain why low flux noise powers had faster rise times, since they also have large oscillations and would shift the power maximum earlier in time. This is not observed in the simulations, despite observing similar changes in the oscillation amplitude.

Unfortunately, numerical simulations of the Lorentzian noise are significantly more computationally difficult, so I cannot present comparisons here, but our collaborators are already looking into our results above to see if they can recreate them.

Chapter 4

Conclusions

Analog quantum simulations, especially of NAT or biological situations like photosynthetic energy transport, are still in their infancy. We are not yet capable of fabricating systems to follow Mostame's suggestion to simulate the full dynamics of FMO nor would we be ready to extract useful information from such a system if we were to suddenly have this capability. Rather, we are at the stage where we have to be content with smaller systems, learning the techniques to measure larger systems and building up a framework of results in order to clearly define which problems of these larger complexes to tackle.

Here, in this work, I have taken one small step along this journey. I have proven the applicability of our superconducting analog quantum simulator to studying the dynamics of noise assisted transport and photosynthetic energy transport. By exploiting the similarities of our sample to the physics of another well-developed field, NMR, we have found measurement techniques to characterize standard circuit QED parameters as well as novel techniques capable of determining couplings in spectrally congested systems as the full FMO complex certainly is. In analog simulations of photosynthetic energy transport, we have again demonstrated the principle result of ENAQT, with intermediate dephasing rates maximizing energy transport and biologically motivated shaped noise further enhancing transfer. In addition, we found clear evidence of the static coherence contained in our system and intriguing new results, only visible in the time domain, hinting at the effects of the static coherence.

We are currently measuring the second-order coherence, $g^{(2)}$, of the radiation emitted by qubit 3 in order to demonstrate that we have quantum transport in a fully quantum system. This is another crucial result before moving to larger systems or more accurate simulations since a quantum system can always behave as a classical one, but a classical system does not have access to quantum-mechanical effects. Furthermore, we plan to extend our two-pulse COSY measurements to three-pulse two-dimensional spectroscopy such that we can extract the same signals as observed in the biophysics community, removing communication barriers by presenting data in a familiar manner.

Now that we have a set of new measurement techniques and have extracted nearly all the information that we can from our sample, it is time to start developing our next sample. Longitudinal coupling to a truly quantum, low-frequency phononic mode would

dramatically improve our simulation fidelity and allow us to study new physics such as unidirectional energy transport due to the asymmetry between spontaneous emission and stimulated absorption from low-occupation resonators. Such a sample could also test whether low-frequency vibrational modes are the source of the long-lived quantum coherences in FMO or even be used to investigate novel analog quantum simulations, such as electron-phonon coupling during exciton transport in quantum dot films.

Thinking more generally about the future of analog quantum simulation with superconducting qubits, one persistent difficulty is extracting information with sufficient timing resolution. Mostame's original proposal predicts that the dynamics of photosynthetic energy transport will play out over 25 ns [43], and we observe dynamics over at most 100 ns. Compared to two-dimensional experiments using ultrafast lasers in the biophysics community, where 15 fs pulses are used to probe dynamics that last 5 ps with nearly arbitrary step sizes produced by physical delay stages, we are at a significant disadvantage. Readily available microwave equipment often has sample rates around 1 GS s^{-1} and with pulses at the limit of what our AWGs can produce, we cannot use shaping to improve timing resolution. While faster equipment is becoming available, this brings a significant disadvantage: greater noise. The only way to resolve faster dynamics is to increase the bandwidth of the entire signal processing chain which increases the noise photons included in the measurement, drastically increasing averaging times. Thus, with current techniques, we could extend our investigations to measuring the effect of NAT on efficiency in a sample with more sites and greater coupling, but might not be able to extract significant information about the dynamics that would be useful in solving the open questions in photosynthetic energy transport.

However, we have a larger number of advantages over biological measurements when it comes to answering the open questions from PET. While we do not have the automatic authenticity of the real samples, there are no limitations stopping us from implementing the same Hamiltonian. Once we have done this, we have a number of advantages. Our entire system is artificial, meaning that we can add or remove components to look for clear cause-and-effect relationships. We also tend to have tunable systems, meaning that we can go beyond investigation of FMO and other biological complexes with realistic parameters, but can investigate whether these parameter regimes are optimal or look at artificial systems to extract guidelines for organic photovoltaics.

Although we are just beginning to scratch the surface of analog quantum simulation, we have come a remarkable way from Feynman's prescription of [38]:

Let the computer be build of quantum mechanical elements which obey quantum mechanical laws.

to practical simulations of real physics and biophysics.

Acknowledgements

I deeply thank Anton for his patience, generosity, and guidance throughout this project. In addition, although I did not interact with him directly on this project, Arno left a wealth of knowledge in the form of the sample, his thesis, and his noise generation code.

Several other people were instrumental in completing the experiments in this thesis: Johannes, for his knowledge about the pulse generation libraries; Simon, for all of his help with SweepSpot; Kadir, for his help with the FPGA applications; Yves, for help with building our FPGA appliance; and Michele and Philipp, for their guidance while assembling our microwave setup.

Beyond performing measurements, Michele, Christian, Johannes, and Philipp offered useful discussion and advice.

Finally, I thank Professor Wallraff for allowing me to work in his group and use his equipment during this project.

Appendix A

Derivation of System Hamiltonian

A.1 Harmonic Oscillator

Before addressing electrical circuits, let me begin with the simple case of an ideal case of a mass oscillating on a spring, an example of a *simple harmonic oscillator* (see [Figure A.1](#)). In terms of the mass, m , and spring constant, k , the Hamiltonian can be written as:

$$H = \frac{1}{2m}p^2 + \frac{k}{2}x^2 \quad (\text{A.1})$$

where x (position) and p (momentum) are the *dynamical variables*. In the classical regime, these variables obey the Poisson bracket: $\{x, p\} = 1$. However, if we shrink the mass-on-spring system down and cool it down to extremely low temperatures [77], we find that we have to consider the system in a quantum mechanical sense. Thus, we replace x and p by their operator forms, \hat{x} and \hat{p} , which obey the commutation relation $[\hat{x}, \hat{p}] = i\hbar$. Letting $\omega = \sqrt{k/m}$, we arrive at

$$\hat{H} = \frac{1}{2m}\hat{p}^2 + \frac{m\omega}{2}\hat{x}^2$$

We can solve this Hamiltonian by working through complicated mathematical derivations, finding that the eigenstates are Hermite polynomials, or, we can take the so-called “ladder” operator approach. Define two new operators as follows:

$$\begin{aligned} \hat{a} &\equiv \sqrt{\frac{m\omega}{2\hbar}} \left(\hat{x} + \frac{i}{m\omega} \hat{p} \right) \\ \hat{a}^\dagger &\equiv \sqrt{\frac{m\omega}{2\hbar}} \left(\hat{x} - \frac{i}{m\omega} \hat{p} \right) \end{aligned}$$

With these operators, we find that the eigenstates of the harmonic oscillator are “number” states, $|n\rangle$, characterized by the number of quanta of energy, n , stored in the oscillator. In this context, \hat{a} and \hat{a}^\dagger correspond to *annihilation* and *creation* operators,

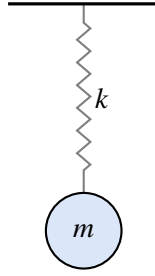


Figure A.1: Example of a harmonic oscillator. A mass, m , is suspended from a bar via an ideal spring with spring constant k .

decrementing or incrementing the energy quanta in the oscillator. The Hamiltonian can be re-written as:

$$\hat{H} = \hbar\omega \left(\hat{a}^\dagger \hat{a} + \frac{1}{2} \right)$$

such that

$$\hat{H} |n\rangle = \hbar\omega \left(n + \frac{1}{2} \right) |n\rangle.$$

Thus, we can see that an ideal harmonic oscillator has an infinite number of equally separated energy levels (eigenstates) characterized by n , the number of quanta of energy in the oscillator. For a more thorough discussion of the quantum harmonic oscillator, consult a text on quantum mechanics, such as [78].

A.2 LC Oscillator

Considering the circuit in [Figure A.2](#) classically, we can write the potential energy of the capacitor as $U_C = \frac{1}{2}CV^2$ and the potential energy of the inductor as $U_L = \frac{1}{2}LI^2$, leading to the Hamiltonian

$$H = \frac{1}{2}CV^2 + \frac{1}{2}LI^2$$

where V is the voltage across the capacitor and I is the current through the inductor. Using the definitions of capacitance ($Q = CV$) and inductance ($\Phi = LI$), where Q is electrical charge and Φ is magnetic flux, we can re-write the Hamiltonian as:

$$H = \frac{1}{2C}Q^2 + \frac{1}{2L}\Phi^2,$$

which is equivalent to the Hamiltonian for a macroscopic harmonic oscillator ([Equation A.1](#)).

Moving to the quantum case, where I will follow [54], we must be slightly more careful about which variables we consider dominant. In this case, I will assume linear capacitances with possibly nonlinear inductances (to allow for the addition of Josephson

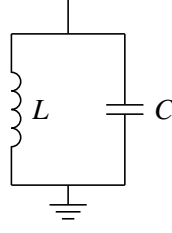


Figure A.2: Example of an inductor-capacitor (LC) resonator. An inductor, with inductance L , and a capacitor, with capacitance C , are connected in parallel.

junctions later), so I will treat the *node flux*, ϕ as the pseudo-position coordinate. The node flux can be calculated via

$$\phi(t) = \int^t V(\tau) d\tau$$

where integration begins at a point far in the past when the system was completely unperturbed. By analogy with the harmonic oscillator case, we have a potential energy of $U = \frac{1}{2}C\dot{\phi}^2$ (which can also be seen by using Faraday's law such that $V = \dot{\phi}$ in the LC oscillator Hamiltonian) and a kinetic energy of $T = \frac{1}{2L}\phi^2$. Thus the Lagrangian is

$$L = \frac{1}{2}C\dot{\phi}^2 - T = \frac{1}{2}C\dot{\phi}^2 - \frac{1}{2L}\phi^2$$

and the conjugate pseudo-momentum is

$$Q = \frac{\partial L}{\partial \dot{\phi}} = C\dot{\phi}.$$

Performing a Legendre transformation,

$$\begin{aligned} H &= Q\dot{\phi} - L \\ &= \frac{1}{2C}Q^2 + \frac{1}{2L}\phi^2. \end{aligned}$$

We can finally quantize the circuit, converting ϕ and Q to operators, $\hat{\phi}$ and \hat{Q} , which obey $[\hat{\phi}, \hat{Q}] = i\hbar$, yielding

$$\hat{H} = \frac{1}{2C}\hat{Q}^2 + \frac{1}{2L}\hat{\phi}^2. \quad (\text{A.2})$$

The method to solve this Hamiltonian is the same as the the harmonic oscillator case. Defining new creation and annihilation operators (\hat{a}^\dagger and \hat{a}) as

$$\begin{aligned} \hat{a} &= \frac{1}{\sqrt{2\hbar\omega}} \left(\frac{1}{\sqrt{L}}\hat{\phi} + i\frac{1}{\sqrt{C}}\hat{Q} \right) \\ \hat{a}^\dagger &= \frac{1}{\sqrt{2\hbar\omega}} \left(\frac{1}{\sqrt{L}}\hat{\phi} - i\frac{1}{\sqrt{C}}\hat{Q} \right) \end{aligned}$$

where the frequency of oscillation, ω , is $\omega = \frac{1}{\sqrt{LC}}$ and the impedance of the circuit, Z , is $Z = \sqrt{\frac{L}{C}}$, we re-write the Hamiltonian as

$$\hat{H} = \hbar\omega \left(\hat{a}^\dagger \hat{a} + \frac{1}{2} \right),$$

confirming that the system is isomorphic to the harmonic oscillator. Therefore the quantum LC circuit also has an infinite spectrum of levels that are equally spaced.

While harmonic systems display interesting physics related to number (*Fock*) states and *coherent* states, they are not ideal for quantum simulations or quantum computers, since they have infinite-dimensional Hilbert spaces. In order to restrict the Hilbert space (*i.e.* to create a two level system), we have to make the system aharmonic such that the energy levels are unevenly spaced. To do this, we will add a Josephson junction, the subject of the next section.

A.3 Josephson Junction

The basic principle behind a *Josephson junction* is that coherent tunneling of *Cooper pairs* through a “small” barrier can lead to dissipationless current flow (a *supercurrent*) [52]. This effect is formalized by the *Josephson equations* which describe the voltage and current across the superconductor-barrier-superconductor junction:

$$V(t) = \frac{\Phi_0}{2\pi} \frac{\partial \varphi(t)}{\partial t} \quad (\text{A.3})$$

$$I(t) = I_c \sin(\varphi(t)) \quad (\text{A.4})$$

where Φ_0 is the magnetic flux quantum, $\Phi_0 \equiv \frac{h}{2e}$, I_c is the *critical current* of the device, determined by material and geometric properties of the junction, such as overlap area and barrier thickness, and φ is the *Josephson phase*, or the phase difference between the superconducting wavefunctions across the barrier [79, p. 11]. A diagram of a S-B-S junction is given in Figure A.3. In the case that I will discuss, this barrier is a thin layer of an insulator, so the junctions are of the superconductor-insulator-superconductor (S-I-S) type.



Figure A.3: Basic diagram of a Josephson junction. Two superconducting regions (S) are separated by a thin barrier region (B). For our qubits, these barriers are a thin layer of insulator.

In order to make apparent that the Josephson junction acts as a nonlinear inductor, let us compute the time-derivative of the current relation (Equation A.4):

$$\frac{\partial I}{\partial t} = I_c \cos(\varphi) \frac{\partial \varphi}{\partial t}$$

which can be re-arranged using the Josephson voltage relation (Equation A.3) to give:

$$V(t) = \frac{\Phi_0}{2\pi} \frac{1}{I_c \cos(\varphi)} \frac{\partial I}{\partial t}.$$

Comparing this to the definition of inductance ($V = L \frac{\partial I}{\partial t}$), we find that the Josephson inductance, L_J is

$$L_J = \frac{\Phi_0}{2\pi} \frac{1}{I_c \cos(\varphi)} \quad (\text{A.5})$$

Now, we need to compute the energy associated with the junction. This can be computed by integrating the number of Cooper pairs that have tunneled across the junction along with their voltage from a time long in the past when the junction was completely unperturbed up to a specified time t as follows:

$$\begin{aligned} E &= \int^t V(\tau) I(\tau) d\tau \\ &= \frac{\Phi_0 I_c}{2\pi} \int^t \sin(\varphi(\tau)) \frac{\partial \varphi}{\partial \tau} d\tau \\ &= E_J (1 - \cos(\varphi(t))) \end{aligned}$$

assuming that the Josephson phase at this distant point in the past is zero, and where the *Josephson energy*, E_J , is defined as $E_J = \frac{\Phi_0 I_c}{2\pi}$. Ignoring the constant offset, this makes the Hamiltonian of a Josephson junction

$$H = -E_J \cos(\varphi) \quad (\text{A.6})$$

which Girvin also derives using a tight-binding approximation [54]. As with the LC oscillator, the appropriate dynamical variables for use in describing the circuit of a Josephson junction depend on the composition of the circuit. Instead of node flux or charge, here we have Josephson phase, φ , and the number of Cooper pairs, n (The two sets can be related via $q = -2en$ and $\varphi = 2\pi \frac{\Phi}{\Phi_0}$). In the following sections, I will discuss the different types of qubits that can be formed where charge is the prominent variable, since these are the predominant type of qubits used in our lab¹.

A.3.1 Cooper Pair Box

The simplest type of charge qubit is known as the *Cooper-pair box* (CPB), first measured by Bouchiat *et al.* in 1998 [80]. In this qubit design, depicted in Figure A.4, a Josephson junction and capacitor are placed in parallel to form a superconducting “island” which is isolated from a voltage source via a “gate” capacitor. Because this island is isolated from the voltage source, the number of Cooper pairs on the island is a well-defined discrete number, meaning that the phase operator must be periodic (*i.e.* only $\cos(\varphi)$ is

¹There are also other types of qubits, called *phase qubits* where the phase (and hence magnetic flux) is the important variable. For more information, consult [54]

an operator, not φ). In addition, we will have to worry about the Coulombic repulsion between different Cooper pairs, leading to the Coulombic charging energy

$$\hat{U} = 4E_C(\hat{n} - n_g)^2$$

where E_C is the Coulombic *charging energy*, $E_C \equiv \frac{e^2}{2C_\Sigma}$, C_Σ is the total capacitance, $C_\Sigma = C_J + C_g$, and n_g is the *gate charge* due to the external voltage source, $n_g \equiv -\frac{C_g V}{2e}$ [54].

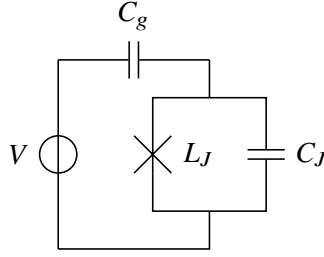


Figure A.4: Basic diagram of a Cooper-pair box. In this system, a Josephson junction (depicted as an angled cross) with impedance L_J is shunted with a capacitor C_J , forming an “island” that is galvanically isolated from a voltage source V by a “gate” capacitor C_g .

Adding the Josephson junction term we previously derived (Equation A.6) leads to a total Hamiltonian

$$\hat{H} = 4E_C(\hat{n} - n_g)^2 - E_J \cos(\hat{\varphi}) \quad (\text{A.7})$$

where actually the entire $\cos(\hat{\varphi})$ is taken as the operator due to the compactness of φ in this case. An exact solution can be found in the phase basis by following the methods of Ref. [81] and using *Mathieu functions*.

Alternatively, if we assume that the variations of the phase are small, we can expand the cosine potential (dropping constant terms) and arrive at the following approximation:

$$\hat{H} \approx 4E_C \hat{n}^2 - \frac{E_J}{2} \hat{\varphi}^2$$

where I have also assumed that the gate voltage is set to zero. Comparing with the LC oscillator above (Equation A.2), we find that we have

$$C = \frac{e^2}{2E_C}$$

$$L = \frac{\Phi_0^2}{4\pi^2 E_J}$$

giving a transition frequency (known as the *Josephson plasma frequency*) of


$$\hbar\omega = \sqrt{8E_C E_J}.$$

For the small phase approximation to hold, we should check that the zero point fluctuations of the junction are small. According to Girvin, $\Phi_{\text{ZPF}} = \sqrt{\frac{\hbar L \omega}{2}}$, which, after plugging in the equations above and rearranging, gives

$$2\pi \frac{\Phi_{\text{ZPF}}}{\Phi_0} = \left(2 \frac{E_C}{E_J}\right)^{1/4},$$

so the zero-point fluctuations are only small when when $E_J \gg E_C$.

A.3.2 Transmon

One extension of the Cooper pair box, first reported by Koch *et al.* in 2007 is known as the *transmon* [81]. The transmon qubit adds a large shunt capacitance in parallel with the Josephson junction (often formed by the overlapping pads of the junction itself) which reduces the charging energy and hence E_C/E_J , reducing the susceptibility of the junction to charge noise (“charge dispersion”). The relative anharmonicity of the junction, defined as the ratio of the e - f transition energy to the g - e transition energy, scales as $1/\sqrt{E_J/E_C}$ while the charge dispersion scales as $\exp(E_J/E_C)$ [81], meaning that the dispersion can be suppressed without eliminating the anharmonicity that allows the qubit to be used as a two-level system. The transmon is often written as a “boxed” Josephson junction  to signify the large shunt capacitor included with the junction.

A.3.3 Superconducting Quantum Interference Devices

In a Superconducting Quantum Interference Device (SQUID), two Josephson junctions are placed in parallel, leading to a modulation of the resonant frequency based on the external flux penetrating the loop, as I will derive below. A basic diagram of a SQUID is presented in [Figure A.5](#).

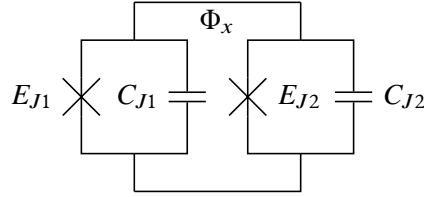


Figure A.5: Basic diagram of a SQUID

Focusing just on the portion of the Hamiltonian due to the Josephson junctions, and thinking in terms of the flux through each junction, we have:

$$H_J = E_{J1} \cos \left[\frac{2\pi}{\Phi_0} \left(\Phi_1 + \frac{1}{2} \Phi_x \right) \right] + E_{J2} \cos \left[\frac{2\pi}{\Phi_0} \left(\Phi_2 + \frac{1}{2} \Phi_x \right) \right] +$$

Assuming that the junctions are mostly symmetric, so $E_{J2} = E_{J1} + \epsilon$, we can re-write this as

$$H_J = E_{J1} \left(\cos \left[\frac{2\pi}{\Phi_0} \left(\Phi_1 + \frac{1}{2} \Phi_x \right) \right] + \cos \left[\frac{2\pi}{\Phi_0} \left(\Phi_2 + \frac{1}{2} \Phi_x \right) \right] \right) + \epsilon \cos \left[\frac{2\pi}{\Phi_0} \left(\Phi_2 + \frac{1}{2} \Phi_x \right) \right]$$

Since we still have a well-defined number of Cooper pairs on each side of the Josephson junctions, the Josephson phase of the junctions is compact, so the flux must be quantized, *i.e.* $\Phi_2 = -\Phi_1 + 2\pi n$ for $n \in \mathbb{N}$. Plugging this in and using standard trigonometric identities results in the final Hamiltonian:

$$H_J = (2 + \epsilon) \cos\left(\frac{\pi}{\Phi_0} \Phi_x\right) \cos\left(\frac{2\pi}{\Phi_0} \Phi_1\right) + \epsilon \sin\left(\frac{\pi}{\Phi_0} \Phi_x\right) \sin\left(\frac{2\pi}{\Phi_0} \Phi_1\right).$$

Defining $E_J(\Phi_x) \equiv 2 \cos\left(\frac{\pi}{\Phi_0} \Phi_x\right)$, and setting the junction asymmetry ϵ to zero, we get the SQUID Josephson junction Hamiltonian

$$H_J = E_J(\Phi_x) \cos(\varphi)$$

where it is now clear why I stated earlier that a SQUID loop functions as a frequency-tunable Josephson junction.

A.4 System Hamiltonian

A.4.1 Qubit-Qubit Coupling

The qubits of our system are capacitively coupled. To compute the Hamiltonian terms resulting from this coupling, let us consider the circuit shown in [Figure A.6](#).

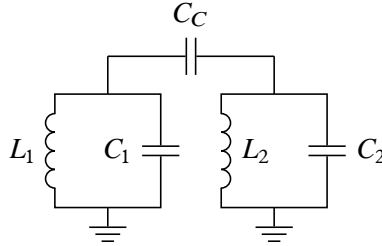


Figure A.6: Coupled LC oscillators.

Focusing on the capacitive portion of the Lagrangian,

$$L_C = \frac{C_1}{2} \dot{\phi}_1^2 + \frac{C_2}{2} \dot{\phi}_2^2 + \frac{C_C}{2} (\dot{\phi}_1 - \dot{\phi}_2)^2,$$

we can compute the conjugate variables

$$q_1 = \frac{\partial L_C}{\partial \dot{\phi}_1} = (C_1 + C_C) \dot{\phi}_1 - C_C \dot{\phi}_2$$

$$q_2 = \frac{\partial L_C}{\partial \dot{\phi}_2} = -C_C \dot{\phi}_1 + (C_2 + C_C) \dot{\phi}_2.$$

Treating this as a matrix and inverting, we get

$$\begin{aligned}\phi_1 &= \frac{C_2 + C_C}{C_1 C_2 + C_C (C_1 + C_2)} q_1 + \frac{C_C}{C_1 C_2 + C_C (C_1 + C_2)} q_2 \\ \phi_2 &= \frac{C_C}{C_1 C_2 + C_C (C_1 + C_2)} q_1 + \frac{C_1 + C_C}{C_1 C_2 + C_C (C_1 + C_2)} q_2.\end{aligned}$$

Performing a Legendre transformation to get the Hamiltonian as usual, *i.e.*

$$H_C = q_1 \phi_1 + q_2 \phi_2 - L_C$$

and rearranging, we get

$$H_C = \frac{1}{2\tilde{C}_1} q_1^2 + \frac{1}{\tilde{C}_C} q_1 q_2 + \frac{1}{2\tilde{C}_2} q_2^2$$

in terms of renormalized capacitances.

Using the usual mapping of charges to annihilation and creation operators,

$$\begin{aligned}q_1 &\rightarrow i\sqrt{\frac{\hbar\omega_1\tilde{C}_1}{2}} (\hat{a}_1^\dagger - \hat{a}_1) \\ q_2 &\rightarrow i\sqrt{\frac{\hbar\omega_2\tilde{C}_2}{2}} (\hat{a}_2^\dagger - \hat{a}_2)\end{aligned}$$

we can rewrite the cross-term as

$$\frac{1}{\tilde{C}_C} q_1 q_2 \rightarrow \frac{\hbar}{2} \sqrt{\omega_1 \omega_2 \tilde{C}_1 \tilde{C}_2} (\hat{a}_1 - \hat{a}_1^\dagger) (\hat{a}_2^\dagger - \hat{a}_2),$$

which, after making the rotating wave approximation, where we drop highly oscillatory terms with respect to a frame rotating at the qubit frequency (or drop non energy-conserving terms), leads to

$$\frac{\hbar}{2} \sqrt{\omega_1 \omega_2 \tilde{C}_1 \tilde{C}_2} (\hat{a}_1 \hat{a}_2^\dagger + \hat{a}_1^\dagger \hat{a}_2) \propto \sqrt{\omega_1 \omega_2} (\sigma_1^- \sigma_2^+ + \sigma_1^+ \sigma_2^-)$$

which is proportional to the usual $\sigma_a^+ \sigma_b^- + \sigma_b^+ \sigma_a^-$ terms for capacitive qubit coupling.

A.4.2 Qubit-Transmission Line Coupling

If we move beyond lumped-elements, to the regime where elements are no longer negligible in size compared to the microwave radiation, we have to begin considering spatial dimensions when deriving our Hamiltonian. This is particularly necessary for our coplanar waveguide transmission line and $\lambda/4$ resonator. Coplanar waveguides are passive elements which are narrow (approximately $25 \mu\text{m}$ in width) but have a length that is comparable to the the wavelength of the microwaves, meaning that we can approximate them as one-dimensional. They can be modeled by treating them as a series of infinitesimal inductors in parallel with capacitors to ground [82] or as classical transmission lines

[83]. In either case, they are characterized by their capacitance, c , and their inductance, l , per unit length. Following Girvin [54], I will start by defining the position-dependent branch flux:

$$\Phi(x, t) = \int_{-\infty}^t V(x, \tau) d\tau$$

and noting that the constitutive equation for the current becomes

$$I(x, t) = -\frac{1}{l} \partial_x \Phi(x, t).$$

The Lagrangian now involves an integral over the spatial coordinate

$$L = \int^{\ell} \frac{c}{2} (\partial_t \Phi(x, t))^2 - \frac{1}{2l} (\partial_x \Phi(x, t))^2 dx = \int^{\ell} \mathcal{L} dx$$

where I assume that the element has length ℓ . Calculating the conjugate charge as usual (looking only at the terms inside the integral), we find

$$q(x, t) = c \partial_t \Phi(x, t)$$

resulting in the following Hamiltonian

$$H = \int^{\ell} \frac{1}{2c} q(x, t)^2 + \frac{1}{2l} (\partial_x \Phi(x, t))^2 dx.$$

Returning to the Lagrangian, if we compute the Euler-Lagrange equation,

$$\partial_t \frac{\partial \mathcal{L}}{\partial (\partial_t \Phi)} + \partial_x \frac{\partial \mathcal{L}}{\partial (\partial_x \Phi)} - \frac{\partial \mathcal{L}}{\partial \Phi} = 0$$

we get

$$\partial_{tt} \Phi - \frac{1}{lc} \partial_{xx} \Phi = 0$$

a wave equation with propagation velocity, $v = \frac{1}{\sqrt{lc}}$. For a finite coplanar waveguide, *e.g.* a resonator, with specified boundary conditions, we can make an ansatz of oscillating solutions, allowing us to quantize the circuit and revealing that it is equivalent to a sum of harmonic oscillator modes [82, 54]. In the limit of large mode separation, we can treat a resonator as a single-mode oscillator.

For the semi-infinite transmission line, the case is slightly more complicated. Following [84], we must consider the input-output theory [85] of the transmission line, working in terms of left and right propagating fields and including the physical separation of elements. For more details on this, including a calculation of the expected power spectrum visible in the input/output lines, consult [55].

Appendix B

Open Quantum Systems

For open quantum systems, systems that are not isolated and have degrees of freedom which are uncontrolled, we cannot stick to the picture of unitary evolution used for closed systems, since this allows no excitation or loss of energy.

B.1 Lindblad Formalism

Instead of the Schrödinger equation acting on wavefunctions

$$\hat{H} |\Psi\rangle = E |\Psi\rangle,$$

for open systems it is easiest to work in an equivalent picture, utilizing what is known as the *density matrix*. The density matrix is defined as

$$\rho = |\Psi\rangle \langle \Psi|$$

which can be decomposed in a basis (say $\{|\psi_j\rangle\}$) as

$$\rho = \sum_j p_j |\psi_j\rangle \langle \psi_j|$$

where p_j are classical probabilities of being in state $|\psi_j\rangle$.

In the density matrix formalism, the time evolution of the system is given by the *Liouville—von Neumann equation*,

$$\frac{\partial \rho}{\partial t} = -\frac{i}{\hbar} [H, \rho] \tag{B.1}$$

rather than the Schrödinger equation. However, this still has only unitary dynamics. To account for incoherent excitation and decay events, we must extend this to the *Lindblad equation*,

$$\frac{\partial \rho}{\partial t} = -\frac{i}{\hbar} [H, \rho] + \sum_i \gamma_i \left(L_i \rho L_i^\dagger - \frac{1}{2} L_i^\dagger L_i \rho - \frac{1}{2} \rho L_i^\dagger L_i \right), \tag{B.2}$$

where the L_i are known as *Lindblad operators*, describing the non-unitary events, and the γ_i are the coefficients describing the rates of these events. Equation B.2 can be explicitly derived in a perturbative manner by assuming weak system–bath coupling and by assuming that the bath correlations rapidly disappear (the so-called *no-memory* or *Markovian* bath approximation) [54].

A particular example of such an operator in the case of our sample comes from the resonator coupled to the transmission line. The presence of the transmission line modifies the local electromagnetic environment, allowing the resonator to emit photons at a rate usually referred to as κ . However, due to thermal photons present in the transmission line, there is also the possibility of thermally exciting photons in the resonator, with a quantum asymmetry provided by the vacuum photons always present in the transmission line. Defining the Lindblad *superoperator* of an operator \hat{O} as

$$\mathcal{D}[\hat{O}] \equiv \left(\hat{O}\rho\hat{O}^\dagger - \frac{1}{2} \{ \hat{O}^\dagger\hat{O}, \rho \} \right)$$

we get two terms in our Lindblad equation:

$$\begin{aligned} &\kappa(n_{\text{th}} + 1) \mathcal{D}[\hat{a}_r] \\ &\kappa n_{\text{th}} \mathcal{D}[\hat{a}_r^\dagger] \end{aligned}$$

where \hat{a}_r is the annihilation operator for photons in the resonator, κ is the coupling between the resonator and the transmission line (resonator loss rate), and n_{th} is the average thermal photon number of the transmission line. The upper term describes stimulated emission while the lower term describes stimulated excitation. This can be extended to include many loss or excitation channels.

Appendix C

Methods

C.1 Bandwidth of Pulses and Boxcar Filter

Since our pulses and our digital filtering are both square, I will discuss the spectrum of a square pulse / boxcar filter here. I have drawn the scheme of a boxcar filter or square pulse as a function of time in [Figure C.1](#). Calling this function $g(t)$, we can compute the frequency spectrum, $\hat{g}(\omega)$ via a Fourier transformation:

$$\begin{aligned}\hat{g}(\omega) &= \int_{-\infty}^{\infty} g(t)e^{-i\omega t} dt \\ &= \int_0^a g(t)e^{-i\omega t} dt \\ &= -\frac{1}{i\omega} (e^{-i\omega a} - 1)\end{aligned}\tag{C.1}$$

the absolute value of which is plotted in [Figure C.2](#). Importantly, the nulls of the frequency response occur when $\omega = n2\pi/a$ for $n \in \mathbb{Z}$. The bandwidth of a few relevant boxcar filter settings are presented in [Table C.1](#).

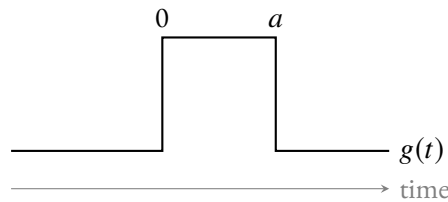


Figure C.1: Time scheme of boxcar filter or square pulse

C.2 Noise Voltage to Flux Power Conversion

The experiments presented above were run by setting particular peak-to-peak voltages (V_{pp}) on the noise AWG. To convert these to flux powers, we first convert from voltage

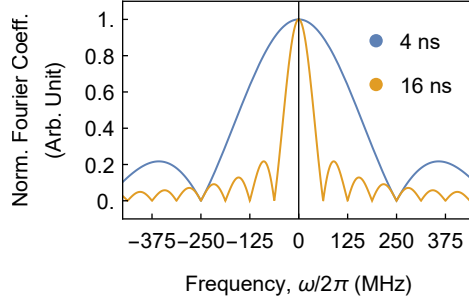


Figure C.2: Spectrum of boxcar filter/square pulses of 4 and 16 ns duration.

Table C.1: Boxcar filter length and resulting bandwidth

Boxcar Length	Length (ns)	Bandwidth (MHz)
2 = 2 ²	4	500
3 = 2 ³	8	250
4 = 2 ⁴	16	125
5 = 2 ⁵	32	62.5
6 = 2 ⁶	64	31.25
7 = 2 ⁷	128	15.63

spectral density, S_U ($V^2 \text{ Hz}^{-1}$), to flux spectral density S_ϕ ($\text{Wb}^2 \text{ Hz}^{-1}$) via

$$S_\phi = \left(\frac{V_{\text{PP}}}{V_{\text{max}}} \right)^2 S_U \left(\frac{M}{\Phi_0} \right)^2$$

where V_{max} is the maximum V_{PP} that can be set on the AWG, Φ_0 is the flux quantum, and M is a parameter extracted from the coil sweep fits that characterizes the flux per volt applied to the flux line. For our sample, M was -0.28 Wb V^{-1} , S_U was $0.009 \text{ V}^2 \text{ Hz}^{-1}$ for white noise and $0.026 \text{ V}^2 \text{ Hz}^{-1}$ for Lorentzian noise. For the Tektronix AWG520, V_{max} is 2.00 V.

Then, in order to convert from flux power spectral density to flux power, we integrate the spectra of the two noise types

$$\Phi_L^2 = \int_0^{\nu_{\text{max}}} \frac{S_{\phi,L}}{1 + \left(\frac{\nu - \nu_{0,L}}{b_L} \right)^2} d\nu$$

and

$$\Phi_W^2 = \int_0^{\nu_{\text{max}}} \frac{S_{\phi,W}}{1 + \exp\left(\frac{\nu - \nu_{0,W}}{b_W}\right)} d\nu$$

where $\nu_{\max} = 500$ MHz, $\nu_{0,L} = 246$ MHz, $\nu_{0,W} = 325$ MHz, $b_L = 5$ MHz, and $b_W = 11.378$ MHz.

C.3 TWPA

The TWPA produces a frequency-dependent gain profile which must be carefully optimized, by tweaking the drive power and drive frequency, in order to maximize gain while minimizing distortion due to unequal amplification. In our case, optimal parameters were a drive power of 15.5 dBm at a frequency of 6.849 000 7 GHz, with the 700 Hz offset to avoid sampling the probe tone during sweeps. This results in a gain curve plotted below in [Figure C.3](#). Note the relatively flat region of gain around 6.2 GHz where the dark states emit.

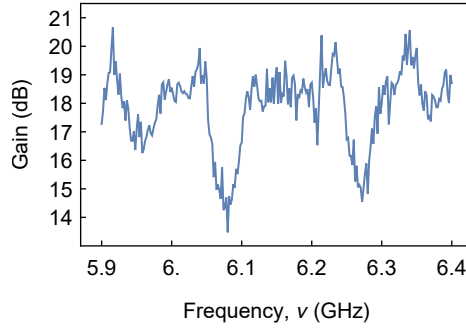


Figure C.3: TWPA gain as a function of frequency at a drive power of 15.5 dBm and a drive frequency of 6.849 000 7 GHz.

C.4 Rabi Measurements

We have two different methods of performing Rabi measurements, which differ only in the processing that is applied to the resulting data set: time-resolved, which looks at the signal as a function of time and pulse amplitude; and frequency-resolved, which separates out contributions from different states, making the Rabi characterization, particularly of short pulses that excite several transitions, more precise.

C.4.1 Time-Resolved

The time-resolved Rabi measurement revolves around recording time traces of the qubit response to pulses of changing length or amplitude. In our case, we chose to vary the amplitude in order to have identical bandwidth for pulses of different rotation angles. The pulse scheme is depicted below in [Figure C.4](#) and the scheme is depicted in terms of the Bloch sphere in [Figure C.5](#). The variable amplitude pulse drives Rabi oscillations between the ground and the excited state, rotating the qubit state about the x axis by a variable angle, θ . In this technique, we measure electric field amplitude $\langle I_1 + iQ_1 \rangle$ in

terms of electric field quadratures), which corresponds to the x - y plane of the Bloch sphere. This means that the recorded signal is maximum for $\theta = \pi/2$, has a null at π , and a minimum at $\theta = 3\pi/2$.

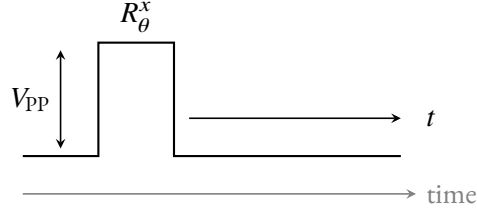


Figure C.4: Rabi measurement pulse scheme. Pulse amplitude is varied across different measurement runs; signal is recorded as a function of time.

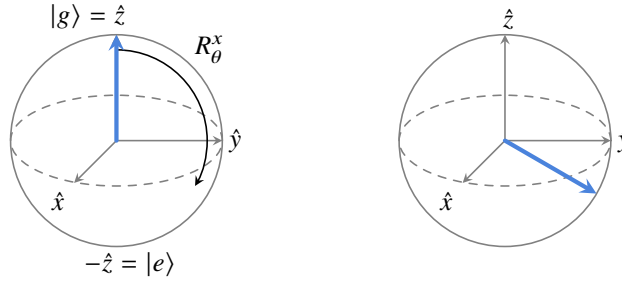


Figure C.5: Depiction of the Rabi measurement pulse scheme on the Bloch sphere. The variable-amplitude pulse serves to rotate the qubit state about the x axis by a variable angle. Since we measure electric field amplitude, we essentially measure the projection of the qubit state onto the $x - y$ plane, meaning that we have maximal signal when $\theta = (2n + 1)\pi/2$, and minimal signal for $\theta = 2n\pi$.

An example of the data we measured as a function of time is plotted in [Figure C.6](#). The typical Rabi measurement plot can be extracted by integrating the data across time after the pulse and then plotting it as a function of pulse amplitude.

C.4.2 Frequency-Resolved

Our frequency-resolved Rabi technique uses the same pulse sequence as the time-resolved above, but adds a Fourier transform across time which separates out different frequency components. Using the data shown above in [Figure C.6](#), this results in [Figure C.7](#). Selecting a region around one of the states and integrating across frequency results in plots such as [Figure 3.2](#). This method is particularly useful with short pulses that excite several parts of the system, as these components can be individually selected, see [Figure C.8](#).

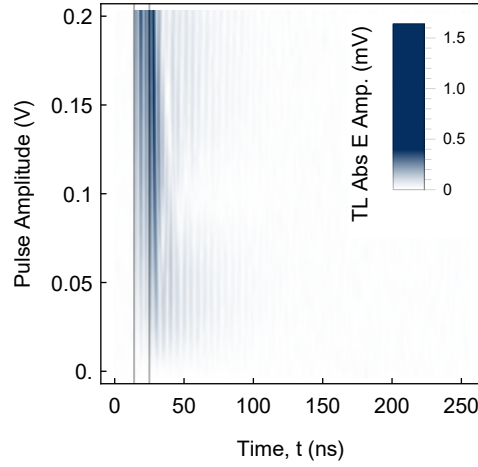


Figure C.6: Example of time-resolved Rabi measurement. Absolute amplitude of electric field response in the transmission line plotted as color versus time and pulse amplitude. The driving pulse occurs during the region bounded by translucent gray lines. Fast oscillations in signal are due to detuning between qubit resonance frequency and frequency of down-conversion LO.

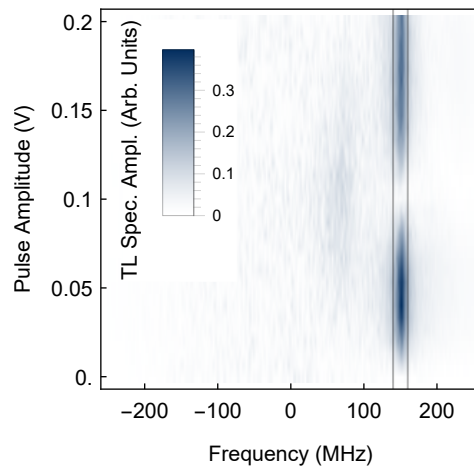


Figure C.7: Example of frequency-resolved Rabi measurement. Absolute amplitude of spectral component in the transmission line plotted as color versus frequency and pulse amplitude. Instead of fast oscillations, we now see that the qubit was detuned relative to the downconversion center frequency. The gray lines indicate the region that is integrated to produce plots like [Figure 3.2](#).

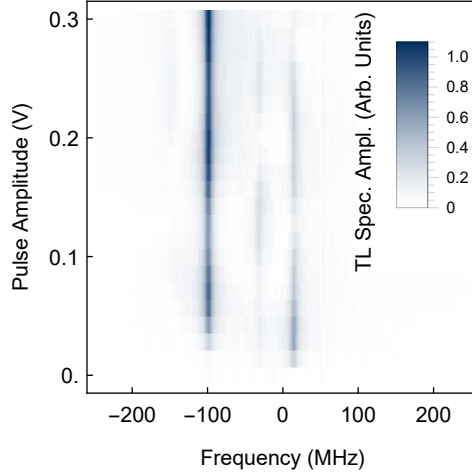


Figure C.8: Example of multi-state frequency-resolved Rabi measurement. Absolute amplitude of spectral component in the transmission line plotted as color versus frequency and pulse amplitude. These components would be impossible to separate in a time-resolved measurement.

C.5 T_1 Measurements

For T_1 measurements, we can either use a method borrowed from NMR and tailored to our measurement basis (based on our connectivity) or the “standard” cQED method.

C.5.1 Inversion Recovery

The *inversion recovery* technique involves a two pulse sequence shown in [Figure C.9](#). The signal is measured in terms of electric field amplitude after the second pulse, but is collected for different values of the interpulse delay, τ , rather than different pulse amplitudes as in the Rabi measurement above. I have depicted the results of the pulse scheme for zero τ on the Bloch sphere in [Figure C.10](#). For no time delay, the qubit state ends up along $-y$. Conversely, at long time delays, the qubit decays from the excited state back to the ground state, so the second $\pi/2$ pulse has the effect of rotating the qubit to y . Therefore, as τ is increased, the signal starts off inverted and gradually recovers back to a positive value.

An example inversion recovery T_1 measurement is plotted in [Figure C.11](#). Again, as with the Rabi measurements, we can look at either time-resolved (t) or frequency-resolved (ω_t) plots. In order to extract T_1 values, we either select a signal trace at a specific t (and hence as a function of τ) or integrate around a specific frequency range, as shown in [Figure C.12](#). Note that the inversion of signal is clearly visible in the time trace, but that the Fourier trace improves the signal-to-noise ratio of the data. Fitting an exponential rise of the form $A[1 - \exp(-\tau/T_1)]$ gives the T_1 time. Both methods produce similar T_1 times.

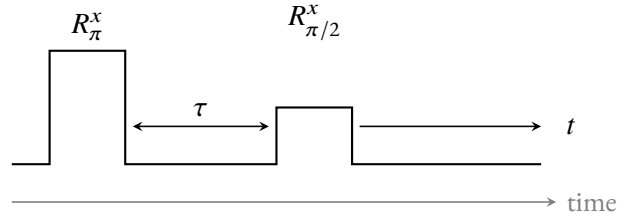


Figure C.9: Inversion recovery pulse scheme.

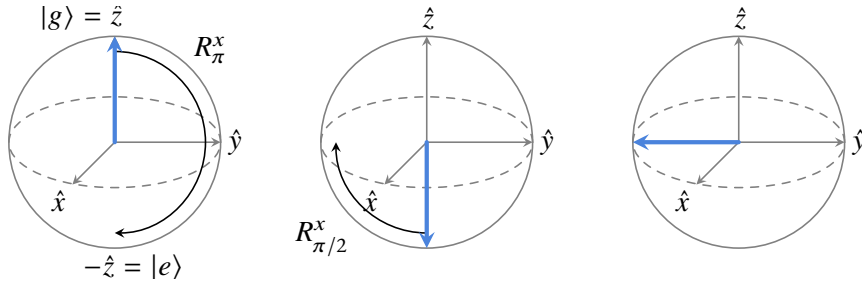


Figure C.10: Zero delay inversion-recovery T_1 pulse scheme depicted on the Bloch sphere. The “inversion” comes from the fact that the qubit state ends up along the $-y$ axis, and changes sign as the delay increases due to T_1 decay from the excited state back to the ground state.

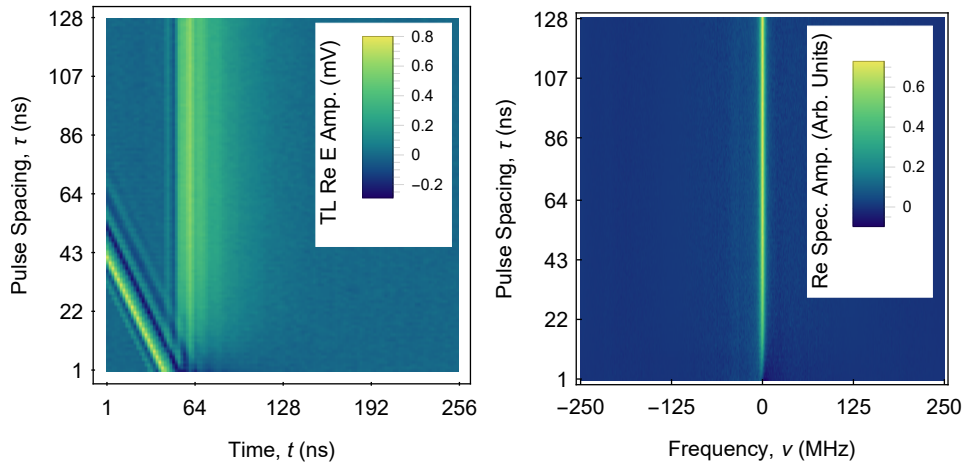


Figure C.11: Example of inversion recovery T_1 measurement. *Left*: real component of electric field amplitude signal recorded as a function of time and pulse delay. Note the spacing between the first pulse and the second pulse increasing from bottom to top as the first pulse is shifted earlier in time. *Right*: real component of the Fourier transformation of the post-pulse electric field amplitude as a function of time.

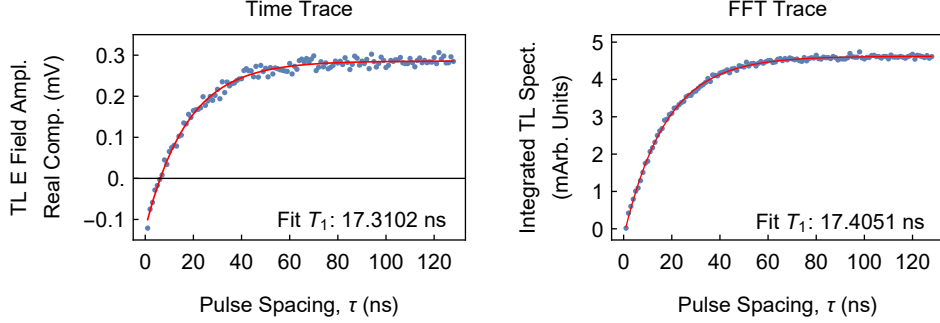


Figure C.12: Example of inversion recovery T_1 time traces. *Left*: real component of the electric field amplitude signal recorded at a specific time and plotted as a function of pulse delay. Note the slightly negative signal which decays to a positive signal at long delay times, the inversion recovery. *Right*: Integrated absolute spectral component at qubit frequency as a function of delay time. Here there is no longer inversion, but the filtering and integration that the Fourier transform provides reduces the SNR of the data.

C.5.2 Power

Instead of using inversion recovery, it is also possible for us to measure the T_1 time in the “standard” fashion. We apply a π pulse to the qubit and then look at the electric field power by post-processing our data (taking the absolute-value squared of the complex electric field signal, $(I_1 + iQ_1)^*(I_1 + iQ_1)$). However since this method overcomes the difference in measurement basis via signal processing and we have a large signal bandwidth, the power measurements have significantly lower signal-to-noise ratios that mean we have to average much longer. This makes the inversion recovery technique faster than the power measurement.

C.6 T_2 Measurements

In our measurement basis, T_2 measurements are more like T_1 measurements in standard cQED: we apply a $\pi/2$ pulse and observe the decay in the electric field amplitude as a function of time. The pulse scheme is provided in [Figure C.13](#) and also depicted on the Bloch sphere in [Figure C.14](#). As with the previous measurements, we can make the technique more selective by Fourier transforming and integrating over the appropriate frequency range. We did not even investigate standard cQED measurements such as a Ramsey measurement since our qubits do not live long enough to make these techniques worthwhile and the measurement method above is extremely fast in our measurement basis.

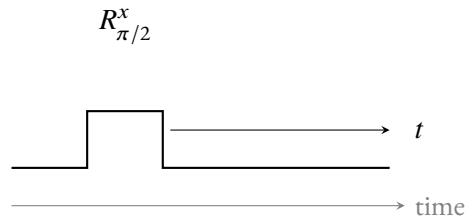


Figure C.13: Amplitude T_2 measurement pulse scheme.

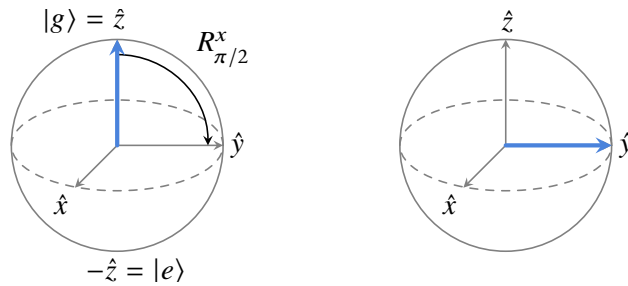


Figure C.14: Bloch sphere representation of the amplitude T_2 pulse sequence. $\pi/2$ pulse rotates the qubit into the measurement basis.

C.7 2D Spectroscopy

What is termed *two-dimensional electronic spectroscopy* (2DES) by the biophysics community is a four-wave mixing experiment involving three pulses, as shown in [Figure C.15](#). After collecting data as a function of t , τ , and T , the data is usually Fourier transformed across the t and τ axes, resulting in a COSY-like plot at each T point, which traces how energy flows through the system in real time.

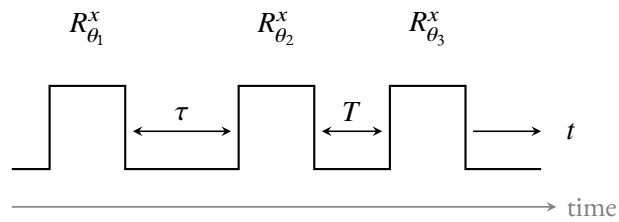


Figure C.15: Two dimensional pulse scheme.

Appendix D

COSY

D.1 Theory

Before I can discuss analytical modeling of the COSY pulse sequence, we need to find a method to propagate the density matrix through time that is computationally easier than the Liouville-von Neumann equation. Starting with a wavefunction, Ψ and assuming that its time evolution is a unitary operation, we can write

$$\Psi(t) = \hat{U}(t)\Psi(0).$$

Applying the Schrödinger equation gives

$$i\hbar \frac{\partial}{\partial t} \Psi(t) = \hat{H}\Psi(t).$$

Combining with these two equations gives

$$i\hbar \hat{U}'(t)\Psi(0) = \hat{H}\hat{U}(t)\Psi(0)$$

which can be solved by setting

$$\hat{U}(t) = e^{-i\hat{H}t/\hbar}.$$

Returning to the definition of the density matrix,

$$\rho(t) = |\Psi(t)\rangle \langle \Psi(t)|$$

we can apply the evolution operator \hat{U} from above to find that

$$\rho(t) = \hat{U}(t) |\Psi(0)\rangle \langle \Psi(0)| \hat{U}^\dagger(t)$$

or, in other words,

$$\rho(t) = \hat{U}(t)\rho(0)\hat{U}^\dagger(t).$$

Since this can be implemented in terms of matrices and matrix multiplication, this is easier to compute than the integration implied by the Liouville-von Neumann equation.

Now we have the toolbox to analytically compute the density matrix of the system during the COSY pulse sequence. To recap the sequence: we start in the ground state, apply a $\pi/2$ or $-\pi/2$ rotation around the x or y axis, allow the system to evolve for a time τ , apply another $\pi/2$ rotation, and then measure at the emitted electric field at a time t . Looking at a simple case of two qubits symmetrically coupled to a transmission line that are also transversely coupled to each other (as is the case of our qubits 1 and 2), we find that the initial state is

$$|\Psi_0\rangle = |g\rangle_1 \otimes |g\rangle_2$$

resulting in the initial density matrix

$$\rho_0 = |\Psi_0\rangle \langle \Psi_0|$$

I will assume that the pulses occur instantly (or with a nearly infinite Rabi rate) such that we can ignore qubit decay during the pulse and treat them as a simple unitary operation on the density matrix (although this could easily be extended to the case involving decay). The symmetric electric field drive has a Hamiltonian term

$$\hat{H}_{\text{drive}} = \frac{\Omega_R}{2} (\hat{\sigma}_1^+ + \hat{\sigma}_1^- + \hat{\sigma}_2^+ + \hat{\sigma}_2^-)$$

which can be re-written in terms of the σ^x operator, giving

$$\hat{H}_{\text{drive}} = \frac{\Omega_R}{2} (\hat{\sigma}_1^x + \hat{\sigma}_2^x)$$

which is more correctly given as

$$\hat{H}_{\text{drive}} = \frac{\Omega_R}{2} (\hat{\sigma}_1^x \otimes \hat{I}_2 + \hat{I}_1 \otimes \hat{\sigma}_2^x).$$

Incorporating this into a unitary time evolution operator, where I assume that $\Omega_R t = \pi/2$, I get

$$\hat{U}_X = \exp \left[-i\pi \left(\hat{\sigma}_1^x \otimes \hat{I}_2 + \hat{I}_1 \otimes \hat{\sigma}_2^x \right) / 4\hbar \right]$$

and the post-first-rotation density matrix is

$$\rho_1 = \hat{U}_X \rho_0 \hat{U}_X^\dagger.$$

Time evolution is slightly more complicated. For simple unitary time evolution of the qubits (with no dephasing or decay), we can use a typical Hamiltonian,

$$\hat{H}_0 = \frac{\hbar\omega_1}{2} \hat{\sigma}_1^z \otimes \hat{I}_2 + \frac{\hbar\omega_2}{2} \hat{I}_1 \otimes \hat{\sigma}_2^z + \frac{J}{2} (\hat{\sigma}_1^+ \otimes \hat{\sigma}_2^- + \hat{\sigma}_1^- \otimes \hat{\sigma}_2^+)$$

which we can apply by exponentiating to form the unitary time evolution operator as above ($e^{-i\hat{H}_0\tau/\hbar} \rho_1 e^{i\hat{H}_0\tau/\hbar}$). To include dephasing and decay, we follow the Lindbladian procedure, *i.e.* we add the terms $1/\sqrt{T_1} \mathcal{D}[\hat{\sigma}_1^- \otimes \hat{I}_2]$ and $1/\sqrt{T_1} \mathcal{D}[\hat{I}_1 \otimes \hat{\sigma}_2^-]$ to add decay at

a rate $1/T_1$ and the terms $1/\sqrt{2T_\phi} \mathcal{D}[\hat{\sigma}_1^z \otimes \hat{I}_2]$ and $1/\sqrt{2T_\phi} \mathcal{D}[\hat{I}_1 \otimes \hat{\sigma}_2^z]$ to add dephasing at a rate of $1/T_\phi$. Thus

$$\dot{\rho} = -\frac{i}{\hbar} [H_0, \rho] + L(\rho)$$

where

$$L(\rho) = \frac{1}{\sqrt{T_1}} \left(\mathcal{D}[\hat{\sigma}_1^- \otimes \hat{I}_2] + \mathcal{D}[\hat{I}_1 \otimes \hat{\sigma}_2^-] \right) + \frac{1}{\sqrt{2T_\phi}} \left(\mathcal{D}[\hat{\sigma}_1^z \otimes \hat{I}_2] + \mathcal{D}[\hat{I}_1 \otimes \hat{\sigma}_2^z] \right)$$

Since the collapse operator terms involve operating from the left and right, we can no longer trivially exponentiate to find the time propagation operator in this case. However, by applying the various theorems of [86, Chp. 4], we can *vectorize* the density matrix (stacking either the rows or the columns) and create a *supermatrix* equation (where if ρ is a $n \times n$ density matrix, \mathbb{L} is $n^2 \times n^2$) [87]:

$$\dot{\vec{\rho}} = \mathbb{L}\vec{\rho}$$

which can now be trivially exponentiated such that

$$\vec{\rho}(t) = e^{\mathbb{L}t} \vec{\rho}(0)$$

so

$$\vec{\rho}_2 = e^{\mathbb{L}\tau} \vec{\rho}_1.$$

Now, we have another $\pi/2$ rotation pulse, so

$$\rho_3 = \hat{U}_X \rho_2 \hat{U}_X^\dagger$$

which is followed by the final time evolution for time t , resulting in

$$\vec{\rho}_4 = e^{\mathbb{L}t} \vec{\rho}_3.$$

Finally, we measure the electric field in the transmission line:

$$V_{XX} \propto \langle \hat{\sigma}_1^x + \hat{\sigma}_2^x \rangle = \text{Tr} \left[\rho_4 \left(\hat{\sigma}_1^x \otimes \hat{I}_2 + \hat{I}_1 \otimes \hat{\sigma}_2^x \right) \right].$$

Calculating all of this out results in tremendously large terms (too large for me to reproduce here in a reasonable amount of time) which all have roughly equal dependence on the different time scales (t, τ, T_1, T_ϕ) and hence cannot be meaningfully simplified. Calculating these terms for different initial pulse phases (see next section) and Fourier transforming gives diagonal peaks at the qubit frequencies and an off-diagonal cross peak, as I explained in the main text.

Here I have explicitly not written operators as matrices in a particular basis, although the usual choice is the “computational basis” where $|g\rangle \equiv \begin{pmatrix} 1 \\ 0 \end{pmatrix}$ and $|e\rangle \equiv \begin{pmatrix} 0 \\ 1 \end{pmatrix}$ and the Pauli matrices are given in their usual form.

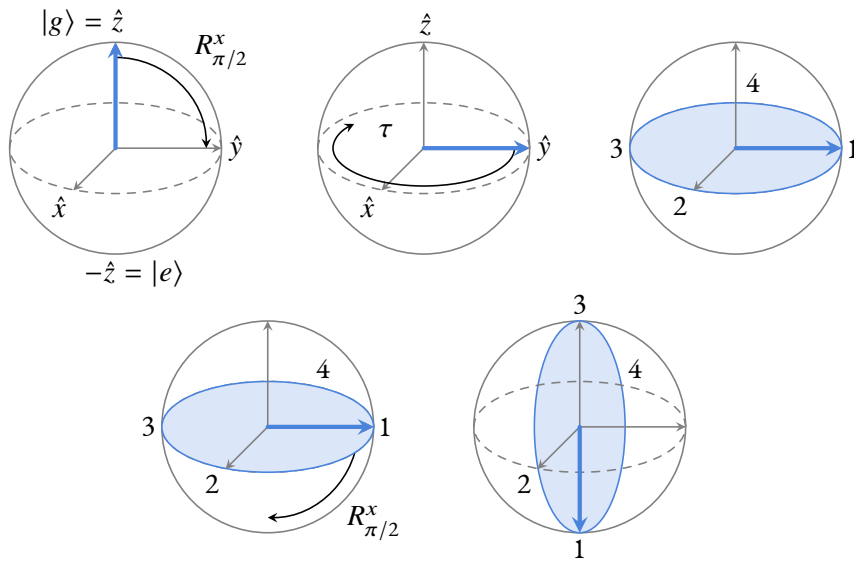


Figure D.1: XX pulse sequence. The initial $X \equiv R_{\pi/2}^x$ pulse rotates the qubit into the equatorial plane of the Bloch sphere. After allowing for the system to evolve for time τ , the qubit has precessed some distance around the equator or decayed; here I have labeled the points of τ evolution in the order that they would be reached. The second X pulse then rotates the qubit again, meaning that only part of the “precession disk” remains in the measurement basis, and furthermore, brings a qubit that has decayed to the ground state back to the equatorial plane.

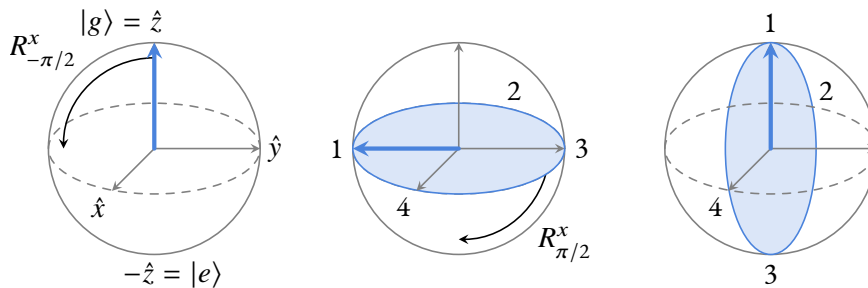


Figure D.2: $\bar{X}X$ pulse sequence

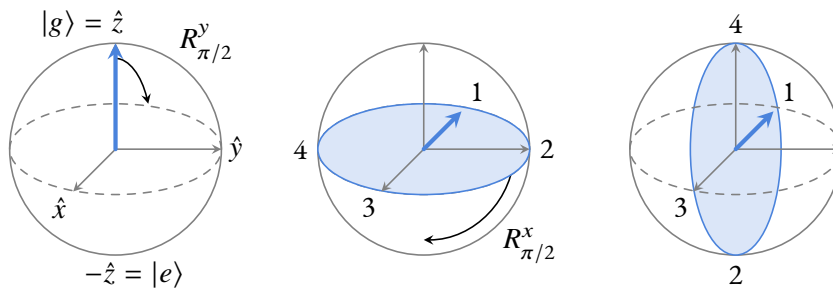


Figure D.3: YX pulse sequence.

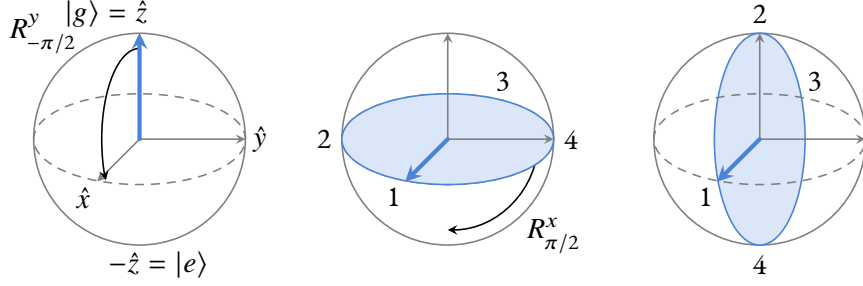


Figure D.4: $\bar{Y}X$ pulse sequence.

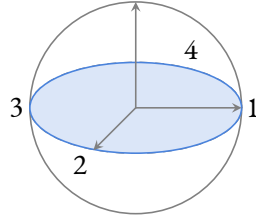


Figure D.5: Final signal

D.2 Phase Cycling

Since we only measure in the equatorial plane of the Bloch sphere, we should now limit ourselves to only these points. Looking at the results of the XX and $\bar{X}X$ pulse sequences (Figure D.1 and Figure D.2), we see that we can combine the equatorial signals and cancel the remaining ones (due to *e.g.* decay into the ground state during the τ evolution time) by subtracting one from another. A similar relation holds for the YX and $\bar{Y}X$ pulses (Figure D.3 and Figure D.4). In order to recover the full τ dynamics, we have to combine these two pairs, since they each contain only part of the full signal in the equatorial plane. In order to combine them into a full diagram on the equator with the correct time-ordering, we should combine them with a phase shift of i . Therefore, the final phase-cycle corrected signal is

$$S_{PC} = XX + iYX - (\bar{X}X + i\bar{Y}X) \tag{D.1}$$

resulting in an equatorial projection depicted in Figure D.5.

D.3 Data Processing

The details of the data processing for COSY measurements are quite similar to those discussed previously. We begin by collecting the electric field amplitude as a function of

time for different time delays and pulse sequences (phase cycling). Next, we combine the data in the correct phase-cycled manner (Equation D.1), still as a function of time, producing the characteristic diagonal oscillations as shown in Figure D.6.

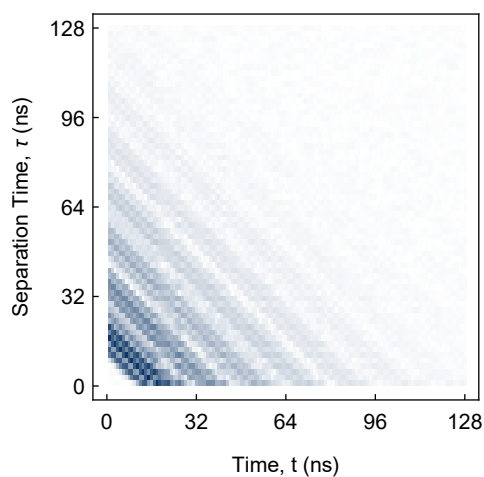


Figure D.6: Phase-cycle corrected electric field amplitude plotted versus time, t , and pulse separation, τ .

Fourier transforming across both dimensions results in the plot shown previously (Figure 3.9). To demonstrate how important phase cycling is to the data processing, I have plotted the equivalent figure without any phase cycling below in Figure D.7.

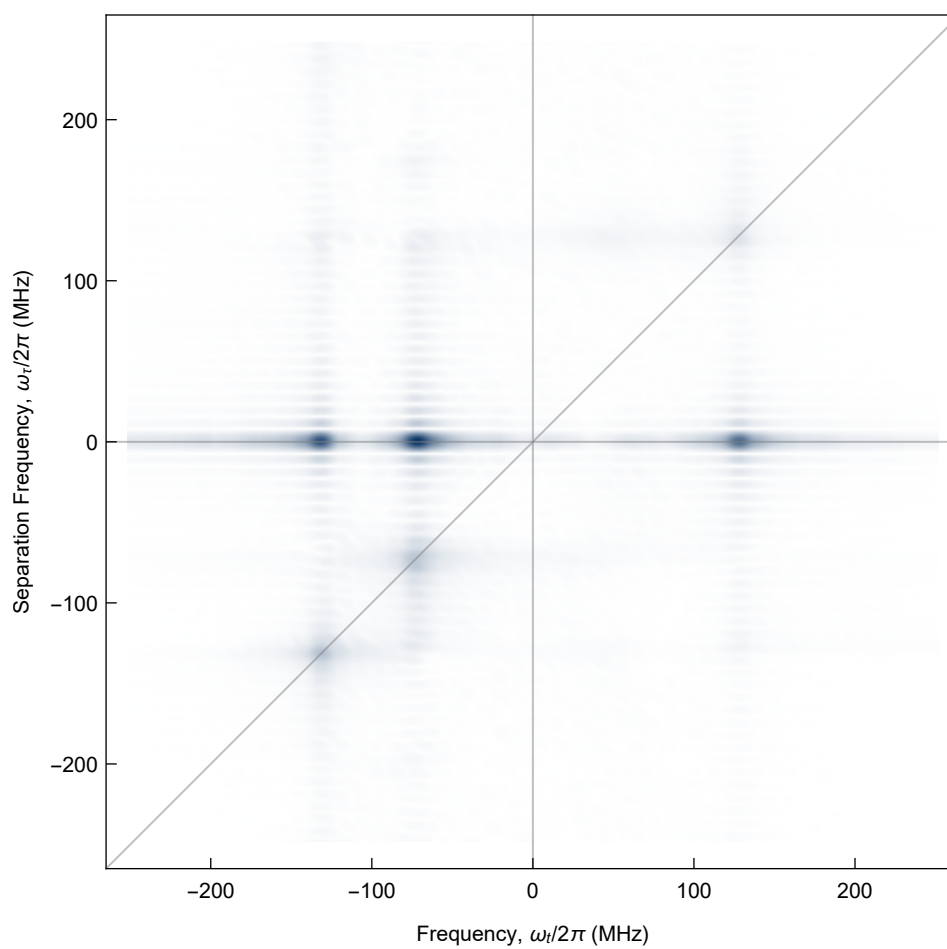


Figure D.7: Uncorrected COSY Fourier signal plotted versus separation frequency, $\omega_\tau/2\pi$, and frequency, $\omega_t/2\pi$. Note the strong DC component which hides the diagonal and off-diagonal cross-peaks.

Appendix E

Parameters

E.1 Numerical Simulations

Table E.1: Numerical simulation system parameters

Parameter	Value (Hz)
$\omega_1/2\pi$	6.313×10^9
$\omega_2/2\pi$	6.313×10^9
$\omega_3/2\pi$	6.193×10^9
$\omega_r/2\pi$	6.00×10^9
$J_{12}/2\pi$	120 $\times 10^6$
$J_{13}/2\pi$	8 $\times 10^6$
$J_{23}/2\pi$	37 $\times 10^6$
$g_{1r}/2\pi$	0
$g_{2r}/2\pi$	0
$g_{3r}/2\pi$	90 $\times 10^6$
$\kappa_{TL}/2\pi$	10 $\times 10^6$
$\gamma_{*,1}/2\pi$	0
$\gamma_{*,2}/2\pi$	0
$\gamma_{*,3}/2\pi$	0
$\gamma_r/2\pi$	35 $\times 10^6$
$E_{\text{drive}}/2\pi$	8 $\times 10^6$
$\omega_{\text{drive}}/2\pi$	6.433×10^9

The thermal photon population, n_{th} , was taken to be zero. Resonator power time traces were calculated for qubit 2 dephasing rates, γ , of 10 MHz, 20 MHz, 30 MHz, 50 MHz and 70 MHz.

Bibliography

- [1] Joeri Rogelj, Alexander Popp, Katherine V. Calvin, Gunnar Luderer, Johannes Emmerling, David Gernaat, Shinichiro Fujimori, Jessica Streffer, Tomoko Hasegawa, Giacomo Marangoni, Volker Krey, Elmar Kriegler, Keywan Riahi, Detlef P. van Vuuren, Jonathan Doelman, Laurent Drouet, Jae Edmonds, Oliver Fricko, Mathijs Harmsen, Petr Havlík, Florian Humpenöder, Elke Stehfest, and Massimo Tavoni. “Scenarios towards limiting global mean temperature increase below 1.5 °C”. In: *Nature Climate Change* (Mar. 5, 2018). DOI: [10.1038/s41558-018-0091-3](https://doi.org/10.1038/s41558-018-0091-3).
- [2] Wenping Yuan, Shuguang Liu, Guirui Yu, Jean-Marc Bonnefond, Jiquan Chen, Ken Davis, Ankur R. Desai, Allen H. Goldstein, Damiano Gianelle, Federica Rossi, Andrew E. Suyker, and Shashi B. Verma. “Global estimates of evapotranspiration and gross primary production based on MODIS and global meteorology data”. In: *Remote Sensing of Environment* 114.7 (Mar. 12, 2010), pp. 1416–1431. DOI: [10.1016/j.rse.2010.01.022](https://doi.org/10.1016/j.rse.2010.01.022).
- [3] Robert E. Blankenship. *Molecular Mechanisms of Photosynthesis*. Blackwell Science Ltd., 2008. ISBN: 9780470758472. DOI: [10.1002/9780470758472](https://doi.org/10.1002/9780470758472).
- [4] R. E. Fenna and B. W. Matthews. “Chlorophyll arrangement in a bacteriochlorophyll protein from *Chlorobium limicola*”. In: *Nature* 258 (Dec. 18, 1975), pp. 573–577. DOI: [10.1038/258573a0](https://doi.org/10.1038/258573a0).
- [5] John M. Olson and Carol A. Romano. “A new chlorophyll from green bacteria”. In: *Biochimica et Biophysica Acta* 59 (3 June 4, 1962), pp. 726–728. DOI: [10.1016/0006-3002\(62\)90659-5](https://doi.org/10.1016/0006-3002(62)90659-5).
- [6] Robert E. Blankenship and Katsumi Matsuura. “Antenna Complexes from Green Photosynthetic Bacteria”. In: *Light-Harvesting Antennas in Photosynthesis*. Ed. by Beverley R. Green and William W. Parson. 2003, pp. 195–217. ISBN: 9789401720878. DOI: [10.1007/978-94-017-2087-8_6](https://doi.org/10.1007/978-94-017-2087-8_6).
- [7] Dale E. Tronrud, Jianzhong Wen, Leslie Gay, and Robert E. Blankenship. “The Structural basis for the difference in absorbance spectra for the FMO antenna protein from various green sulfur bacteria”. In: *Photosynthesis Research* 100.2 (May 1, 2009), pp. 79–87. DOI: [10.1007/s11120-009-9430-6](https://doi.org/10.1007/s11120-009-9430-6).
- [8] LLC Schrödinger. “The PyMOL Molecular Graphics System, Version 2.0.6”. 2017.

- [9] Anja Krieger-Liszky. “Singlet oxygen production in photosynthesis”. In: *Journal of Experimental Botany* 56.411 (Aug. 13, 2004), pp. 337–346. DOI: [10.1093/jxb/erh237](https://doi.org/10.1093/jxb/erh237).
- [10] J. Frenkel. “On the Transformation of light into Heat in Solids. I”. In: *Physical Review* 37 (1 Jan. 1, 1931), pp. 17–44. DOI: [10.1103/PhysRev.37.17](https://doi.org/10.1103/PhysRev.37.17).
- [11] J. Frenkel. “On the Transformation of light into Heat in Solids. II”. In: *Physical Review* 37 (10 May 15, 1931), pp. 1276–1294. DOI: [10.1103/PhysRev.37.1276](https://doi.org/10.1103/PhysRev.37.1276).
- [12] Herbert van Amerongen, Rienk van Grondelle, and Leonas Valkunas. *Photosynthetic Excitons*. World Scientific, June 2000. ISBN: 9789810232801. DOI: [10.1142/9789812813664](https://doi.org/10.1142/9789812813664).
- [13] James Franck and Edwards Teller. “Migration and Photochemical Action of Excitation Energy in Crystals”. In: *Journal of Chemical Physics* 6 (Dec. 1938), pp. 861–872. DOI: [10.1063/1.1750182](https://doi.org/10.1063/1.1750182).
- [14] Theodore Förster. “Energiewanderung und Fluoreszenz”. In: *Die Naturwissenschaften* 33 (6 June 1946), pp. 166–175. DOI: [10.1007/BF00585226](https://doi.org/10.1007/BF00585226).
- [15] Patrick Rebentrost, Masoud Mohseni, Ivan Kassal, Seth Lloyd, and Alán Aspuru-Guzik. “Environment-Assisted Quantum Transport”. In: *New Journal of Physics* 11 (Mar. 3, 2009), p. 033003. DOI: [10.1088/1367-2630/11/3/033003](https://doi.org/10.1088/1367-2630/11/3/033003).
- [16] Koichiro Mukai, Shuji Abe, and Hitoshi Sumi. “Theory of Rapid Excitation-Energy Transfer from B800 to Optically-Forbidden Exciton States of B850 in the Antenna System LH2 of Photosynthetic Purple Bacteria”. In: *Journal of Physical Chemistry B* 103.29 (July 3, 1999), pp. 6096–6102. DOI: [10.1021/jp984469g](https://doi.org/10.1021/jp984469g).
- [17] Gregory S. Engel, Tessa R. Calhoun, Elizabeth L. Read, Tae-Kyu Ahn, Tomáš Mančal, Yuan-Chung Cheng, Robert E. Blankenship, and Graham R. Fleming. “Evidence for wavelike energy transfer through quantum coherence in photosynthetic systems”. In: *Nature* 446 (Apr. 12, 2007), pp. 782–786. DOI: [10.1038/nature05678](https://doi.org/10.1038/nature05678).
- [18] Gitt Panitchayangkoon, Dugan Hayes, Kelly A. Fransted, Justin R. Caram, Elad Harel, Jianzhong Wen, Robert E. Blankenship, and Gregory S. Engel. “Long-lived quantum coherence in photosynthetic complexes at physiological temperature”. In: *Proceedings of the National Academy of Sciences* 107.29 (July 20, 2010), pp. 12766–12770. DOI: [10.1073/pnas.1005484107](https://doi.org/10.1073/pnas.1005484107).
- [19] Hiroshi Huzisige and Bacon Ke. “Dynamics of the history of photosynthesis research”. In: *Photosynthesis Research* 38 (1993), pp. 185–209. DOI: [10.1007/BF00146418](https://doi.org/10.1007/BF00146418).
- [20] L. N. M. Duysens. “Photosynthesis”. In: *Progress in Biophysics and Molecular Biology* 14 (1961), pp. 1–104. DOI: [10.1016/S0079-6107\(64\)80003-1](https://doi.org/10.1016/S0079-6107(64)80003-1).

- [21] Francesco Pellegrino. “Ultrafast energy transfer processes in photosynthetic systems probed by picosecond fluorescence spectroscopy”. In: *Optical Engineering* 22.5 (Sept. 1983), pp. 508–520. DOI: [10.1117/12.7973190](https://doi.org/10.1117/12.7973190).
- [22] Michael Seibert and Robert R. Alfano. “Probing Photosynthesis on a Picosecond Time Scale. Evidence for Photosystem I and Photosystem II Fluorescence in Chloroplasts”. In: *Biophysical Journal* 14 (4 Apr. 1974), pp. 269–283. DOI: [10.1016/S0006-3495\(74\)85915-1](https://doi.org/10.1016/S0006-3495(74)85915-1).
- [23] Antonius M. Nuijs, Henk Vasmel, H. Laura P. Joppe, Louis N. M. Duysens, and Jan Amesz. “Excited states and primary charge separation in the pigment system of the green photosynthetic bacterium *Prosthecochloris aestuarii* as studied by picosecond absorbance difference spectroscopy”. In: *Biochimica et Biophysica Acta - Bioenergetics* 807.1 (1985), pp. 24–34. DOI: [10.1016/0005-2728\(85\)90049-0](https://doi.org/10.1016/0005-2728(85)90049-0).
- [24] Gitt Panitchayangkoon, Dmitri V. Voronine, Darius Abramavicius, Justin R. Caram, Nicholas H. C. Lewis, Shaul Mukamel, and Gregory S. Engel. “Direct evidence of quantum transport in photosynthetic light-harvesting complexes”. In: *Proceedings of the National Academy of Sciences* 108 (Dec. 27, 2011), pp. 20908–20912. DOI: [10.1073/pnas.1105234108](https://doi.org/10.1073/pnas.1105234108).
- [25] Darius Abramavicius and Shaul Mukamel. “Quantum oscillatory exciton migration in photosynthetic reaction centers”. In: *Journal of Chemical Physics* 133.6 (Aug. 13, 2010), p. 064510. DOI: [10.1063/1.3458824](https://doi.org/10.1063/1.3458824).
- [26] Alexander Eisfeld and John S. Briggs. “Classical master equation for excitonic transport under the influence of an environment”. In: *Physical Review E* 85 (4 Apr. 30, 2012), p. 046118. DOI: [10.1103/PhysRevE.85.046118](https://doi.org/10.1103/PhysRevE.85.046118).
- [27] David M. Wilkins and Nikesh S. Dattani. “Why Quantum Coherence Is Not Important in the Fenna–Matthews–Olsen Complex”. In: *Journal of Chemical Theory and Computation* 11 (7 Mar. 4, 2015), pp. 3411–3419. DOI: [10.1021/ct501066k](https://doi.org/10.1021/ct501066k).
- [28] Leonardo A. Pachón and Paul Brumer. “Incoherent excitation of thermally equilibrated open quantum systems”. In: *Physical Review A* 87 (2 Feb. 7, 2013), p. 022106. DOI: [10.1103/PhysRevA.87.022106](https://doi.org/10.1103/PhysRevA.87.022106).
- [29] Leonardo A. Pachón, Juan D. Botero, and Paul Brumer. “Open system perspective on incoherent excitation of light-harvesting systems”. In: *Journal of Physics B: Atomic, Molecular and Optical Physics* 50.18 (Sept. 4, 2017), p. 184003. DOI: [10.1088/1361-6455/aa8696](https://doi.org/10.1088/1361-6455/aa8696).
- [30] Hong-Guang Duan, Valentyn I. Prokhorenko, Richard J. Cogdell, Khuram Ashraf, Amy L. Stevens, Michael Thorwart, and R. J. Dwayne Miller. “Nature does not rely on long-lived electronic quantum coherence for photosynthetic energy transfer”. In: *Proceedings of the National Academy of Sciences* 114.32 (Aug. 8, 2017), pp. 8493–8498. DOI: [10.1073/pnas.1702261114](https://doi.org/10.1073/pnas.1702261114).

- [31] S. F. Huelga and M. B. Plenio. “Vibrations, quanta and biology”. In: *Contemporary Physics* 54.4 (Nov. 13, 2013), pp. 181–207. DOI: [10.1080/00405000.2013.829687](https://doi.org/10.1080/00405000.2013.829687).
- [32] Elisabet Romero, Vladimir I. Novoderezhkin, and Rienk van Grondelle. “Quantum design of photosynthesis for bio-inspired solar-energy conversion”. In: *Nature* 543 (Mar. 15, 2017), pp. 355–365. DOI: [10.1038/nature22012](https://doi.org/10.1038/nature22012).
- [33] M. B. Plenio and S. F. Huelga. “Dephasing-assisted transport: quantum networks and biomolecules”. In: *New Journal of Physics* 10.11 (Nov. 14, 2008), p. 113019. DOI: [10.1088/1367-2630/10/11/113019](https://doi.org/10.1088/1367-2630/10/11/113019).
- [34] Masoud Mohseni, Patrick Rebentrost, Seth Lloyd, and Alán Aspuru-Guzik. “Environment-assisted quantum walks in photosynthetic energy transfer”. In: *Journal of Chemical Physics* 129.17 (Nov. 6, 2008), p. 174106. DOI: [10.1063/1.3002335](https://doi.org/10.1063/1.3002335).
- [35] Lov K. Grover. “Quantum Mechanics Helps in Searching for a Needle in a Haystack”. In: *Physical Review Letters* 79.2 (July 14, 1997), pp. 325–328. DOI: [10.1103/PhysRevLett.79.325](https://doi.org/10.1103/PhysRevLett.79.325).
- [36] Patrick Rebentrost, Masoud Mohseni, and Alán Aspuru-Guzik. “Role of Quantum Coherence and Environmental Fluctuations in Chromophoric Energy Transport”. In: *Journal of Physical Chemistry B* 113.29 (June 24, 2009), pp. 9942–9947. DOI: [10.1021/jp901724d](https://doi.org/10.1021/jp901724d).
- [37] Francesca Fassioli, Raymond Dinshaw, Paul C. Arpin, and Gregory D. Scholes. “Photosynthetic light harvesting: excitons and coherence”. In: *Journal of The Royal Society Interface* 11.92 (2014). DOI: [10.1098/rsif.2013.0901](https://doi.org/10.1098/rsif.2013.0901).
- [38] Richard P. Feynman. “Simulating physics with computers”. In: *International Journal of Theoretical Physics* 21 (6–7 June 1982), pp. 467–488. DOI: [10.1007/BF02650179](https://doi.org/10.1007/BF02650179).
- [39] Matthew Neeley, Markus Ansmann, Radoslaw C. Bialczak, Max Hofheinz, Erik Lucero, Aaron D. O’Connell, Daniel Sank, Haohua Wang, James Wenner, Andrew N. Cleland, Michael R. Geller, and John M. Martinis. “Emulation of a Quantum Spin with a Superconducting Phase Qudit”. In: *Science* 325.5941 (Aug. 7, 2009), pp. 722–725. DOI: [10.1126/science.1173440](https://doi.org/10.1126/science.1173440).
- [40] K. Kim, M.-S. Chang, S. Korenblit, R. Islam, E. E. Edwards, J. K. Freericks, G.-D. Lin, L.-M. Duan, and C. Monroe. “Quantum simulation of frustrated Ising spins with trapped ions”. In: *Nature* 465 (June 3, 2010), pp. 590–593. DOI: [10.1038/nature09071](https://doi.org/10.1038/nature09071).
- [41] Markus Greiner, Olaf Mandel, Tilman Esslinger, Theodor W. Hänsch, and Immanuel Bloch. “Quantum phase transition from a superfluid to a Mott insulator in a gas of ultracold atoms”. In: *Nature* 415 (Jan. 3, 2002), pp. 39–44. DOI: [10.1038/415039a](https://doi.org/10.1038/415039a).
- [42] I. M. Georgescu, S. Ashhab, and Franco Nori. “Quantum simulation”. In: *Reviews of Modern Physics* 86 (1 Mar. 10, 2014), pp. 153–185. DOI: [10.1103/RevModPhys.86.153](https://doi.org/10.1103/RevModPhys.86.153).

- [43] Sarah Mostame, Patrick Rebentrost, Alexander Eisfeld, Andrew J. Kerman, Dimitris I. Tsomokos, and Alán Aspuru-Guzik. “Quantum simulator of open quantum systems using superconducting qubits: exciton transport in photosynthetic complexes”. In: *New Journal of Physics* 14 (Oct. 10, 2012), p. 105013. DOI: [10.1088/1367-2630/14/10/105013](https://doi.org/10.1088/1367-2630/14/10/105013).
- [44] L. D. Contreras-Pulido, M. Bruderer, S. F. Huelga, and M. B. Plenio. “Dephasing-assisted transport in linear triple quantum dots”. In: *New Journal of Physics* 16 (Nov. 24, 2014), p. 113061. DOI: [10.1088/1367-2630/16/11/113061](https://doi.org/10.1088/1367-2630/16/11/113061).
- [45] Roberto de J. Leòn-Montiel, Mario A. Quiroz-Juárez, Rafael Quintero-Torres, Jorge L. Domínguez-Juárez, Héctor M. Moya-Cessa, Juan P. Torres, and José L. Aragón. “Noise-assisted energy transport in electrical oscillator networks with off-diagonal dynamical disorder”. In: *Scientific Reports* 5 (Nov. 27, 2015), p. 17339. DOI: [10.1038/srep17339](https://doi.org/10.1038/srep17339).
- [46] Devon N. Biggerstaff, René Heilmann, Aidan A. Zecevik, Markus Gräfe, Matthew A. Broome, Alessandro Fedrizzi, Stefan Nolte, Alexander Szameit, Andrew G. White, and Ivan Kassal. “Enhancing coherent transport in a photonic network using controllable decoherence”. In: *Nature Communications* 7 (Apr. 15, 2016), p. 11282. DOI: [10.1038/ncomms11282](https://doi.org/10.1038/ncomms11282).
- [47] Hiroshi Imada, Kuniyuki Miwa, Miyabi Imai-Imada, Shota Kawahara, Kensuke Kimura, and Yousoo Kim. “Real-space investigation of energy transfer in heterogeneous molecular dimers”. In: *Nature* 538 (Oct. 3, 2016), pp. 364–367. DOI: [10.1038/nature19765](https://doi.org/10.1038/nature19765).
- [48] Nicholas C. Harris, Gregory R. Steinbrecher, Mihika Prabhu, Yoav Lahini, Jacob Mower, Darius Bunandar, Changchen Chen, Franco N. C. Wong, Tom Baehr-Jones, Michael Hochberg, Seth Lloyd, and Dirk Englund. “Quantum transport simulations in a programmable nanophotonic processor”. In: *Nature Photonics* 11 (June 19, 2017), pp. 447–452. DOI: [10.1038/nphoton.2017.95](https://doi.org/10.1038/nphoton.2017.95).
- [49] Anton Potočnik, Arno Bargerbos, Florian A. Y. N. Schröder, Saeed A. Khan, Michele C. Collodo, Simone Gasparinetti, Yves Salathé, Celestino Creatore, Christopher Eichler, Hakan E. Türeci, Alex W. Chin, and Andreas Wallraff. “Studying light-harvesting models with superconducting circuits”. In: *Nature Communications* 9 (1 Mar. 2, 2018), p. 904. DOI: [10.1038/s41467-018-03312-x](https://doi.org/10.1038/s41467-018-03312-x).
- [50] Dylan J Gorman, Boerge Hemmerling, Eli Megidish, Soenke A. Moeller, Philipp Schindler, Mohan Sarovar, and Hartmut Haeflner. “Engineering Vibrationally Assisted Energy Transfer in a Trapped-Ion Quantum Simulator”. In: *Physical Review X* 8 (1 Mar. 7, 2018), p. 011038. DOI: [10.1103/PhysRevX.8.011038](https://doi.org/10.1103/PhysRevX.8.011038).
- [51] Adrian Beckert. “Towards the realization fo a transmon longitudinally coupled to a lumped element resonator”. Master’s Thesis. ETH Zürich, 2016.
- [52] Brian David Josephson. “Possible new effects in superconductive tunnelling”. In: *Physics Letters* 1.7 (June 1, 1962), pp. 251–253. DOI: [10.1016/0031-9163\(62\)91369-0](https://doi.org/10.1016/0031-9163(62)91369-0).

- [53] Martin Volker Göppl. “Engineering Quantum Electronic Chips—Realization and Characterization of Circuit Quantum Electrodynamics Systems”. PhD. Thesis. ETH Zürich, 2009. DOI: [10.3929/ethz-a-005816478](https://doi.org/10.3929/ethz-a-005816478).
- [54] Steven M. Girvin. “Circuit QED: superconducting qubits coupled to microwave photons”. In: *Quantum Machines: Measurement and Control of Engineered Quantum Systems. Lectures Notes of the Les Houches Summer School: Volume 96, July 2011*. Ed. by Michel Devoret, Benjamin Huard, Robert Schoelkopf, and Leticia F. Cugliandolo. June 12, 2014, pp. 113–255. ISBN: 9780199681181. DOI: [10.1093/acprof:oso/9780199681181.001.0001](https://doi.org/10.1093/acprof:oso/9780199681181.001.0001).
- [55] Arno Bargerbos. “Analog Quantum Simulation of Noise Assisted Transport in Light Harvesting Structures with Superconducting Circuits”. Master’s Thesis. ETH Zürich, Oct. 6, 2016.
- [56] Edward Mills Purcell. “Spontaneous Emission Probabilities at Radio Frequencies”. In: *Physical Review* 69 (11–12 June 1946), p. 674. DOI: [10.1103/PhysRev.69.674](https://doi.org/10.1103/PhysRev.69.674).
- [57] Michel H. Devoret. “Quantum Fluctuations in Electrical Circuits”. In: *Les Houches Session LXIII, Quantum Fluctuations*. Ed. by S Reynaud, E. Giacobino, and J. Zinn-Justin. 1997, pp. 351–386. ISBN: 9780444825933.
- [58] Uri Vool and Michel Devoret. “Introduction to quantum electromagnetic circuits”. In: *International Journal of Circuit Theory and Applications* 45 (7 June 5, 2017), pp. 897–934. DOI: [10.1002/cta.2359](https://doi.org/10.1002/cta.2359).
- [59] H. Haken and G. Strobl. “Exact treatment of coherent and incoherent triplet exciton migration”. In: *The Triplet State. Proceedings of an International Symposium Held at the American University of Beirut, Lebanon*. Ed. by A. B. Zahlan. 1967, pp. 311–314. ISBN: 9780521126502.
- [60] H. Haken and P. Reineker. “The coupled coherent and incoherent motion of excitons and its influence on the line shape of optical absorption”. In: *Zeitschrift für Physik* 249.3 (June 1, 1972), pp. 253–268. DOI: [10.1007/BF01400230](https://doi.org/10.1007/BF01400230).
- [61] H. Haken and G. Strobl. “An exactly solvable model for coherent and incoherent exciton motion”. In: *Zeitschrift für Physik A Hadrons and nuclei* 262.2 (Apr. 1, 1973), pp. 135–148. DOI: [10.1007/BF01399723](https://doi.org/10.1007/BF01399723).
- [62] Carsten Olbrich, Johan Strümpfer, Klaus Schulten, and Ulrich Kleinekathöfer. “Quest for Spatially Correlated Fluctuations in the FMO Light-Harvesting Complex”. In: *Journal of Physical Chemistry B* 115.4 (2011), pp. 758–764. DOI: [10.1021/jp1099514](https://doi.org/10.1021/jp1099514).
- [63] Zhiren Wang. “Development of Sputtering Process for High Quality Nb Thin Film”. Master’s Thesis. Grenoble and ETH Zürich, Aug. 31, 2017.
- [64] Marlan O. Scully. “Quantum Photocell: Using Quantum Coherence to Reduce Radiative Recombination and Increase Efficiency”. In: *Physical Review Letters* 104 (20 May 21, 2010), p. 207701. DOI: [10.1103/PhysRevLett.104.207701](https://doi.org/10.1103/PhysRevLett.104.207701).

- [65] C. Creatore, M. A. Parker, S. Emmott, and A. W. Chin. “Efficient Biologically Inspired Photocell Enhanced by Delocalized Quantum States”. In: *Physical Review Letters* 111 (25 Dec. 18, 2013), p. 253601. DOI: [10.1103/PhysRevLett.111.253601](https://doi.org/10.1103/PhysRevLett.111.253601).
- [66] K. D. B. Higgins, S. C. Benjamin, T. M. Stace, G. J. Milburn, B. W. Lovett, and E. M. Gauger. “Superabsorption of light via quantum engineering”. In: *Nature Communications* 5 (Aug. 22, 2014), p. 4705. DOI: [10.1038/ncomms5705](https://doi.org/10.1038/ncomms5705).
- [67] Yiteng Zhang, Sangchul Oh, Fahhad H. Alharbi, Gregory S. Engel, and Sabre Kais. “Delocalized quantum states enhance photocell efficiency”. In: *Physical Chemistry Chemical Physics* 17 (Jan. 16, 2015), pp. 5743–5750. DOI: [10.1039/C4CP05310A](https://doi.org/10.1039/C4CP05310A).
- [68] K. D. B. Higgins, B. W. Lovett, and E. M. Gauger. “Quantum-Enhanced Capture of Photons Using Optical Ratchet States”. In: *Journal of Physical Chemistry C* 121.38 (Aug. 23, 2017), pp. 20714–20719. DOI: [10.1021/acs.jpcc.7b07138](https://doi.org/10.1021/acs.jpcc.7b07138).
- [69] Frank Pobell. *Matter and Methods at Low Temperatures*. 3rd ed. Springer, 2007. ISBN: 9783540463566.
- [70] Yves Salathé. “Towards Gigahertz Bandwidth Digital Signal Processing in Circuit Quantum Electrodynamics”. Master’s Thesis. ETH Zürich, Oct. 7, 2011.
- [71] Simon Storz. “Spectroscopy Automation and Sample Characterization of Superconducting Qubits”. Master’s Thesis. ETH Zürich, Dec. 21, 2016.
- [72] Peter J. Brockwell and Richard A. Davis. *Introduction to Time Series and Forecasting*. 3rd ed. Springer, 2016. ISBN: 9783319298528. DOI: [10.1007/978-3-319-29854-2](https://doi.org/10.1007/978-3-319-29854-2).
- [73] Alexey B. Pavolotsky, Dimitar Dochev, and Victor Belitsky. “Aging- and annealing-induced variations in Nb/Al–AlO_x/Nb tunnel junction properties”. In: *Journal of Applied Physics* 109.2 (Jan. 19, 2011), p. 024502. DOI: [10.1063/1.3532040](https://doi.org/10.1063/1.3532040).
- [74] I. M. Pop, T. Fournier, T. Crozes, F. Lecocq, I. Matei, B Pannetier, O. Buisson, and W. Guichard. “Fabrication of stable and reproducible submicron tunnel junctions”. In: *Journal of Vacuum Science & Technology B, Nanotechnology and Microelectronics: Materials, Processing, Measurement, and Phenomena* 30.1 (2012), p. 010607. DOI: [10.1116/1.3673790](https://doi.org/10.1116/1.3673790).
- [75] Eyob A. Sete, Jay M. Gambetta, and Alexander N. Korotkov. “Purcell effect with microwave drive: Suppression of qubit relaxation rate”. In: *Physical Review B* 89 (10 Mar. 21, 2014), p. 104516. DOI: [10.1103/PhysRevB.89.104516](https://doi.org/10.1103/PhysRevB.89.104516).
- [76] Malcolm H. Levitt. *Spin Dynamics. Basis of Nuclear Magnetic Resonance*. 2nd ed. Wiley, 2008. ISBN: 9780470511183.

- [77] A. Schliesser, R. Rivière, O. Arcizet, and T. J. Kippenberg. “Cooling and Measurement of a micromechanical oscillator close to the quantum limit”. In: *2009 Conference on Lasers and Electro-Optics and 2009 Conference on Quantum electronics and Laser Science Conference*. June 2009, pp. 1–2. DOI: [10.1364/IQEC.2009.IFD1](https://doi.org/10.1364/IQEC.2009.IFD1).
- [78] J.J. Sakurai and Jim Napolitano. *Modern Quantum Mechanics*. 2nd ed. Addison-Wesley, 2011. ISBN: 9780805382914.
- [79] Antonio Barone and Gianfranco Paternó. *Physics and Applications of the Josephson Effect*. Wiley, 1982. ISBN: 9780471014690. DOI: [10.1002/352760278X](https://doi.org/10.1002/352760278X).
- [80] V. Bouchiat, D. Vion, P. Joyez, D. Esteve, and M. H. Devoret. “Quantum Coherence with a Single Cooper Pair”. In: *Physica Scripta* 1998.T76 (1998), pp. 165–170. DOI: [10.1238/Physica.Topical.076a00165](https://doi.org/10.1238/Physica.Topical.076a00165).
- [81] Jens Koch, Terri M. Yu, Jay Gambetta, A. A. Houck, D. I. Schuster, J. Majer, Alexandre Blais, M. H. Devoret, S. M. Girvin, and R. J. Schoelkopf. “Charge-insensitive qubit design derived from the Cooper pair box”. In: *Physical Review A* 76 (4 Oct. 12, 2007), p. 042319. DOI: [10.1103/PhysRevA.76.042319](https://doi.org/10.1103/PhysRevA.76.042319).
- [82] Alexandre Blais, Ren-Shou Huang, Andreas Wallraff, S. M. Girvin, and R. J. Schoelkopf. “Cavity quantum electrodynamics for superconducting electrical circuits: An architecture for quantum computation”. In: *Physical Review A* 69 (6 June 29, 2004), p. 062320. DOI: [10.1103/PhysRevA.69.062320](https://doi.org/10.1103/PhysRevA.69.062320).
- [83] David M. Pozar. *Microwave Engineering*. 4th ed. Wiley, 2012. ISBN: 9780470631553.
- [84] Kevin Lalumière, Barry C. Sanders, A. F. van Loo, A. Fedorov, A. Wallraff, and A. Blais. “Input-output theory for waveguide QED with an ensemble of inhomogeneous atoms”. In: *Physical Review A* 88 (4 Oct. 7, 2013), p. 043806. DOI: [10.1103/PhysRevA.88.043806](https://doi.org/10.1103/PhysRevA.88.043806).
- [85] Bernard Yurke. “Use of cavities in squeezed-state generation”. In: *Physical Review A* 29 (1 Jan. 1, 1984), pp. 408–410. DOI: [10.1103/PhysRevA.29.408](https://doi.org/10.1103/PhysRevA.29.408).
- [86] Roger A. Horn and Charles R. Johnson. *Topics in Matrix Analysis*. Cambridge University Press, 1991. ISBN: 9780511840371. DOI: [10.1017/CB09780511840371](https://doi.org/10.1017/CB09780511840371).
- [87] Carlos Navarrete-Benlloch. *Open system dynamics: Simulating master equations in the computer*. Apr. 21, 2015. arXiv: [1504.05266v2](https://arxiv.org/abs/1504.05266v2) [quant-ph].

Colophon

This document was typeset with 11-point EB Garamond, a modern open-source font created by Georg Duffner based on 16th century typefaces by Claude Garamond. Typesetting was performed by the author with pdf~~L~~A~~T~~E~~X~~.

Plots were prepared using Wolfram Mathematica 11.1.

Josephson junctions in figures are from the [jktikz](#) library.

Declaration of Originality

I hereby confirm that I am the sole author of the written work here enclosed and that I have compiled it in my own words. This excludes corrections of form and content by my supervisor.

Title of Work

Time-Resolved Quantum Simulations of Photosynthetic Energy Transport with Superconducting Qubits

Authored By

Norris, Graham J.

With my signature, I confirm that:

- I have committed none of the forms of plagiarism described in the [Citation etiquette](#) information sheet.
- I have documented all methods, data, and processes truthfully.
- I have not manipulated any data.
- I have mentioned all persons who were significant facilitators of this work.

Place, Date

Signature

Zurich, 2018-04-03

Graham Norris